Arab American University-Jenin

Faculty of Graduate Studies

Structural and Optical Properties of Al Doped and Al

Sandwiched ZnSe Thin Films

By

Ansam Mostafa Alsabe

Supervisor

Prof. Dr. Atef Fayez Qasrawi

This thesis was submitted in partial fulfillment of the requirements for

The Master's degree in

Physics

January/2018

Structural and Optical Properties of Al Doped and Al Sandwiched ZnSe Thin Films

By

Ansam Mostafa Alsabe

This thesis was defended successfully on………………...and approved by:

Committee members   Signature

1. Prof. Dr. Atef Fayez Qasrawi   ………………….

2. Dr. Hazem Khanfar   ………………….

3. Dr. Iyad Saadeddin   ………………….

Declaration

The work provided in this thesis, unless otherwise referred, is the researcher's own work and has not been submitted elsewhere for any other degree or qualification.

أقر بأن ما اشتملت عليه هذه الرسالة إنما هو نتاج جهدي الخاص, باستثناء ما تمت الإشارة إليه حيثما ورد, وأن هذه الرسالة ككل من أو جزء منها لم يقدم من قبل أية درجة أو بحث علمي أو بحثي لدى أي مؤسسة تعليمية أو بحثية أخرى.

Student's Name:

Signature:

Date:

To My Parents

Acknowledgments

After thanking Allah, I am grateful to my mother, for the continuous support and encouragement during the university way. O Mum, I owe this work all to you.

To my father Also, I appreciate your help and guiding whenever I need. Many thanks!

I am grateful to my brothers "Mohammad & Oday" since they have never left me when I call for help!

With all respect, I'd like to thank: Prof. Atef Qassrawi for his scientific guidance, constructive directing, and continuous attention to this work.

A special gratitude goes out to all down at physics research lab for guiding and helping until I furnish this work.

My sincere thanks go to the following physics department staff: Prof. Atef Qassrawi, Prof. Zaki Saleh, Prof. Mohammad Sammereh, Dr. Muyyad Abu Saa, and Dr. Adli Saleh for their assistance and patience during my Master period.

And finally, last but by no means least, to my friends and to everyone who helps even with small thing or just asks about my work progress, you all mean to me.

Thanks for all your support!

Structural and Optical Properties of Al Doped and Al Sandwiched ZnSe Thin Films

By

Ansam Mostafa Alsabe

Supervisor

Prof. Dr. Atef Fayez Qasrawi

Abstract

In the current study, Aluminum (Al) doping as well as Al nanosandwiching effects on the structural and optical properties of ZnSe thin films were investigated by means of X-ray diffraction and ultraviolet-visible light-near infrared spectrophotometry techniques, respectively. While the ZnSe doped with 13% Al revealed an amorphous nature of growth, the nanosandwiched films revealed a polycrystalline nature with structural properties that are sensitive to thickness of the sandwiched Al layer. Particularly, the lattice parameter of the cubic unit cell of the ZnSe increased significantly with increasing Al thickness. This increase in the lattice constant was associated with the increase in the grain size and decrease in the strain, dislocation density, and stacking faults. The remarkable enhancements in the crystallinity of the ZnSe that are associated with increasing Al thickness caused an engineering ability of the optical gap. Namely, the energy band gap decreased from 2.67 to 2.05 eV as the Al content increased from 0 to 100 nm. It was also observed that the increase in the Al thickness make band tails deeper. In addition, the analysis of the dielectric spectra has shown that the presence of 100 nm thick Al could increase the real part of the dielectric constant by three times, and increases the drift mobility from 65.6 cm^2/Vs to 280.4 cm^2/Vs .

List of contents

List of tables

List of figures

Chapter One

Introduction and Literature Survey

ZnSe (semiconductor) based electronic devices seems to be promising for the production of the future thin film transistor technology. Thin layers of pure and doped ZnSe have been used in the fabrication of field effect transistors (FET) [1], quantum dots [2, 3] and nanowire FETs [4].

A high performance photodetector was fabricated by the construction of ZnSe/Si *p-n* heterojunction photo-diodes [4]. The responsivity of these diodes is reported to be 1.1×10^5 A/W. It is associated with a photoconductivity gain of 2.9×10^5. On the other hand, the high performance FETs which get uses from ZnSe nanowires with high Si_3N_4 dielectric constant and top-gate geometry, exhibited a substantial improvement in the threshold voltage which was reduced to 1.9 V in addition to the transconductance, hole mobility and I_{on}/I_{off} ratio which were observed to increase up to 864 nS, 10.4 cm^2 V^{-1} s^{-1} and 10^6, respectively [1].

Various metals are used as doping agents to the ZnSe to improve its physical properties so that it can fit correctly with technological needs. For example, a series of co-doped core/shell ZnSe/ZnS quantum dots with tunable photoluminescence maxima spanning a range of 430-570 nm and a broad emission extending up to 700 nm are achieved. This was done through the use of Cu^+ as the primary dopant and trivalent cations (Al^{3+}, Ga^{3+}, and In^{3+}) as co-dopants [5].

The absorption edge red shift was also obtained by the design of a heterojunction. Namely, the design of the InSe/ZnSe heterojunction and InSe/ZnSe/InSe structure shifted the energy band gap of the ZnSe from 2.60 eV to 1.70 and 1.40 eV [6].

Another doping agents like gallium doping to the molecular beam epitaxial layers of ZnSe deposited onto GaAs (100) resulted in reduction of carrier concentration, decrease in the blue photoluminescence emission and increase in the broadband emission [7].

Similarly, the Ag doping to the ZnSe is reported to be promising for the optimization of thin film transistors with tunable electrical and optical properties. Such type of films is judged to be ideal as buffer layer in solar cells [8, 9].

In the scope of the above mentioned features, here in this thesis the physical characteristics of ZnSe can be altered by either Al doping or nanosandiwching into the structure. The status of the material can else be improved via heat treatment under vacuum pressure.

We aim to explore the properties of Al doped and Al sandwiched ZnSe thin films as a novel material suitable for optoelectronic applications. Particularly, the structural, optical, and dielectric properties of Al doped and Al sandwiched ZnSe thin films will be examined. Also, a comparison between Al doped and Al sandwiched ZnSe films properties will be performed. The growth and characterization of Al doped and Al sandwiched ZnSe thin films are for the purpose of finding new types of applications for the ZnSe as a promising candidate for the production of photodetectors, bandstop filters and thin film transistors.

In the second chapter of this thesis, the theoretical background is reported to simplify understanding the results in the light of the existing theories. On the other hand, the necessary details of the experiment are described in chapter three. This chapter will contain information about X-ray diffraction and optical spectrophotometry techniques. The main results that one obtained from the study are shown in chapter four. This chapter will discuss the X-ray analysis of the doped and

sandwiched films, it will report the optical properties of the films, and it will involve the dielectric analysis. Finally, conclusions of the whole work presented in this thesis, will be introduced as a separate part in chapter five.

Chapter Two

Theoretical Background

2.1 Atoms Arrangement and Bravais Lattices

Crystal structure of solids is principally credited to the arrangement of atoms, which controls the material structural, electrical, and optical characteristics. When the atoms that compose the solid are repeated infinitely in three dimensions in an identical manner, the initiated solid is considered as a crystalline material. If the atoms arrangement and orientation are precisely equivalent at all points, a Bravais lattice will be constructed [10].

Space lattice is determined by the positions of atoms that form a repeated unit cell. The lattice unit cell reflects the whole crystal structure. A seven Bravais lattices were established upon the unit cell axial lengths and interaxial angles: cubic, tetragonal, orthorhombic, rohmbohedral (trigonal), hexagonal, monoclinic, and triclinic. The seven crystal systems are classified into 14 subsystems, this classification arises on the basis of the unit cell's internal atoms ordering. Such that, the main crystal lattices may have different unit cells of the type: (1) simple, (2) body-centered, (3) face-centered, or (4) base-centered. For example, the tetragonal system has simple and body-centered unit cells [10].

Primitive vectors of a Bravais lattice, donated by a_i, are defined as the vectors that can span the whole lattice. Thereby, any Bravais lattice position vector can be described in terms of these primitive vectors.

$$R = n_1 a_1 + n_2 a_2 + n_3 a_3 \tag{2.1}$$

Where a_i's are the primitive vectors that may sit in different lattice planes, and n_i's are integer values.

2.2 Face Centered Cubic and Zinc Blende (Zinc Selenide) Structures

Face centered cubic structure (fcc) is one of the most commonly existed crystal structures like the body-centered cubic and hexagonal closed packed (hcp). Lying beneath the face centered cubic is the zinc blende structure, which is characterized as a two (fcc) structures displaced from each other by one quarters of a body diagonal. Such that, the cubic zinc selenide structure is formed when the Zn atoms are placed at $000, 0\frac{1}{2}\frac{1}{2}, \frac{1}{2}0\frac{1}{2}, \frac{1}{2}\frac{1}{2}0$ and Se atoms are at $\frac{1}{4}\frac{1}{4}\frac{1}{4}, \frac{1}{4}\frac{3}{4}\frac{3}{4}, \frac{3}{4}\frac{3}{4}\frac{1}{4}$; this illustrates the presence of four Zn atoms around each Se atom as shown in Fig. 2.1 [11].
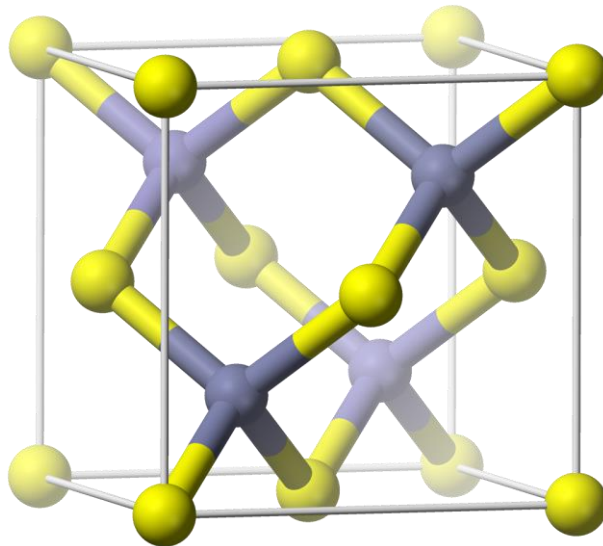
Fig. 2.1. Zinc blende crystal structure.

2.3 X-ray Diffraction

When X-rays bombard a crystalline solid, a set of diffracted X-ray intensities will be obtained. The condition for intensive X-ray producing upon diffraction is a crucial point. Let's consider an incident X-ray, striking a stationary crystalline solid at an angle θ as indicated in Fig. 2.2.
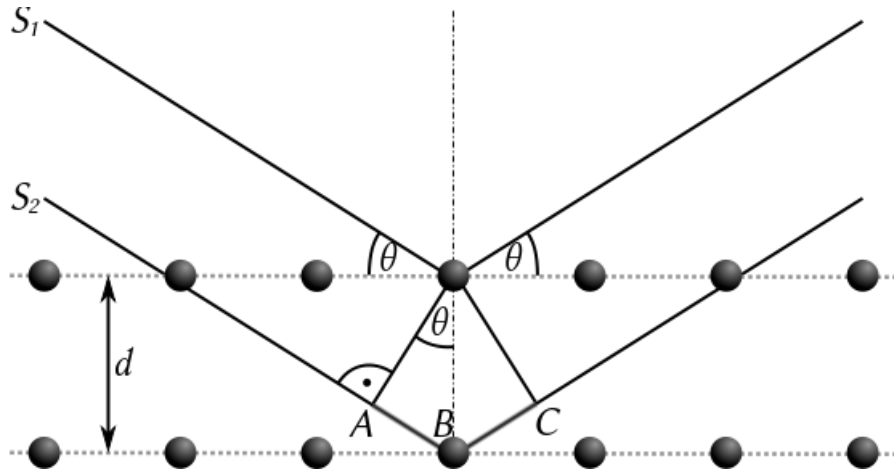
Fig. 2.2. X-ray diffraction by (*hkl*) crystal planes.

The atomic planes behave as an X-ray reflective mirror. Miller indices (*hkl*) are used to represent a specific set of parallel atomic planes. If the diffracted X-rays are out of phase, they diminish each other, and a destructive interference takes place. However, if the X-rays reflected back from the parallel planes, the reflected X-rays will be in phase, the X-ray intensity will build up, and a constructive interference is achieved.

The accomplishment of the constructive interference requires the additional distance traveled by ray S_2 relative to ray S_1 to be an integral multiple of the incident X-ray wavelength (λ) [12,13].

$$AB + BC = n\lambda \tag{2.2}$$

AB and *BC* are both related to the interplanar distance (*d*) for a given parallel planes (*hkl*) and to the X-ray angle of incidence (θ), such that they equal *d sinθ*. Subsequently, the constructive interference condition will have the form,

$$n\lambda = 2d \sin \theta \tag{2.3}$$

This equation is called Bragg's equation. The first order diffraction ($n = 1$) is generally employed,

$$\lambda = 2d \sin \theta \tag{2.4}$$

Interplanar spacing (d) of the cubic structure expressed by the following formula can be used to determine the lattice constant (a).

$$\frac{1}{d^2} = \frac{h^2 + k^2 + l^2}{a^2} \tag{2.5}$$

2.4 Major Concepts Correlated to Crystalline Solids

2.4.1 Full Width at Half Maximum (β)

The full width at the half maximum (FWHM) is defied as the angular broadening at the half maximum of the X-ray intensity [14].

2.4.2 Grain Size (D)

D is defined as a single crystal size of the crystalline solid. It is known that the polycrystalline material is a collection of single crystal grains, and atoms in each grain have the same orientation. However, atoms in single crystal materials have a one definite orientation.

Sherrer's formula can be used to connect the grain size D to the angular broadening β of the X-ray intensity [15]. It can be derived by employing the first order Bragg's law introduced in equation (2.4).

$$\lambda = 2d \sin \theta$$

Multiply both sides of the previous equation by an integer m, where m is the number of the parallel atomic planes.

$$m\lambda = 2md \sin \theta \tag{2.6}$$

And $m\,d$ = crystallite size (D). Hence, the first order Bragg's equation will be presented as,

$$m\lambda = 2D\sin\theta \tag{2.7}$$

If we differentiate both sides of equation (2.7) with respect to the grain size D and to the angle of incidence θ, one readily gets

$$0 = 2\Delta D\sin\theta + 2D\cos\theta\Delta\theta \tag{2.8}$$

From equation (2.8), the magnitude of the crystallite size D is given by,

$$D = \frac{\Delta D\sin\theta}{\cos\theta\Delta\theta} \tag{2.9}$$

The minus sign resulted from equation (2.8) rearrangement is ignored, since the crystallite size D represents a measured physical quantity. Interplaner distance d can be substituted instead of ΔD to get,

$$D = \frac{d\sin\theta}{\cos\theta\Delta\theta} \tag{2.10}$$

Braggs law can be used again, such that $d\sin\theta = \frac{\lambda}{2}$. Then, the grain size equation illustrated in (2.10) becomes,

$$D = \frac{\lambda}{2\cos\theta\Delta\theta} \tag{2.11}$$

However, $2\Delta\theta = \beta$, where β is the previously investigated FWHM. Then D equation is simplified to,

$$D = \frac{\lambda}{\beta\cos\theta} \tag{2.12}$$

Finally, more complicated derivations predict the precise Sherrer's formula, where the wavelength (λ) is multiplied by a factor of 0.9 rather 1 [16, 17].

$$D = \frac{0.9\lambda}{\beta \cos\theta} \qquad (2.13)$$

2.4.3 Strain (ε)

Strain is the expansion or contraction in the atomic distances relative to the original. The following equation indicated the susceptibility of the intensity broadening β to the solid strain alterations [18],

$$\varepsilon = \frac{\beta}{4\tan\theta} \qquad (2.14)$$

Strain refers to crystal imperfections like lattice stacking faults and dislocations. A strain of 2×10^{-3} donates that a specified length of a solid may have 2000 stretched atomic distances. Or, a crystalline solid made up by 1 million cells, a 2000 unit cells may be exposed to expansion or contraction.

2.4.4 Stacking Fault (*SF*)

Stacking fault is a kind of crystalline imperfections, which describes the atomic planes disordering. So, it is categorized as a planer imperfection. Stacking fault can be evaluated by using the subsequent formula [19],

$$SF = \frac{2\pi^2\beta}{45\sqrt{3}\tan\theta} \qquad (2.15)$$

A popular stacking fault is the fault introduced in the face-centered cubic and hexagonal close-packed planes. It is known that the fcc has ABC sequence, while ABA sequence is referred to the hcp structure, the deviation from these ordered sequences is assigned to the stacking faults defects [20]. For example, the fcc sequence that was affected by stacking imperfections may have the form ABCABABCAAB….

2.4.5 Dislocation Density (δ)

Dislocation density is the number of the linear crystalline defects per unit volume. It may be caused by the inner atomic planes removal. The existence of the dislocations greatly affects the solid material properties. The following formula used for dislocation density calculation [21],

$$\delta = \frac{15\varepsilon}{a\,D} \tag{2.16}$$

2.5 Energy Band Gap (E_g)

Lattice is made up by the endless repetition of identical atoms, in which each atom has many bound and unbound electrons. When the atoms are close enough, their electrons which occupy the outer most energy states will interact with each other, leading to energy states overlapping and allowed band formation. The inner energy states may form a band of allowed energies as well. Electrons reside the allowed bands are detached by a forbidden region called an energy band gap, in which energy levels cannot exist. The concepts of overlapping, energy bands, and the forbidden gap formation are referred to an energy band theory of solids [22]. Valence band (the lower band) is formed when the states filled with valence electrons split into a band. However, the conduction band (the upper band) is created when the outermost electrons (free electrons) energy levels overlap. According to Fermi-Dirac distribution in semiconductors, at $T=0\ K$ valence band is filled with electrons and the conduction band is empty. When the temperature is raised above zero, valence electrons gain enough energy to break the bonds and run across the energy gap up to the conduction band, leaving behind an empty space called hole. The electron-hole energy-momentum (E-k) relation is dignified in characterizing carriers-photons/phonons interactions, such that the energy must be conserved and hence the momentum. E-k relationship will have the form,

$$E(k) = \frac{\hbar^2 k^2}{2m^*} \qquad (2.17)$$

Where $\hbar$ is Planck's constant and k is the wave vector. A theorem that is strongly related to the band structure is Bloch theorem [23]. Since the atoms in a lattice are ordered in a periodic manner, the crystalline potential must hold the periodicity of the lattice

$$U(r+R) = U(r) \qquad (2.18)$$

Where r is the position vector and R is the lattice vector. By substituting the potential $U(r)$ in Schrödinger equation of one electron problem,

$$(-\frac{\hbar^2}{2m}\nabla^2 + U(r))\psi = E\psi \qquad (2.19)$$

Bloch electrons were defined to be electrons that posses a periodic potential and satisfy Schrödinger equation. The solution of the Schrödinger equation (2.20) is $\psi(r)$, it have the form of a plane wave times a function that reflects the lattice periodicity presented as follows,

$$\psi(r) = e^{ik.r} u_{nk}(r) \qquad (2.20)$$

However, $\psi(r+R)$ can be substituted in the previous equation and it is easily found to have the formula

$$\psi(r+R) = e^{ik.(r+R)} u_{nk}(r+R) \qquad (2.21)$$

The periodicity in the potential presented by equation (2.19) implies,

$$\psi(r+R) = e^{ik.r} e^{ik.R} u_{nk}(r) \qquad (2.22)$$

$\psi(r + R)$ equals $\psi(r)$ if $k.R$ is a multiple of 2π; this can be attached to the relation that connects the direct space to k space [23].

$$G.R = 2\pi \times integer \tag{2.23}$$

Where G is the lattice reciprocal vector, which stands for k in expressing the *E-k* relationship. Thus, the energy $E(k)$ must also hold the lattice periodicity $E(k) = E(k + G)$.

2.6 Optical Processes Categorization

An ordinary classification of optical processes encloses reflection, propagation and transmission. Consider a medium exposed to a light beam of a specific propagation thickness. The incident beam may be reflected from the front surface, or propagates through until it reaches the back surface. The light at the back surface may be reflected or transmitted outside the medium. It is evident that the transmitted light depends on the front and back surface reflectivities as well as to the propagated medium [24]. Linear optical propagation implicates four processes: refraction, absorption, luminescence, and scattering.

Refraction can be referred as light bending when it travels from one interface to another. Refraction includes attenuation in the light velocity compared to the free space velocity. Light bending at two mediums interface is described by Snell's law [25].

$$n_1 \sin \theta_1 = n_2 \sin \theta_2 \tag{2.24}$$

Absorption is essentially related to the propagated light frequency. If the light frequency is in resonance with the frequency of solid material oscillations, the light will be absorbed. As the absorption increases the intensity of the transmitted beam will be reduced.

Luminescence is associated with spontaneous emission. Such that, light brings electrons to the excited states and a constitutive emission occurs. The emitted light is incoherent, and possesses a color different to that of the incident light. Absorbance can be considered as the competitor optical process to luminescence.

Scattering is another process that may take place during light propagation. It involves light redirection and it may change the light frequency. The total number of photons remains invariant, while the straightforward propagating photons are attenuated since photons scattered in other directions. So, the intensity of the incoming beam is reduced [26].

2.7 Absorption of Light in Matter

Absorption spectrum analysis is one of the most prevalent techniques for semiconductors band structure and energy gap (E_g) realization. Absorption is concerned with photon-electron interaction, in which an incident photon induces electron transfer from the valence to conduction band. Absorption coefficient $\alpha(hv)$ quantifies material's light absorption, which is defined as the rate of incident light intensity attenuation over the propagated distance [27].

Electron momentum is maintained conserve even when the photon is absorbed, since the photon momentum ($\frac{h}{\lambda}$) is less than the crystal momentum ($\frac{h}{a}$).

The absorption coefficient $\alpha(hv)$ is linearly proportional to the electron transition probability P_{if}, initial states electron density n_i, and empty final states density n_f. This proportionality is introduced through the following equation [27],

$$\alpha(hv) = A \sum P_{if} n_i n_f \tag{2.25}$$

Fig. 2.3 reveals a multilayer film of a specified thickness, the incident light beam propagates along the z-axis, and the light intensity at point z is $I(z)$. The propagated light will be attenuated by an amount dI

$$dI = -\alpha dz \times I(z)$$ (2.26)

If we apply separation of variables and then integrate, Beer's law will be obtained. This law describes an exponential relation between light intensity and the propagated distance.

$$I(z) = I_o e^{-\alpha z}$$ (2.27)

Where I_o is defined as the light intensity at $z=0$. The transmittance of the multilayer film is expressed as follows,

$$T = \frac{(1 - R_1)e^{-\alpha d}(1 - R_2)}{1 - R_1 R_2 e^{-2\alpha d}}$$ (2.28)

Where d is the medium thickness and R is the reflectivity of the film surfaces. However, the preceding equation denominator goes to one if the surfaces are parallel and their reflectivity is large [24].

$$T = (1 - R_1)e^{-\alpha d}(1 - R_2)$$ (2.29)

Absorbance (A) of a grown film can be evaluated if one knows the film's transmittance (T) and reflectance (R),

$$A = -\ln\left(\frac{T}{(1 - R_{glass})(1 - R_{sample})}\right)$$ (2.30)

If the films thickness (d) is monitored, Absorption coefficient $\alpha(hv)$ can be connected to the film's absorbance (A) through the relation,

$$A = \alpha d \qquad (2.31)$$

Absorption coefficient $\alpha(hv)$ can be expressed in terms of the film's transmittance (T) and reflectance (R) such that,

$$\alpha = \frac{-\ln\left(\dfrac{T}{(1-R_{glass})(1-R_{sample})}\right)}{d} \qquad (2.32)$$

Alternatively, $(T + R + A = 100)$ can be used to get the propagated mediums absorption [24]. This method overrides light scattering, which is defined previously as the redirection of the propagated light.
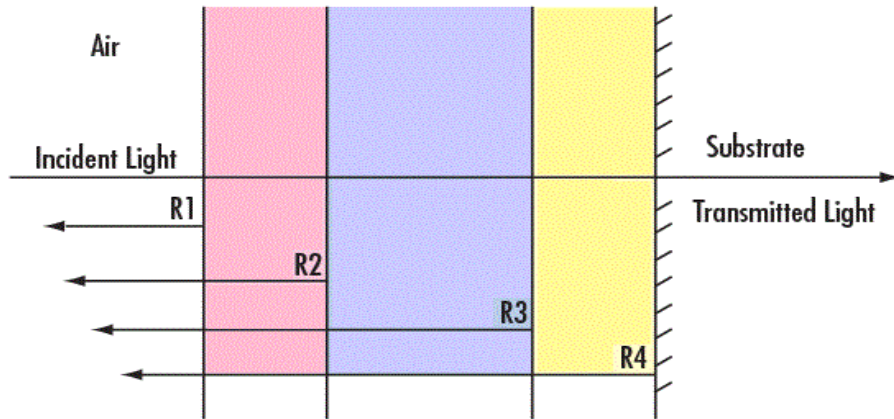
Fig. 2.3. A light beam incident on an optical medium is exposed to multiple reflections.

2.7.1 Allowed Direct Transitions

The allowed direct absorption transition illustrated in Fig. 2.4 (a) takes place when the valence and conduction bands valleys are direct and posses the same k-vector regardless of the incident photon

energy. The valence band initial states are tied up with the conduction band final states through the equation [27],

$$E_f = h\nu - E_i \tag{2.33}$$

However, the initial and final energy states of the parabolic bands are given by the following formulas [27],

$$E_f - E_g = \frac{\hbar^2 k^2}{2m_e^*} \tag{2.34}$$

And,

$$E_i = \frac{\hbar^2 k^2}{2m_h^*} \tag{2.35}$$

When incident photons interact with solids, it stimulates an electron resides in the valence band up to conduction band where,

$$E_f = h\nu - |E_i|$$

If we subtract E_g from the both sides of the previous equation, we will obtain

$$E_f - E_g = h\nu - E_g - |E_i| \tag{2.36}$$

Equations (2.34) and (2.35) are then substituted in equation (2.36) to give,

$$\frac{\hbar^2 k^2}{2m_e^*} = h\nu - E_g - \frac{\hbar^2 k^2}{2m_h^*} \tag{2.37}$$

Equation (2.37) rearrangement yields,

$$h\nu - E_g = \frac{\hbar^2 k^2}{2m_e^*} + \frac{\hbar^2 k^2}{2m_h^*} = \frac{\hbar^2 k^2}{2}\left(\frac{1}{m_e^*} + \frac{1}{m_h^*}\right) \tag{2.38}$$

The states density in an energy range that extends from $h\nu$ to $h\nu+d(h\nu)$ was reported frequently in literature to have the form [27],

$$N(h\nu)d(h\nu) = \frac{8\pi k^2 dk}{(2\pi)^3} \tag{2.39}$$

By rearranging equation (2.38),

$$k^2 = \frac{2(h\nu - E_g)}{\hbar^2} m_r \tag{2.40}$$

m_r is the reduced mass, where $\dfrac{1}{m_r} = \dfrac{1}{m_e^*} + \dfrac{1}{m_h^*}$ \qquad (2.41)

Equation (2.40) are then differentiated implicitly with respect to (k) and ($h\nu$) respectively to yield,

$$2kdk = \frac{2m_r}{\hbar^2} d(h\nu) \tag{2.42}$$

By substituting equations (2.40) and (2.42) in (2.39), the equation that describes states density becomes

$$N(h\nu)d(h\nu) = \frac{16\pi(h\nu - E_g)m_r}{\hbar^2 (2\pi)^3} dk \tag{2.43}$$

By employing equations (2.40) and (2.42) in the previous equation (2.43), the states density equation will be rewritten as,

$$N(h\nu)d(h\nu) = \frac{16\pi(h\nu - E_g)}{\hbar^2(2\pi)^3} \frac{m_r^2}{\hbar^2\sqrt{\frac{2(h\nu - E_g)m_r}{\hbar^2}}} d(h\nu) \tag{2.44}$$

This equation is then simplified to take the form,

$$N(h\nu)d(h\nu) = \frac{(2m_r)^{\frac{3}{2}}}{2\pi^2\hbar^3}(h\nu - E_g)^{\frac{1}{2}}d(h\nu) \tag{2.45}$$

Since the absorption coefficient is linearly proportional to the initial and final states density N_i and N_f respectively,

$$\alpha(h\nu) = A^*(h\nu - E_g)^{\frac{1}{2}} \tag{2.46}$$

Where $A^* = \dfrac{q^2(\dfrac{2m_h^* m_e^*}{m_h^* + m_e^*})^{\frac{1}{2}}}{nch^2 m_e^*}$ \tag{2.47}

2.7.2 Forbidden Direct Transitions

Here, quantum selection rules prohibit $k = 0$ direct absorption transitions but let them otherwise. Then, the forbidden vertical transition probability will be directly proportional to k^2. Since $k^2 = \dfrac{2(h\nu - E_g)m_r}{\hbar^2}$, the forbidden direct transition will contain an extra $(h\nu - E_g)$ [27]. Particularly, the absorption coefficient of the allowed direct transition is $\alpha(h\nu) = A^*(h\nu - Eg)^{1/2}$, however the forbidden direct transition absorption coefficient will be $\alpha(h\nu) = A'(h\nu - E_g)^{3/2}$.

2.7.3 Indirect Valleys and Indirect Transitions

When a change in the electron momentum is involved, a two-step transition is demanded as shown in Fig. 2.4 (b). Because photon momentum is low compared to the crystal momentum, the indirect transition is a phonon assisted process [27]. Therefore, in order to accomplish an indirect electron transition from valence to the conduction band, a phonon is either absorbed or emitted.

$$h\nu_c = E_f - E_i + E_p \tag{2.48}$$

$$h\nu_a = E_f - E_i - E_p \tag{2.49}$$
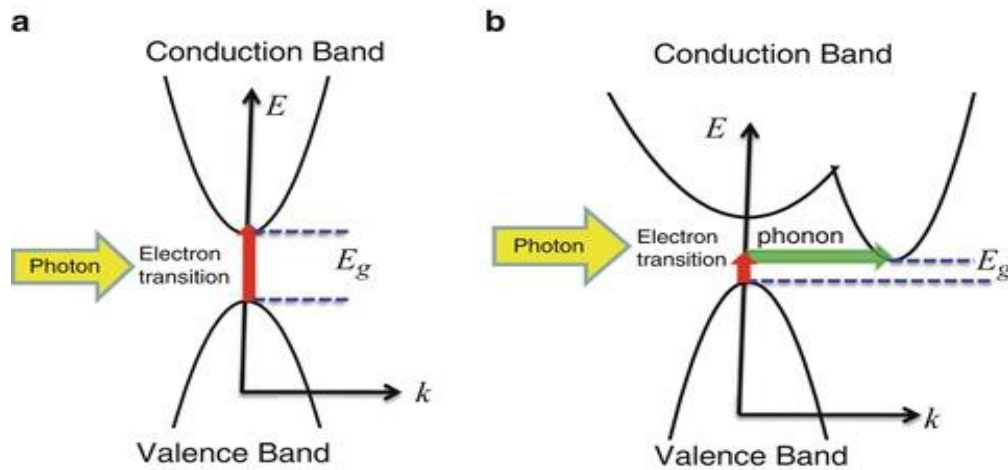
Fig. 2.4. Incident photons cause solids inerband (a) direct and (b) indirect transitions.

2.7.4 Direct Valleys and Indirect Transitions

Direct valleys can be expressed by the maximum of the valence band and the minimum of the conduction band symmetrical consistency. Indirect transition between direct valleys is supported by phonons absorption or emission as stated previously. The absorption coefficient here is directly proportional to $(h\nu - E_g)^2$ [27].

2.8 Doped Semiconductors and the Effect of Free Carriers

By semiconductor n-type or p-type doping, a considerable free electrons and holes densities will be reproduced, which sets up plasmon effects and enhances the optical absorption.

The free carrier's density is usually between $10^{18} - 10^{19} cm^{-3}$, this indicates a small plasmon frequency in the doped semiconductor, which leads to light absorption below the energy gap upon band tails formation [24].

2.9 Transitions Involves Band Tails

Band tails stand out as a result of impurities doping, such that the impurities levels extend into the forbidden gap deform the valence and conduction band. The ionized impurities of the five valence type exert an electrostatic repulsive force on the holes present in the valence band. While, the conduction band electrons are attracted.

The constancy of the energy gap throughout the bulk crystal is known. However, impurities presence shifts the valence band up or lowers the conduction band. Thus, a change in the energy gap is recorded upon doping.

The randomly distributed impurities that perturb the crystal are: the interstitial atoms, substitutional atoms, and vacancies. The interstitial atoms reproduce a compressional strain. On the other hand, vacancies cause lattice dilation. Compression will provoke an increase in the energy gap, while dilation lowers the gap.

Transitions involve impurities induced band tails shows exponentially increased absorption spectra at photon energies less than the energy gap. It is important to investigate and derive the relation that

conducts the band tails influence on the absorption coefficient. The initial density of the doping induced band tails is proportional to the square root of the valence band $E_v^{1/2}$. The band tails final state density and the absorption coefficient are expressed as follows [27],

$$N_f = N_0 e^{E/E_0} \tag{2.50}$$

$$\alpha(h\nu) = A\int_{E_v}^{h\nu - E_v} |E_v|^{1/2} \exp(E/E_0)dE \tag{2.51}$$

Substitute $E - h\nu$ instead of E_v in order to solve the integration by the following change of variables,

$$x = \frac{h\nu - E}{E_0} \tag{2.52}$$

The integration indicated in equation (2.51) will have the form,

$$\alpha(h\nu) = -Ae^{h\nu/E_o}(E_o)^{3/2} \int_{\frac{h\nu+E_v}{E_o}}^{\frac{E_v}{E_o}} x^{1/2}e^{-x}dx \tag{2.53}$$

$$\alpha(h\nu) = A(E_o)^{3/2}e^{h\nu/E_o}(\frac{1}{2}\pi^{1/2} - \int_0^{E_v/E_o} x^{1/2}e^{-x}dx) \tag{2.54}$$

Then the width of the band tails established near the top of the valence band or the bottom of the conduction band is given by,

$$E_o = (\frac{d\ln\alpha}{dh\nu})^{-1} \tag{2.55}$$

Alternatively, the following equation can be used to determine the width of the formed band tails.

$$\alpha = \alpha_o e^{\frac{E}{E_e}} \tag{2.56}$$

Hence, lattice deformation is a doping consequence. The transition will connect one of the bands (valence/conduction) with the impurities induced band tails. For example, in *n*-type semiconductor, the donor atoms stimulate the formation of the near valence band tails. Whereas, in *p*-type semiconductors, the acceptor atoms cause conduction band tails formation [27].

2.10 Band Gap Measuring

The band gap calculation is substantial in understanding solids characteristics. The energy gap can be specified by using the spectrophotometric absorption spectrum. Electrical conductivity measurements and the related thermal activation energies can be used to estimate the energy gap too.

The spectrophotometric absorption coefficient is correlated to the incident photon energy through Tauc equation,

$$(\alpha E)^{1/p} = B(E - E_g) \tag{2.57}$$

Where E is the incident photon energy, p is an index that specifies the type of the optical absorption process and it can take many values, B is a constant that is principally depends on the probability of electron transition, and E_g is the desired energy gap.

The parameter p can have the values 2, 1/2, 3, and 3/2 for indirect allowed, direct allowed, indirect forbidden, and direct forbidden electronic transition, respectively.

The E_g determination requires $(\alpha E)^{1/p}$ plotting versus the incident photon energy E. Such that, $(\alpha E)^{1/2}$, $(\alpha E)^2$, $(\alpha E)^{1/3}$, and $(\alpha E)^{2/3}$ were graphed in order to select the p value of graph with a widest range of

linear data in the high absorption region. The linear portion of $(\alpha E)^{1/p}$ can be extrapolated, and the intercept of the photon energy axis returns the energy gap [28].

2.11 Dielectric Spectra

Refractive index is one of the dielectric solids most distinctive optical features, which depends on the wavelength of the incident optical beam. The refractive index-optical wavelength relation is introduced by an equation called the dispersion equation. The dispersive refractive index is given by the following equation [24],

$$N_{complex} = n(\lambda) + ik(\lambda)$$
$$= (\varepsilon_r + i\varepsilon_{im})^{1/2} \tag{2.58}$$

$k(\lambda)$ is the extinction coefficient, while ε_r and ε_{im} is the real and imaginary dielectric constants, respectively. It is obvious that the dispersion equation (2.58) comprises some imaginary terms. This interprets that the propagating electromagnetic waves through the dielectric solid undergoes optical attenuation and dispersion.

The effective dielectric constant ε_{eff} is expressed in terms of the dielectric refractive index $n(\lambda)$ through the relation,

$$\varepsilon_{eff} = n^2(\lambda) \tag{2.59}$$

The effective dielectric constant ε_{eff} can be expressed in terms of the real ε_r and imaginary ε_{im} dielectric constants.

$$\varepsilon_{eff} = \varepsilon_r + i\varepsilon_{im} \tag{2.60}$$

Where ε_r and ε_{im} can be connected to the refractive index $n(\lambda)$ by squaring the both sides of equation (2.58),

$$n^2(\lambda) - k^2(\lambda) + i2n(\lambda)k(\lambda) = \varepsilon_r + i\varepsilon_{im} \tag{2.61}$$

By comparing the real and imaginary parts on both sides one immediately get ε_r and ε_{im} in terms of $n(\lambda)$ and $k(\lambda)$.

$$n^2(\lambda) - k^2(\lambda) = \varepsilon_r \tag{2.62}$$

$$2n(\lambda)k(\lambda) = \varepsilon_{im} \tag{2.63}$$

Replacing the refractive index $n(\lambda)$ by $(\varepsilon_{eff})^{1/2}$, the real and imaginary dielectric constants can be expressed as follows,

$$\varepsilon_r = \varepsilon_{eff} - (\frac{\alpha\lambda}{4\pi})^2 \tag{2.64}$$

$$\varepsilon_{im} = \sqrt{\varepsilon_{eff}}(\frac{\alpha\lambda}{2\pi}) \tag{2.65}$$

An incident electromagnetic wave propagated along the z-axis inside a dielectric material compromises an electric field part [24].

$$E_x = E_0 e^{i(kz-\omega t)} \tag{2.66}$$

Where, $k = \frac{\omega}{c} N_{complex}$ \qquad (2.67)

The electric field consists of incident and reflected waves moves along +z-axis and –z-axis, respectively.

$$E_x = E_1 e^{i(\frac{\omega z}{c} - \omega t)} + E_2 e^{i(\frac{-\omega z}{c} - \omega t)}$$

(2.68)

The E_x continuity at the dielectric surface initiates a relation between E_o, E_1 and E_2.

$$E_o = E_1 + E_2$$

(2.69)

The continuity in the tangential magnetic field component H_y at the surface, gives rise to the second relation between E_o, E_1, and E_2. Using Maxwell's equations,

$$\nabla \times E = -\frac{\mu}{c}\frac{dH}{dt} = \frac{i\mu\omega}{c}H$$

(2.70)

By applying the curl relative to z-axis to the x-component of the incident electric field, we attain

$$\frac{dE_x}{dz} = \frac{i\mu\omega}{c}H_y$$

(2.71)

Equation (2.71) above yields,

$$E_o k = E_1\frac{\omega}{c} - E_2\frac{\omega}{c} = E_o\frac{\omega}{c}N_{complex}$$

(2.72)

Simplification of equation (2.72) yields,

$$E_1 - E_2 = E_o N_{complex}$$

(2.73)

Then, the normal reflectance and the reflection coefficient can be expressed as,

$$R = \left|\frac{E_2}{E_1}\right|^2$$

(2.74)

$$r = \frac{E_2}{E_1}$$

(2.75)

E_2 and E_1 can be rewritten by using equations (2.69) & (2.73),

$$E_2 = \frac{1}{2}E_o(1 - N_{complex}) \hspace{6cm} (2.76)$$

$$E_1 = \frac{1}{2}E_o(1 + N_{complex}) \hspace{6cm} (2.77)$$

Equations (2.76) & (2.77) are used to rewrite the normal reflectance indicated by equation (2.74) in terms of $N_{complex}$.

$$R = \left| \frac{1 - N_{complex}}{1 + N_{complex}} \right|^2 = \frac{(1-n)^2 + k^2}{(1+n)^2 + k^2} \hspace{4cm} (2.78)$$

The Reflectance R and the effective dielectric constant ε_{eff} are related through the following equation. This relation enables the extraction of the effective dielectric constant ε_{eff} from the spectral reflectance R and absorption coefficient data α.

$$R = \frac{(\sqrt{\varepsilon_{eff}} - 1)^2 + k^2}{(\sqrt{\varepsilon_{eff}} + 1)^2 + k^2} \hspace{5cm} (2.79)$$

$$\text{Where } k = \frac{\alpha\lambda}{4\pi} \hspace{6cm} (2.80)$$

At a high optical wavelength λ, the extinction coefficient k will grow to a large value, then the terms contain ε_{eff} in equation (2.79) will be ignored, and the reflectance R is roughly 100%. In this situation, low energy electromagnetic waves impinge the dielectric solid will be reflected, and the rest will enter and then attenuated.

We can rewrite equation (2.79) as follows in order to extract ε_{eff} as a function of the light reflectance R.

$$R(\sqrt{\varepsilon_{eff}} + 1)^2 + Rk^2 = (\sqrt{\varepsilon_{eff}} - 1)^2 + k^2 \qquad (2.81)$$

By squaring $(\sqrt{\varepsilon_{eff}} + 1)$ and $(\sqrt{\varepsilon_{eff}} - 1)$ on both sides, rearranging, and simplifying the equation we obtain,

$$\varepsilon_{eff} + \frac{2(R+1)}{(R-1)}\sqrt{\varepsilon_{eff}} + k^2 = 0 \qquad (2.82)$$

This equation is then solved in order to find a formula for ε_{eff} using the generalized law.

$$\sqrt{\varepsilon_{eff}} = \frac{-\dfrac{2(R+1)}{(R-1)} \pm \sqrt{(\dfrac{2(R+1)}{(R-1)})^2 - 4k^2}}{2} \qquad (2.83)$$

As observed in equation (2.83) two roots are involved. These roots are squared and separated into two distinct solutions.

$$\varepsilon_{eff1} = \left(\frac{-\dfrac{2(R+1)}{(R-1)} + \sqrt{(\dfrac{2(R+1)}{(R-1)})^2 - 4k^2}}{2}\right)^2 \qquad (2.84)$$

$$\varepsilon_{eff2} = \left(\frac{-\dfrac{2(R+1)}{(R-1)} - \sqrt{(\dfrac{2(R+1)}{(R-1)})^2 - 4k^2}}{2}\right)^2 \qquad (2.85)$$

2.12 Drude-Lorentz Model

The data of the imaginary dielectric constant ε_{im} can be analyzed using the effective-oscillator model to provide a comprehensive polarization overview. Dielectric solid atoms or molecules can be treated as an agglomerate of oscillators. When the electric field of the electromagnetic waves interacts with the dielectric material, it inflames the dipole oscillations. The electrons bounded to the positively charged

nucleuses vibrate around an equilibrium position with a specific resonant frequency according to Drude-Lorentz model.

Semiconductor doping facilitates more free electrons creation. The Paul Drude model is used to demonstrate metallic free electron vibrations. However, the Drude-Lorentz model employs the dipole oscillator model to free electron model [24].

When the incident light waves interact with the solid atoms, a dipoles oscillation happens with a resonant frequency ω_o. A damped harmonic oscillator is used to inspect dipoles displacement. The damping in the generated dipoles oscillation is referred to the electron collisions with immobile ions. Phonons interactions can be referred as the main reason for frictional damping.

The electric field of the electromagnetic waves exerts a force on the optically created atomic dipoles. Since $m_N >> m_o$, the nucleus is considered to be stationary. The equation of motion that describes the electron motion is expressed as follows [24],

$$m_o \frac{d^2 x}{dt^2} + m_o \gamma \frac{dx}{dt} + m_o \omega_o^2 x = -eE \qquad (2.86)$$

Where m_o is the electron mass, x is the electron displacement, γ is the damping coefficient, e is the electronic charge, and E is the electric field.

The former equation left side involves an accelerating, damping, and force restored terms. On the other hand, the right side includes the driving force term.

We transact with an incident light electric field with a frequency ω. The electric field is time dependent as introduced by the following equation [24],

$$E(t) = E_o \cos(\omega t + \phi) = E_o \operatorname{Re}(\exp(-i\omega t - \phi)) \tag{2.87}$$

Where E_o and ϕ are the electric field amplitude and the light phase, respectively. The AC electric field brings on oscillations that have the form,

$$X(t) = X_o \operatorname{Re}(\exp(-i\omega t - \phi')) \tag{2.88}$$

Where X_o is the amplitude of the electron displacement, and ϕ' is the oscillation phase. We can substitute ϕ and ϕ' into electric field and displacement amplitudes. Moreover, E_o and X_o must be complex numbers. By inserting the equations of the electric field (2.87) and the expected displacement performance (2.88) in the equation of motion (2.86),

$$-m_o \omega^2 X_o e^{-i\omega t} - im_o \gamma \omega X_o e^{-i\omega t} + m_o \omega_o^2 X_o e^{-i\omega t} = -eE_o e^{-i\omega t} \tag{2.89}$$

The previous equation entails,

$$X_o = -\frac{\frac{eE_o}{m_o}}{\omega_o^2 - \omega^2 - i\gamma\omega} \tag{2.90}$$

A time dependent dipole moment $p(t)$ results from the frequency variant displacement amplitude denoted in equation (2.90), participates in the resonant polarization induction. Polarization is defined as the dipole moment per unit volume.

$$\begin{aligned} P_{resonant} &= Np \\ &= -Nex \tag{2.91} \\ &= \frac{Ne^2}{m_o} \frac{1}{\omega_o^2 - \omega^2 - i\gamma\omega} E \end{aligned}$$

N is the number of atoms per unit volume. Equation (2.91) illustrates that polarization maximizes when the electric field frequency approaches ω_o; this implies that the oscillation is ignored except if the incident light frequency is consistent with the material natural frequency ω_o. Electric displacement D of a solid is polarization and electric field dependent [24].

$$D = \varepsilon_o E + P \tag{2.92}$$

As we said before, oscillations are ignored unless $\omega = \omega_o$, thus polarization can be categorized into a resonant and non-resonant parts.

$$D = \varepsilon_o E + P_{background} + P_{resonant}$$
$$= \varepsilon_o E + \varepsilon_o \chi E + P_{resonant} \tag{2.93}$$

Where χ is the electric susceptibility. In our seeking for the imaginary dielectric constant, the material is postulated to be isotropic. Isotropic expression proposes that the material possesses the same characteristics in all directions, and having no preferred axes. With this assumption, the electric displacement can be redefined as

$$D = \varepsilon_o \varepsilon_r E \tag{2.94}$$

Where ε_r is the relative dielectric constant. By employing the previous equation (2.94), the relative dielectric constant will be

$$\varepsilon_r(\omega) = 1 + \chi + \frac{Ne^2}{\varepsilon_o m_o}(\frac{1}{\omega_o^2 - \omega^2 - i\gamma\omega}) \tag{2.95}$$

This formula can be rearranged, in order to separate the real and imaginary dielectric constants. ε_1 and ε_2 are then obtained to be,

$$\varepsilon_1(\omega) = 1 + \chi + \frac{Ne^2}{\varepsilon_o m_o}\left(\frac{\omega_o - \omega^2}{(\omega_o^2 - \omega^2)^2 + (\gamma\omega)^2}\right)$$

(2.96)

$$\varepsilon_2(\omega) = \frac{Ne^2}{\varepsilon_o m_o}\left(\frac{\gamma\omega}{(\omega_o^2 - \omega^2)^2 + (\gamma\omega)^2}\right)$$

(2.97)

By utilizing an incoming light of frequency ω, which is compatible with the material natural resonant frequency ω_o, the assumption $\omega \approx \omega_o \gg \gamma$ can be stated. $(\omega_o^2 - \omega^2)$ term can be roughly approximated to $2\omega_o\Delta\omega$.

Static dielectric constant ε_{st} can be clarified as the relative dielectric constant ε_r at $\omega = 0$, which designate the low frequency material permittivity in the presence of static electric fields.

$$\varepsilon_1(0) = \varepsilon_{st} = 1 + \chi + \frac{Ne^2}{\varepsilon_o m_o \omega_o^2}$$

(2.98)

The high frequency permittivity can be indicated by the relative dielectric constant at $\omega = \infty$,

$$\varepsilon_r(\infty) = \varepsilon_\infty = 1 + \chi$$

(2.99)

By subtracting the last two equations (2.98) and (2.99),

$$\varepsilon_{st} - \varepsilon_\infty = \frac{Ne^2}{\varepsilon_o m_o \omega_o^2}$$

(2.100)

Chapter Three

Experimental Details

3.1 Thin Film Preparation

Glass substrates were cut to the desired size by using a cutter pen, then cleaned with soap and washed with distilled water. Alcohol is also used to rinse the glasses. The alcohol treated substrates were immersed in a beaker filled with H_2O_2. The beaker is boiled for 15 minutes. At this time, the ultrasonic device is turned on and waited to reach 70 °C. The H_2O_2 is poured out of the beaker and replaced by alcohol; the beaker is then inserted in the ultrasonic device for 40 minutes. The cleaned glass substrates are then used as a basis for films deposition.

The 300 nm thick Al doped ZnSe thin films were prepared by using 0.2 gm ZnSe powder and 0.04 gm Al. The ZnSe and Al were filled in a double source, which settled in a physical vapor deposition system shown in Fig. 3.1. The materials were evaporated together to form Al doped ZnSe thin films, this evaporation was achieved under a vacuum pressure of 10^{-5} mbar. Some of ZnSe and Al were remained in the boats after finishing the preparation of Al doped ZnSe films. The pure ZnSe thin film was prepared by the evaporation of the ZnSe powder on a cleaned glass substrate using the vapor deposition system. The ZnSe and Al doped ZnSe thin films are shown in Fig. 3.2.

Al nanosandwiching was achieved by utilizing physical vapor deposition technique in 500 nm thick ZnSe layer deposition over ultrasonically cleaned glass substrates. The obtained samples were used as a basis for 0, 10, 30, 50, and 100 nm Al layer evaporation. The attained ZnSe/Al grown films were used again for another 500 nm ZnSe layer deposition. The runs of deposition were supplied by 0.3 gm of ZnSe powder and 0.03 gm of Al. All these sequential evaporations were executed at 10^{-5} mbar vacuum pressure. The final films that represent Al sandwiched ZnSe films are indicated in Fig. 3.3.

Fig. 3.1. The 600 VCM evaporation system.

Fig. 3.2. The ZnSe and Al doped ZnSe thin films grown on a glass substrate.
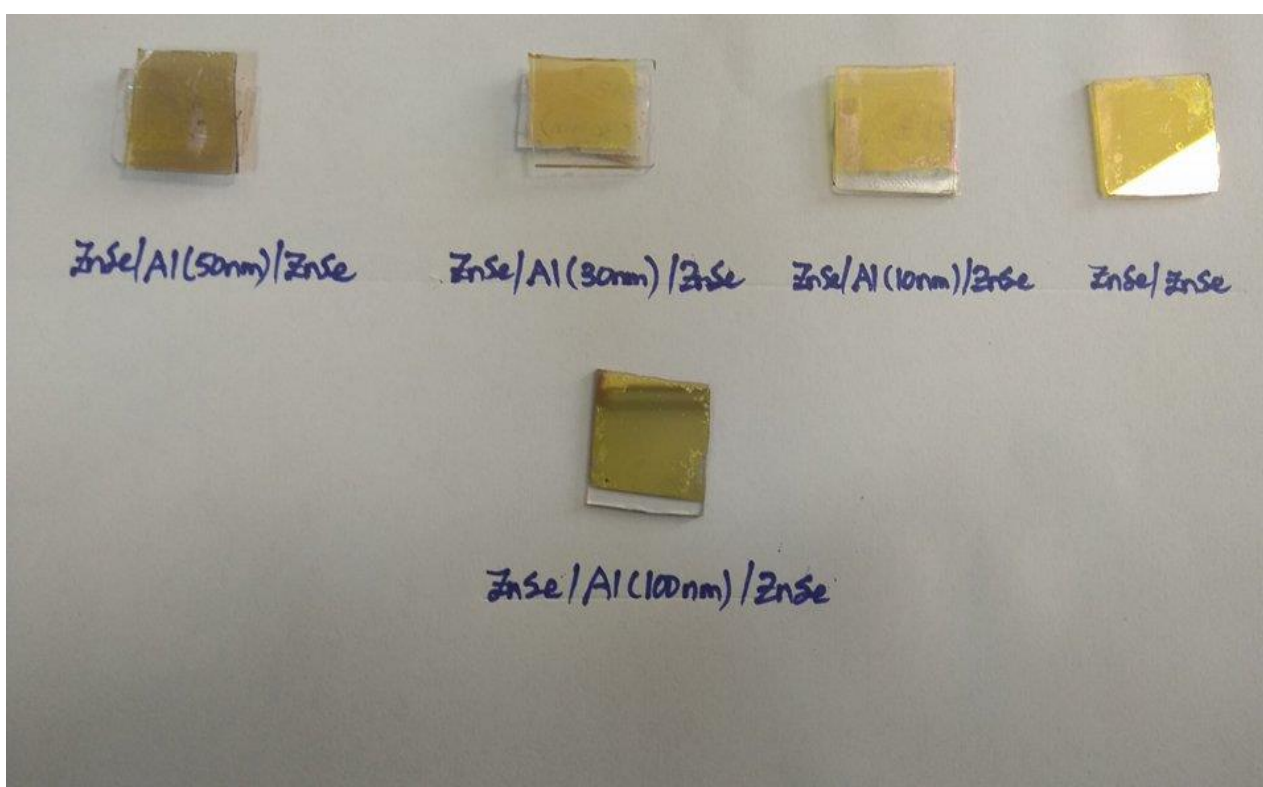
Fig. 3.3. The (0, 10, 30, 50, and 100) nm Al sandwiched ZnSe thin films grown on a glass substrates.

3.2 Thin Film Analysis

The grown films were tested using the hot probe technique, in order to determine the films type (*n*-type or *p*-type). As well as, ZnSe and Al doped ZnSe films were subjected to one hour thermal annealing at a temperature of 200 °C under a vacuum pressure of 10^{-4} mbar, to study the annealing effect on the properties of the grown samples. Scientific results can be acquired by performing structural, optical, and dielectric analysis. X-ray diffraction technique was used for structural investigations, and optical spectrophotometry was performed for optical and dielectric properties perception.

3.2.1 Hot Probe Technique

The experimental set-up of the hot probe technique is shown in Fig. 3.4. It was performed on pure ZnSe, Al doped ZnSe, and Al sandwiched ZnSe thin films using wires and digital multimeter. The hot probe was connected to the tested film and to the positive terminal of the multimeter, while the cold probe was connected to the film and to the negative terminal.

The multimeter read a positive current for the pure ZnSe, Al doped ZnSe, and 0, 10, 30, 50, and 100 nm Al sandwiched ZnSe thin films; this reveals that these films are of *n*-type due to the related positive current.

n-type semiconducting behavior in the Al doped ZnSe films may be referred to the substitution of Al to Zn in the ZnSe crystal matrix according to $Zn_{1-x}^{2+}Al_x^{3+}Se^{2-}[xe^-C.B]$. To compensate Al^{3+} valency we need to have free electrons in the conduction band.

As well as, n-type behavior may take place if Al goes into substitutional and interstitial positions the ZnSe crystal matrix, then it will have the form $Zn_{1-x}^{2+}Al_x^{3+}Al_y^{3+}Se^{2-}[(x+3y)e^-C.B]$.

n-type behavior may also occur due to Se^{2-} vacancies, which will create free electrons in the conduction band according to $Zn^{2+}Se_{1-\delta}^{2-}[2\delta e^{-}C.B]$.

In our films, both substitution of Al^{3+} to Zn^{2+} and/or the presence of Se^{2-} vacancies will create electrons in the conduction band of the grown crystal according to $Zn_{1-x}^{2+}Al_{x}^{3+}Se_{1-\delta}^{2-}[(x+2\delta)e^{-}C.B]$.
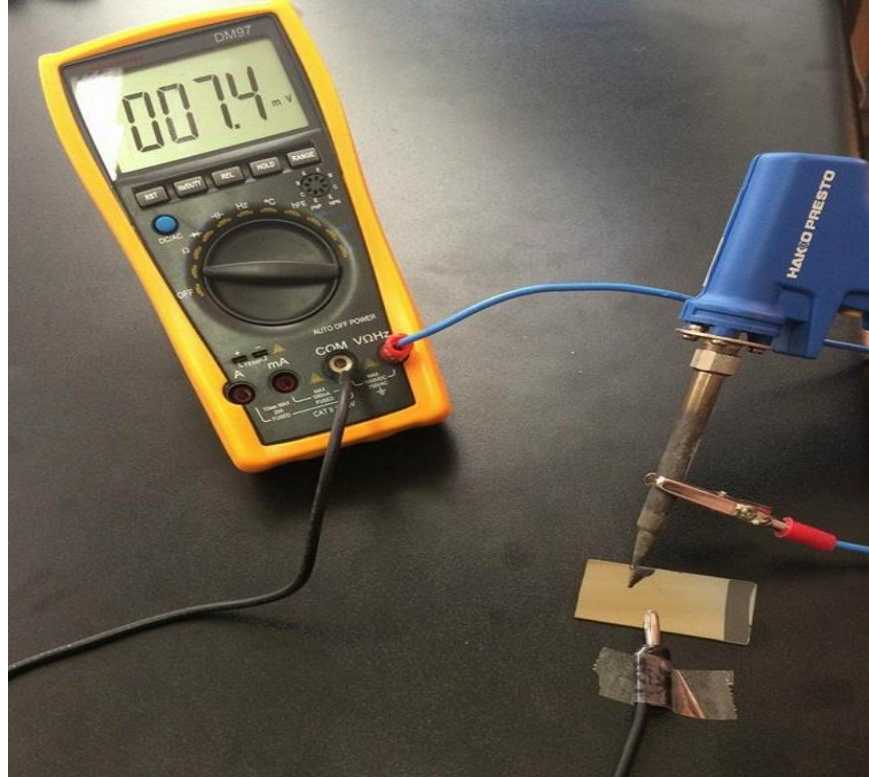
Fig. 3.4. The experimental set-up of the hot probe technique**.**

3.2.2 X-ray Measurements

The XRD spectrums of the ZnSe, Al doped, and Al sandwiched ZnSe thin films were characterized using Rigaku diffractometer presented in Fig. 3.5, which employs a characteristic K_{α} Cu X-rays of a 1.5418 A^{o} wavelength. The data involved in the film's X-ray spectrum were analyzed by using TREOR 92 and crystdiff programs.

Fig. 3.5. Rigaku diffractometer for the 1.542A° Cu XRD.

3.2.3 Optical Measurements

Thermo-scientific 300 ultraviolet-visible-near infrared spectrophotometer shown in Fig. 3.6 is used for ZnSe, Al doped, and Al sandwiched ZnSe film's transmittance and reflectance measuring. The VEEMAX II program was used for visualizing the examined films optical parameters. The spectrophotometer equipped Xe light source emits electromagnetic waves with wavelengths in the range 300-1100 nm. The reflectometer shown in Fig. 3.7 enables the optical measurements at an angle of incidence (15°) and a 0.1° step variable angles from 30° to 80°.

Fig. 3.6. Scientific 300 ultraviolet-visible-near infrared spectrophotometer.

Fig. 3.7. The reflectometer.

Chapter Four

Results and Discussion

4.1 Structural Analysis

4.1.1 Structural Analysis of Al Doped ZnSe and Pure ZnSe Thin Films

As deposited Al doped ZnSe (Al-ZnSe) film was observed to have an amorphous nature of growth as no peaks which refer to a specific plane of atoms observed in the diffractogram presented in Fig. 4.1. In an attempt to crystallize this film, it was annealed at 200 ℃ but the XRD spectrum didn't exhibit a structural transformation as shown in Fig. 4.1. The amorphous nature may be ascribed by the presence of point defects, which can conduct Al migration and diffusion through the as deposited and annealed Al doped ZnSe films. Primarily, Zn vacancies may be created during film nucleation; those can be filled with substitutional Al impurities. Also, Al diffusion may be assisted by the existence of the interstitial point defects. This will disturb the matrix linearity of the planes in the grains of the crystal and hence no XRD peaks can be observed.

While the annealed Al doped ZnSe film exhibits amorphous behavior, the undoped ZnSe film structural data illustrated in Fig. 4.2 verifies the ZnSe crystallinity even with or without heat treatment. It was previously reported that ZnSe films may have a cubic structure, hexagonal structure, or a mixture of the cubic and hexagonal phases, depending on the preparation conditions [29-31].

In the present work, the as grown semiconducting ZnSe film crystallizes in a zinc blende phase. The ZnSe cubic structure was reported in literature [32, 33]. However, Al doping destroys the cubic structure of the ZnSe and cause the formation of an amorphous film. This may be ascribed by the reason that the presented Al ions can substitute the Zn vacancies. This replacements is allowed provided that the Al ionic radius is (0.053 nm) [34] and the Zn ionic radius is (0.074 nm) [35].

The diffractogram of the as grown and 200 ºC annealed ZnSe thin films shows several peaks that were assigned to the film's cubic structure. The maximum peak (111) reveals a diffracted X-rays of intensities 825 and 482 a.u. (arbitrary unit). However, the local maximum (100) presented in the diffractogram has intensities of 548 and 271 a.u. for the as grown and annealed ZnSe thin films, respectively. It is obvious how 200 ºC annealing can affect the intensities of the diffracted X-rays at the maximum peaks.

A shift in the peaks toward higher 2θ is observed from the XRD spectra of the as grown and annealed ZnSe thin films; this shift is attributed to the preformed 200 ºC annealing. While, the maximum peak (111) is shifted from 28.1º to 28.3º, the local maximum (100) is observed to shift from 25.3º to 25.5º for the as grown and annealed ZnSe thin films, respectively.

200 ºC annealing can be considered for it's impact on the interplaner spacing (d), lattice constant (a), crystallite size (D), lattice strain (ε), stacking fault (SF %), and dislocation density (δ). These parameters were all evaluated using equations (2.4), (2.5), (2.13), (2.14), (2.15), and (2.16), respectively.

As shown in table 4.1, 200 ºC annealing causes an increase in the grain size (D) from 25.19 nm to 32.95 nm. However, the lattice constant (a) is observed to decrease from 0.5503 nm to 0.5465 nm for the as grown and annealed ZnSe thin films, respectively. Also, the calculated strain is observed to decrease from 5.9282×10^{-3} to 4.4999×10^{-3} upon annealing. The (111) dislocation density is found to decrease upon annealing too from 6.4156×10^{11} to 3.7484×10^{11}. Finally, 200 ºC annealing causes a decrease in the stacking fault of the (111) plane from 0.30004% to 0.22859%.
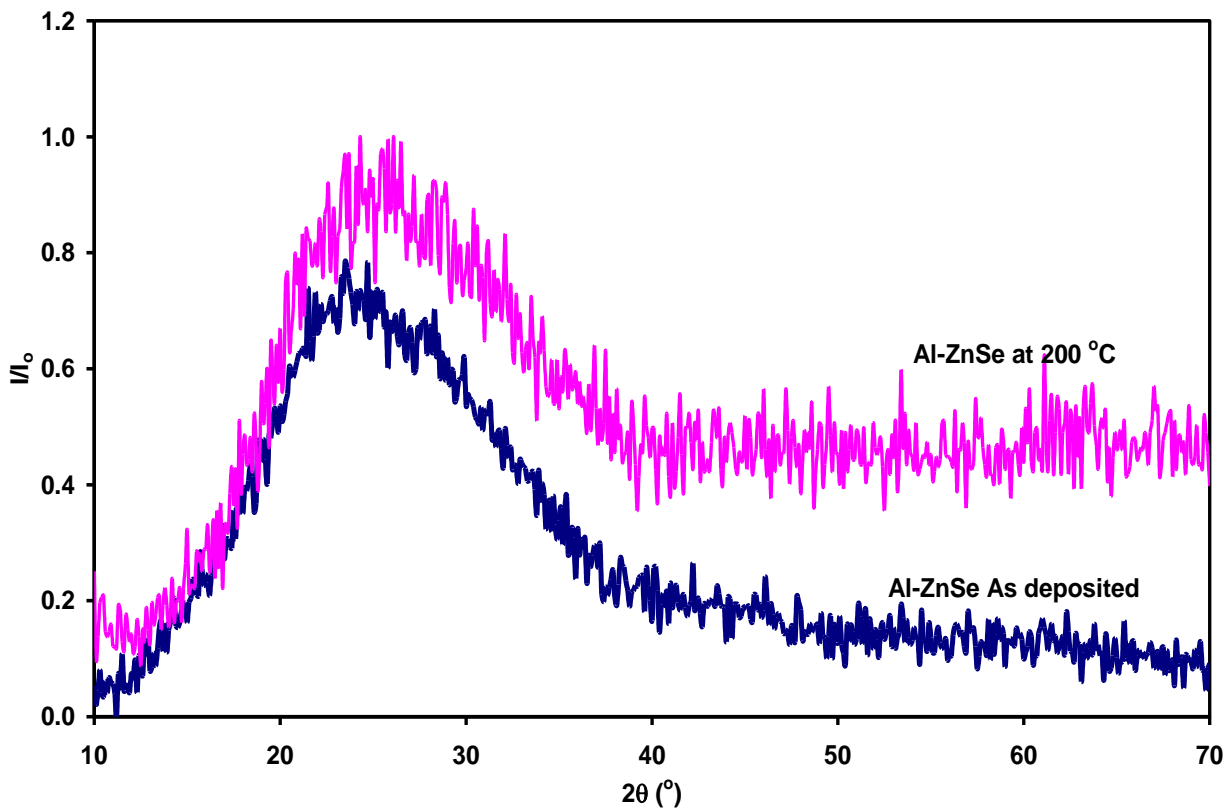
Fig. 4.1. The X-ray diffraction spectrum for the as deposited and 200 ºC annealed Al doped ZnSe thin films.

Fig. 4.2. The X-ray diffraction spectrum for the as deposited ZnSe, 200 °C annealed ZnSe, and 200 °C annealed Al doped ZnSe thin films.

Table 4.1

Structural properties of the as grown and 200 °C annealed ZnSe thin films.

Film type	D (nm)	d (nm)	a (nm)	ε x10^{-3}	δ x10^{11}	$SF\%$
As grown ZnSe	25.188	0.318	0.5503	5.9282	6.416	0.30004
annealed ZnSe	32.953	0.316	0.5465	4.4999	3.748	0.22859

4.1.2 Structural Analysis of the Al Sandwiched ZnSe Thin Films

The structural investigation of the Al sandwiched ZnSe thin films is performed in details. The films were prepared by inserting an Al layer with a thickness of 0, 10, 30, 50, and 100 nm between the two ZnSe layers. Thus, we have the samples ZnSe/ZnSe, ZnSe/Al (10 nm)/ZnSe, ZnSe/Al (30 nm)/ZnSe, ZnSe/Al (50 nm)/ZnSe, and ZnSe/Al (100 nm)/ZnSe symbolized by ZAlZ-0, ZAlZ-10, ZAlZ-30, ZAlZ-50, ZAlZ-100, respectively. Fig. 4.3 displays the XRD patterns of these sandwiched films.

It is seen from Fig. 4.2 and 4.3 that Al sandwiched ZnSe thin films show the same diffraction spectra observed in the as grown and annealed ZnSe thin films. This means that Al nanosandwiching doesn't change the ZnSe crystal structure.

The XRD spectrum of the Al sandwiched ZnSe thin films seen in Fig. 4.3 reveals a number of sharp peaks, that referred to the zinc blende crystal structure. The peaks were observed to be more intense when Al thickness increases. The maximum reflection peak shows intensity values of (698, 895, 915, 1174, and 932) a.u. as the Al thickness is increased from (0, 10, 30, 50, and reaches 100) nm, respectively. While, the local maximum exhibits intensity values of (437,501, 639, 660, 654) a.u. as the Al thickness is increased from (0, 10, 30, 50, and reaches 100) nm, respectively. The increase in the intensity of the diffraction peaks can be attributed to the Al effect on the structural properties of the ZnSe sandwiched films. This increase in the diffracted intensity predicts an increase in the grain size of the sandwiched films and a decrease in the film's dislocation density and stalking faults. So a crystallinity enhancement is observed with Al sandwiching.

The XRD spectrum of the pure ZnSe film reveals slightly intensive peaks as indicated in Fig. 4.3. However, this is not the case in (50 and 100) nm Al sandwiching, where peaks are strongly maximized.
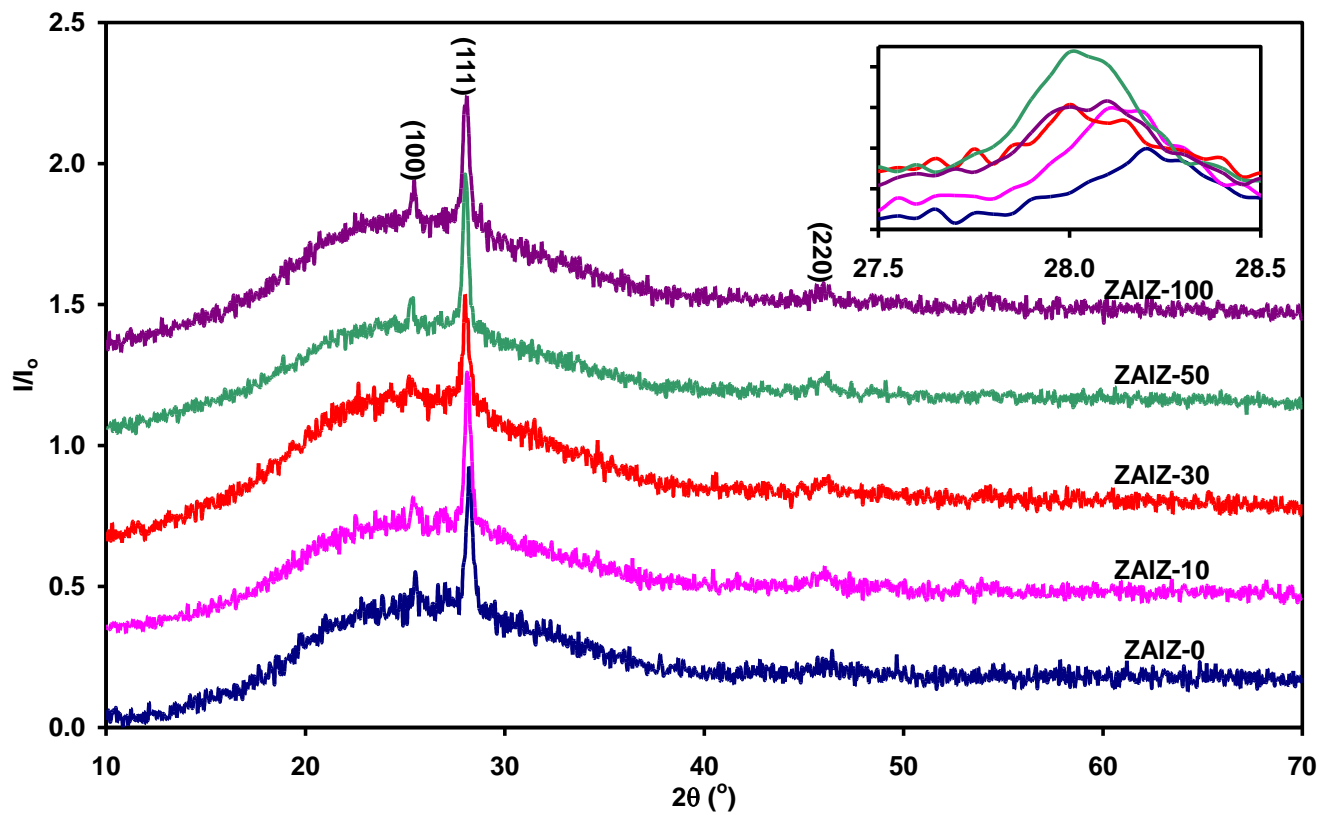
Fig. 4.3. The X-ray diffraction patterns of the (0, 10, 30, 50, and 100) nm Al sandwiched ZnSe thin films.

The raised Al sandwiching level ensures crystallinity improvement; this may be referred to the stabilized impurities at the sites of the vacancies and interstitial defects [36, 37]. Moreover, the increase in the intensity may be referred to the atomic planes rearrangement, grains formation, and amputation of residual stresses.

It was perceived that the peaks width of the sandwiched films contracts with increasing Al concentration. In addition, the maximum peak (111) appears at 2θ is indicated as a sub graph in Fig. 4.3. The (111) peak is shifted toward lower values (28.20º, 28.15º, 28.00º, 28.00º, and 27.95º) as the Al thickness is increased from (0, 10, 30, 50, and reaches 100) nm, respectively. While the local maximum (100) is shifted from (25.55º, 25.40º, 25.35º, 25.30º, 25.30º) as the Al thickness has increased from (0, 10, 30, 50, and reaches 100) nm, respectively. This shift toward lower 2θ may be attributed to the ions that substitute Zn [38]. The structural analysis using "TREOR 92" and "crystdiff" software package ensures that Al sandwiched ZnSe thin film's structure is predominantly of a cubic type. The mentioned maximum peak is presented by (111) indices, that correspond to (111) plane of the ZnSe zinc blende phase. However, the local maxima expressed by (100) indices refers to the hexagonal ZnSe structure. The total shift in the major and minor peaks is observed to be equal. The preferred orientation tendency in the zinc blende structure is along (111) axis. The orientation tendency can be determined by evaluating the orientation factor α using (Wang et al 2010) formula, $\alpha_{(111)}=I_{(111)}/$(sum of the intensities of the other distinct peaks). The (111) orientation tendency can be ascribed to the fact that the available activation energy is enough for atoms to set in its lattice site [39].

A structural comparison between Al doped ZnSe and Al sandwiched ZnSe techniques was also carried out. The films grown by the first technique posses an amorphous XRD patterns and this behavior was earlier extensively explained. However, the sandwiched films patterns reflect a zinc blende structure.

This crystallinity could probably be due to the continuity of the Al plate that is sandwiched between the ZnSe layers. Thus, less Al ions can substitute Zn ions.

To form a comprehensive view about the structural properties of the Al sandwiched ZnSe thin films, the interplaner crystal spacing (*d*), lattice constant (*a*), crystallite size (*D*), lattice strain (*ε*), stacking fault (*SF* %), and dislocation density (*δ*) were evaluated. The calculated parameters are illustrated in the Table. 4.2, and plotted in Fig. 4.4 & 4.5.

As the table 4.2 shows, Al sandwiching promotes an increase in the crystallite size from 21.41 nm for the ZnSe/ZnSe film to 27.61 nm for the ZnSe/Al(100 nm)/ZnSe film. A similar trend is recorded in the values of the lattice constant (*a*), which is found to increase from 0.5484 nm for the ZnSe/ZnSe film to 0.5522 nm for the ZnSe/Al(30 nm)/ZnSe and ZnSe/Al(50 nm)/ZnSe films.

However, the lattice strain decreases with Al sandwiching from 6.949×10^{-3} for the ZnSe/ZnSe film to 6.650×10^{-3}, 5.600×10^{-3}, and 5.435×10^{-3} for the ZnSe/Al(30 nm)/ZnSe, ZnSe/Al(50 nm)/ZnSe, and ZnSe/Al(100 nm)/ZnSe film, respectively. The dislocation density of the (111) plane is reduced from 8.876×10^{11} for the ZnSe/ZnSe sample to 5.337×10^{11} for the ZnSe/Al(100 nm)/ZnSe sample, and stacking fault of the (111) planes is observed to decrease from 0.3523% for the ZnSe/ZnSe sample to 0.2743% for the ZnSe/Al(100 nm)/ZnSe sample.

The main reason for the crystallite size, inter-planer distance, and lattice constants enlargements with Al sandwiching may be referred to Al ions incorporation into lattice vacancies by substitution as reported in Al doped ZnO [40]. This indication is also predictable from the decreasing defect density with increasing Al thickness. The increase in the crystallite size may also be ascribed to columnar grain growth in the films [41].

Table 4.2

Structural properties of Al sandwiched ZnSe thin films.

Doping level (nm)	D (nm)	d (nm)	a (nm)	ε x10^{-3}	δ x10^{11}	$SF\%$
0	21.415	0.316	0.5484	6.9486	8.876	0.3523
10	21.961	0.317	0.5493	6.7874	8.439	0.3438
30	22.532	0.138	0.5522	6.6503	8.017	0.3359
50	26.757	0.138	0.5522	5.6002	5.685	0.2829
100	27.617	0.139	0.5532	5.4353	5.337	0.2743
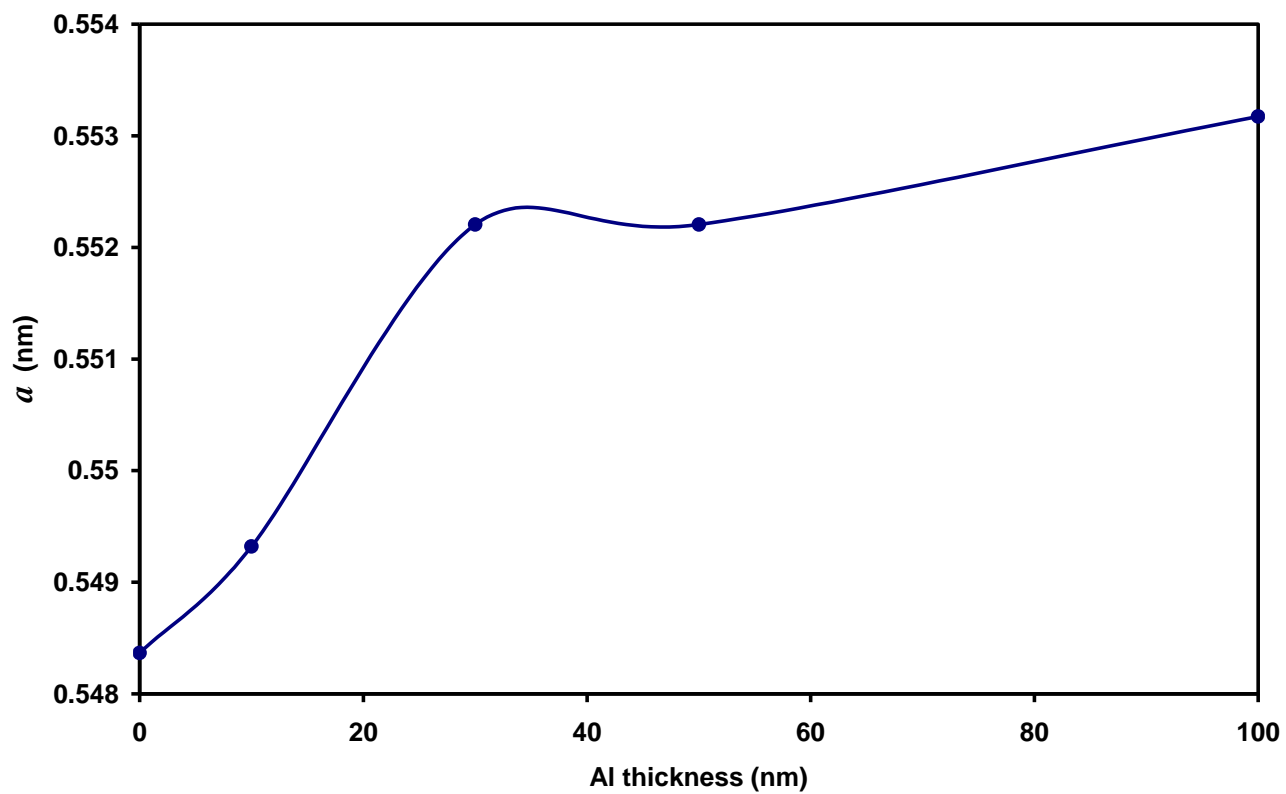
Fig. 4.4. Lattice constant *a* plotted as a function of Al sandwiching level.
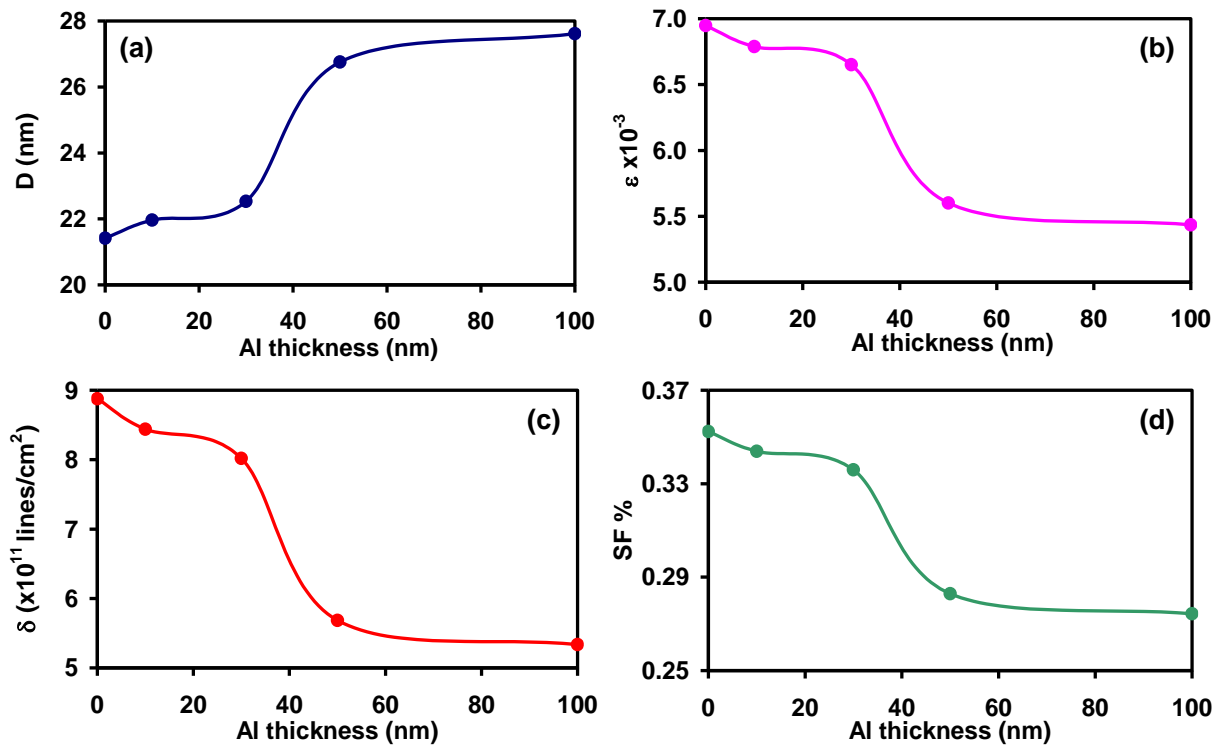
Fig. 4.5. (a) Crystallite size, (b) lattice strain, (c) dislocation density, and (d) stacking fault were plotted as a function of Al sandwiching level.

Besides, the interplaner distance growth can explain the shift in the sharp peaks toward lower glancing angles, when Al thickness increases from 0 to 100 nm according to Bragg's law, which is expressed in equation (2.5).

The obtained results imply the decline in the strain values with Al doping. The explanation of this bonds shrinking could be probably explained by the ability of Zn ions to be replaced by Al ions, then Al-Se bonds (2.58 A^o) [42] may be formed. In this case, the formed bonds are shorter than Zn-Zn and Se-Se bonds (3.85 A^o and 4.11 A^o) [43]. The sharp decrease in the stacking fault and dislocation density prove the crystallinity enhancement with raising the Al content of the sandwiched films [44].

Our structural analysis for the Aluminum sandwiched ZnSe films can be compared with the reported structural properties of metal doped ZnSe thin films rather than Al. Fe doped ZnSe thin film and Cu doped quantum dot were investigated previously in literature. An increase in the crystallite size was reported with increasing the doping percent above 1% in Fe doped ZnSe thin films. It was reported that Fe ions may replace the Zn in the grown ZnSe film [45]. A decrease in the lattice strain and dislocation density with doping was also reported in Fe doped ZnSe thin film [32]. It was reported that the crystallite size of Cu: ZnSe quantum dot calculated using the Sherrer's equation is larger than that attained for the undoped ZnSe quantum dot [46, 47].

4.1.3 Nucleation and Growth of the Al doped and Al Sandwiched ZnSe Thin Films

The structural properties of the doped as well as the nanosandwiched ZnSe films can be understood by investigating the growth of the two doping mechanisms introduced in Fig. 4.6. In Al doping technique, which is shown in Fig. 4.6 (a), Al atoms are evaporated concurrently with the evaporation of the ZnSe molecules. The velocity of both particles (Al and ZnSe) was controlled by the heating temperature of the boats.

While in sandwiching mechanism, which is shown in Fig. 4.6 (b), ZnSe and Al were deposited layer by layer in different growth cycles. In the first nucleation cycle, ZnSe molecule in its vapor phase reaches the glass substrate, and condenses rapidly. It may re-evaporate or diffuse along the substrate. The diffused ZnSe molecule may be adsorbed or re-evaporate. The increased number of adsorbed ZnSe molecules leads to the formation of the embryo, which can grow into a nucleus if its size is larger than a critical size. Nucleus then can grow into a crystal which in turn can form grains, in a process known as a heterogeneous nucleation. In the second nucleation cycle, a molten Al atom condenses from the vapor phase, the raised amount of adsorbed Al atoms leads to grow a layer of Al grains on the top of ZnSe layer. In the last nucleation cycle, again by heterogeneous nucleation a ZnSe layer covers the pre-deposited Al layer.

The layer by layer growth mode predominate the island and layer-plus-island modes, because the interaction between glass substrate and ZnSe molecules is stronger than between neighboring ZnSe molecules, and the interaction between Al atoms and ZnSe atoms is stronger than between Al neighboring atoms or ZnSe neighboring molecules.
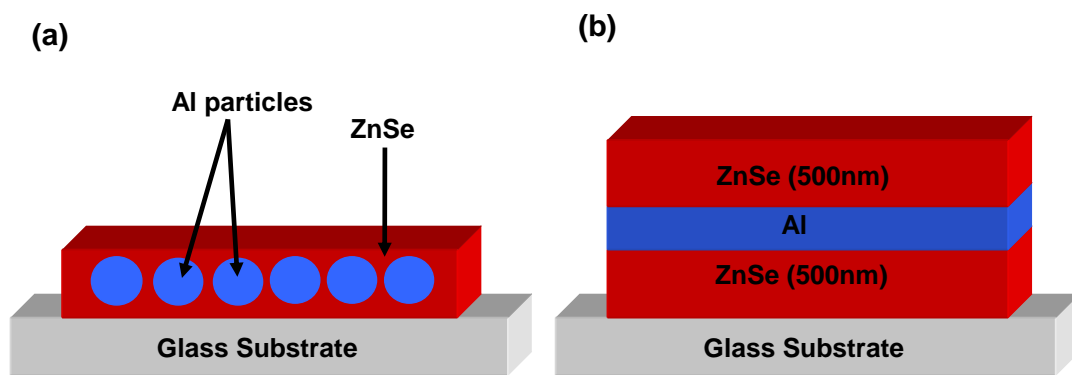
Fig. 4.6. Schematic graph of (a) Al doped ZnSe thin films and (b) Al sandwiched ZnSe thin films.

4.1.4 Energy Dispersive X-ray Analysis

The energy dispersive X-ray measurement for the Al doped ZnSe is shown in Fig. 4.7. In accordance with the figure, the spectral data that are collected from the surface of the film and substrate as well, the Al doped ZnSe film is atomically composed of 13.16% Al, 47.02% Zn and 39.82% Se. On the other hand the undoped ZnSe films reveal an atomic content of 51.36% Zn and 49.82% Se as shown in Table 4.3. The significant decrease in the content of Zn before and after doping and the change in the content of Se upon doping indicate that the Al atoms are not substituting the Zn atoms unless we think that the pure samples prefer the growth of ZnSe with excess of Zn of 1.54% and the preferred phase of growth of zinc selenide in the presence of aluminum is Zn_3Se_2. The latter case indicate that assuming all Al was replacing Zn then the atomic content is 60.18% Zn and 39.82% Se.

Table 4.3

EDAX data for the pure and Al doped ZnSe thin films.

Atom	ZnSe atomic ratios	Al doped ZnSe atomic ratios
Al	0%	13.16%
Zn	51.36%	47.02%
Se	48.64%	39.82%
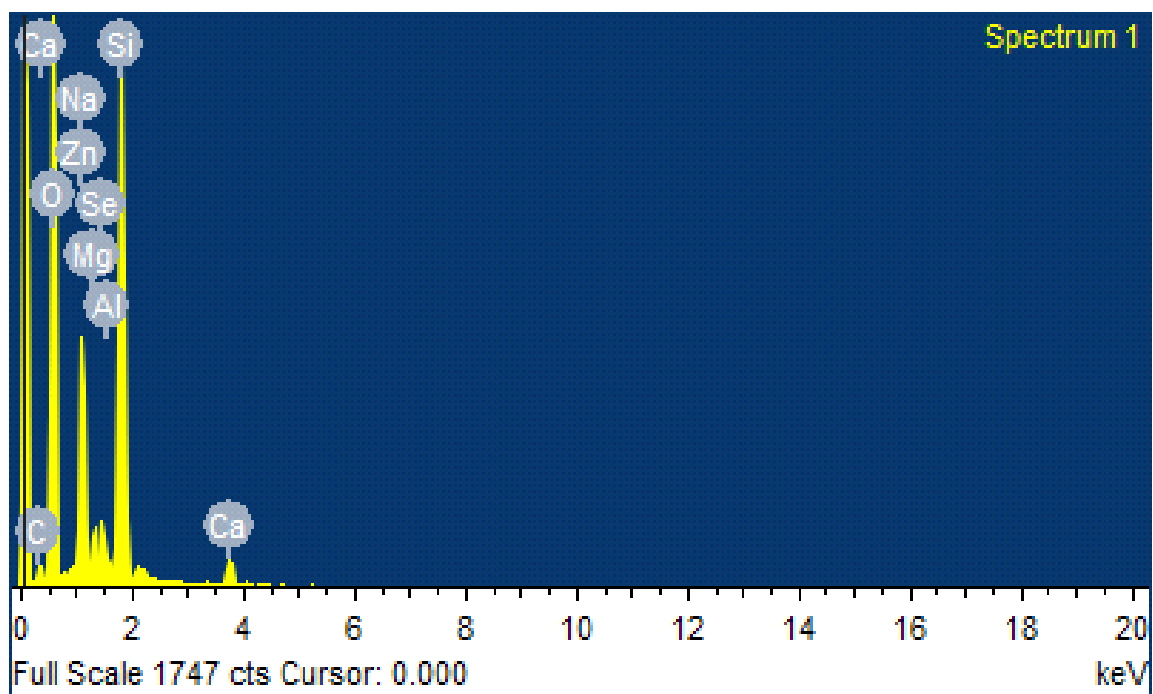
Fig. 4.7. EDAX image of Al doped ZnSe thin film grown on a glass substrate.

4.2 Optical Analysis

4.2.1 Optical Analysis of ZnSe and Al Doped ZnSe Thin films

Fig. 4.8 and 4.9 illustrate the spectral transmittance and reflectance for the as deposited and 200 ^{o}C annealed ZnSe and Al doped ZnSe thin films, respectively. The transmittance curve of the annealed ZnSe film shows a transmittance lower than the as grown ZnSe film along the UV-VIS-NIR range. The transparency for both films (as deposited and annealed ZnSe) increases with increasing the incident light wavelength up to 710 nm and 668 nm for the as deposited and annealed ZnSe thin films, respectively. After that, transparency decreases for higher wavelength range. However, the highest transmittance is assigned to the as deposited ZnSe film with a 93.49% transmittance at 704 nm.

On the other hand, compared to the as deposited Al doped ZnSe the annealed Al doped ZnSe film shows a lower transmittance in the UV and visible range (up to 556 nm). By considering the as deposited and annealed Al doped ZnSe, both films show a transmittance that increases with increasing the wavelength of the incident light. It is observed from Fig. 4.8 (b) that for wavelengths greater than 700 nm, the as grown and annealed Al doped ZnSe films turn out to be transparent with a transmittance of 87.06%.

The reflectance curve of the annealed ZnSe film is observed to decrease in UV and visible spectral ranges compared to the as deposited ZnSe film. As well as, the annealed Al doped sample exhibits a lower reflectance extends along the UV-VIS-NIR ranges relative to the as deposited Al doped ZnSe.

The spectrophotometric transmittance of the ZnSe thin films prepared by chemical bath deposition was reported to decrease with air annealing at 373, 473, 573, and 673 K [48]. In another study, the optical constants of the ZnSe thin films were examined as the pulsed laser annealing at 15, 20 to 30 W was performed.
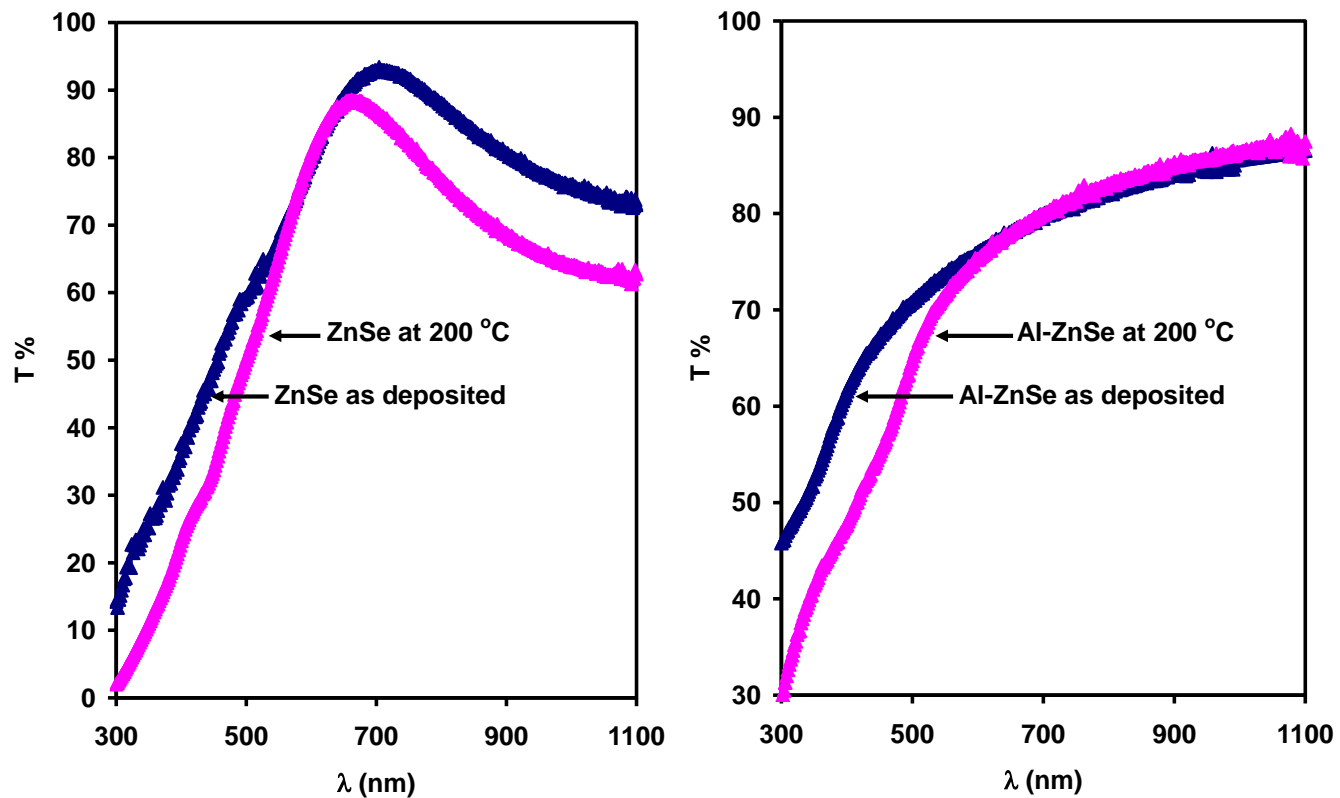
Fig. 4.8. The optical transmission (*T* %) versus the incident light wavelength (λ) for the as deposited and annealed (a) ZnSe and, (b) Al doped ZnSe thin films.
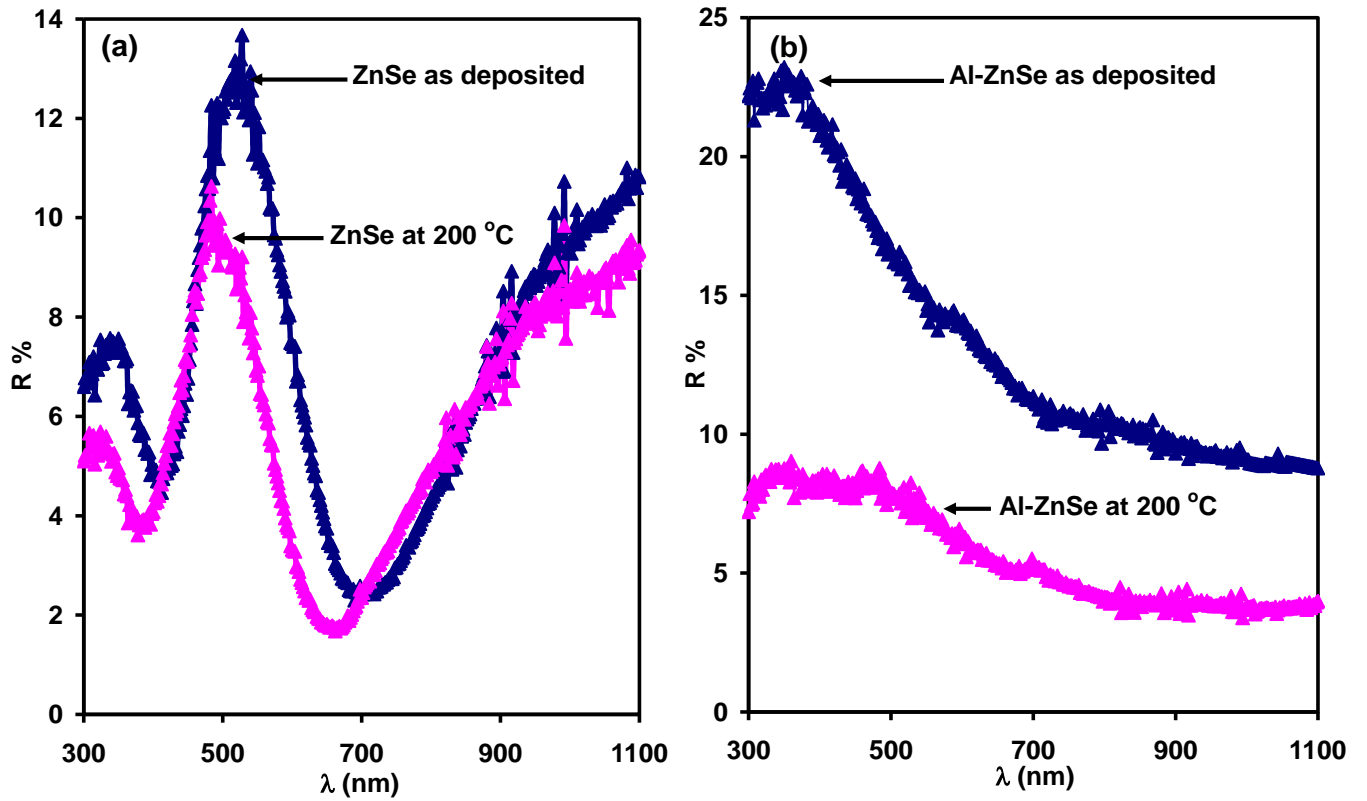
Fig. 4.9. The optical reflection (R %) versus the incident light wavelength (λ) for the as deposited and annealed (a) ZnSe and, (b) Al doped ZnSe thin films.

A momentary decrease in ZnSe films transparency and reflectance by annealing processes was articulated [49]. Optical properties of ZnSe thin films annealed at various annealing temperatures (273, 333, and 473) K were investigated in literature. A decrease in the ZnSe transmittance was observed with annealing. The highest transmittance was associated with the ZnSe film annealed at 273 K [50].

Compared to as deposited films, the lower transparency and reflectivity observed for the thermally annealed ZnSe and Al doped ZnSe films may be credited to the increase in light absorption which activates electron migration from the valence to conduction band [51].

Another reason that transmittance and reflectance are lower in the annealed films can be assigned to light scattering, which is associated with the annealed films rough surfaces [52]. The nanostructured ZnSe thin films roughness was observed to increase from 1.5 nm to 2.5 nm for annealing at 100 and 300 $^{\circ}$C, respectively [53].

To reveal more accurate picture about the optical dynamics of the ZnSe and Al doped ZnSe thin films, absorbance (A) of the grown films was calculated using equation (2.30). The absorbance (A) is then linked to the absorption coefficient (α) through equation (2.31).

Absorption coefficient spectrum was plotted in Fig. 4.10 in order to analyze and visualize the influence of the 200 $^{\circ}$C annealing on the optical parameters of the ZnSe and Al doped ZnSe thin films.

An increase in the ZnSe and Al doped ZnSe absorption upon annealing can be observed from Fig. 4.10 (a) and (b), respectively. In details, the annealed ZnSe thin film shows an increase in the absorption coefficient along the UV-VIS-NIR ranges. On the other hand, the absorption spectra of the annealed Al doped ZnSe thin film exhibits a UV-VIS-NIR increase too.
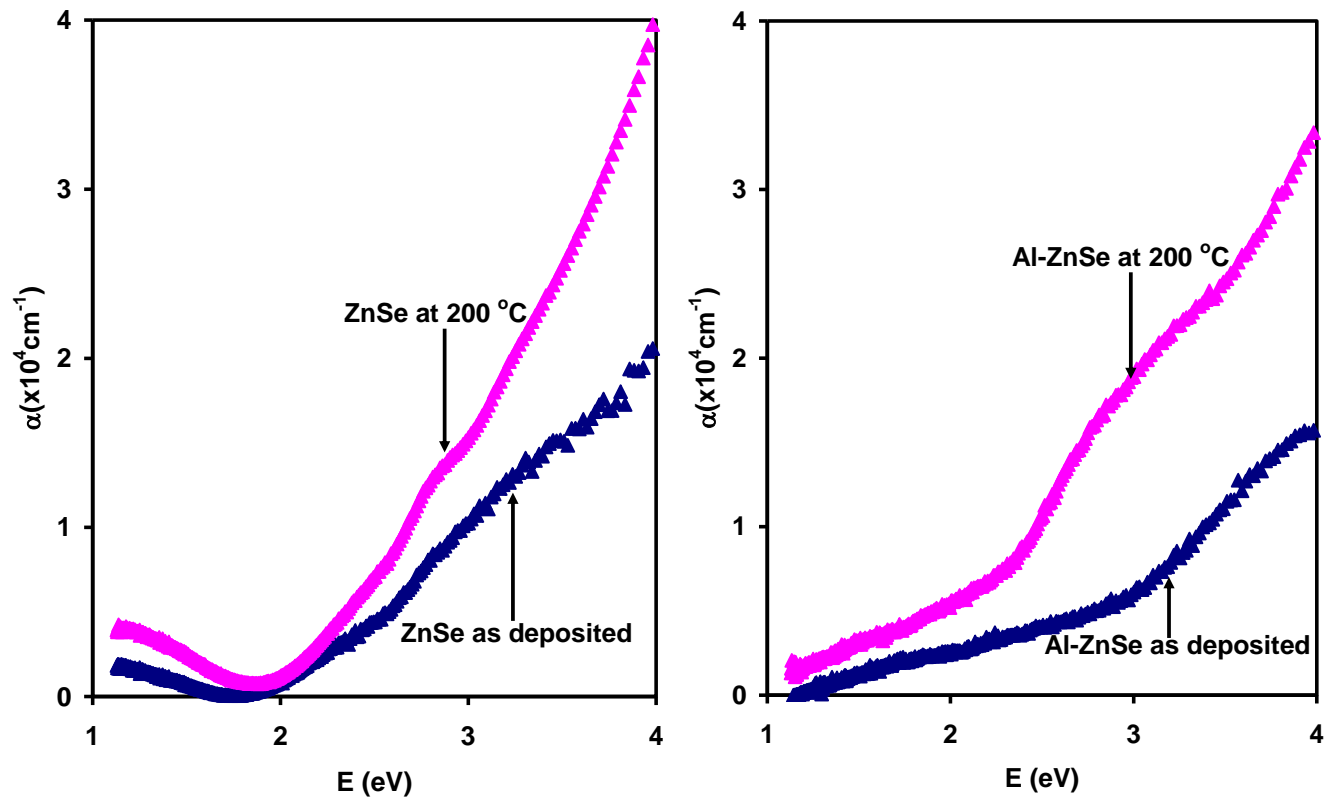
Fig. 4.10. The absorption coefficient (α) versus photon energy (E) for the as deposited and annealed (a) ZnSe and, (b) Al doped ZnSe thin films.

This increase in the absorption coefficient is expected, since the annealed ZnSe and Al doped ZnSe thin films were previously analyzed to show a transmittance and reflectance attenuation upon annealing.

The 200 °C annealed ZnSe thin films reveal an evident blue shift in the absorption edge (below 2 eV). This behavior was reported in Cu_2O thin films, which displayed an absorption blue shift with increasing the temperature of annealing [54].

For incident photon energies lower than the band gap, an exponentially increasing absorption edge was informed since Al impurities induce band tails formation in the gap [27] according to equation (2.56),

$$\alpha = \alpha_o e^{\frac{E}{E_e}} \tag{4.1}$$

Where α_0 is the pre-exponential factor and E_e is the width of the band tails of the localized states. The width of the as grown and annealed Al doped ZnSe samples band tails were estimated from Fig. 4.11 lines slope. The estimated band tails width is 0.42 eV and 0.77 eV for the as grown and annealed films, respectively. It is clear how 200 °C annealing can manipulate the transition width of the band tails.

Evaluation of the energy gap E_g can be accomplished by employing the values of the optical absorption coefficient spectrum through Tauc equation (2.57), which presented in chapter 2.

$$(\alpha E)^{1/p} = B(E - E_g) \tag{4.2}$$

Where E is the incident photon energy, p is a parameter that typifies the absorption process, B is a constant that is mainly proportional to the hole and electron effective masses, and E_g is the band gap energy.
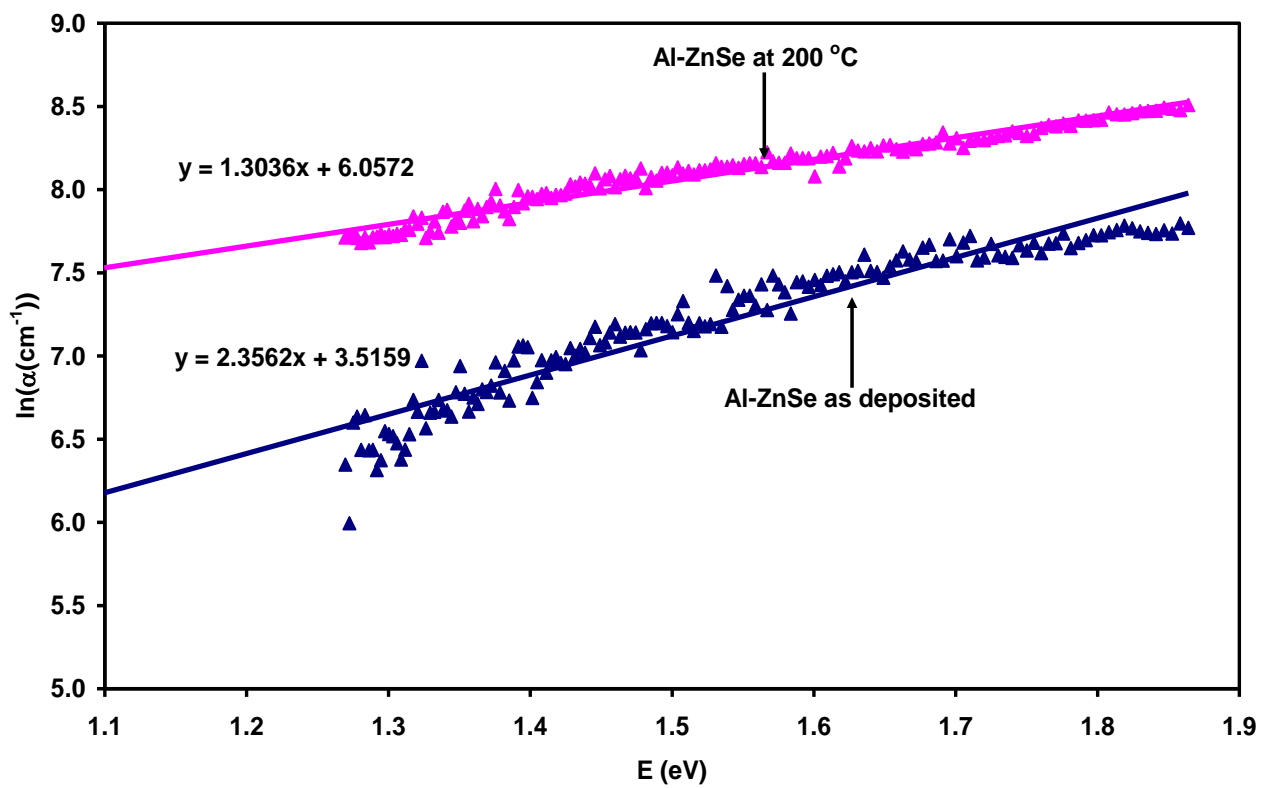
Fig. 4.11. ($ln(\alpha)$) versus photon energy (E) for the as grown and annealed Al doped ZnSe thin films.

The index p can have the values 2, 1/2, 3, and 3/2 for indirect allowed, direct allowed, indirect forbidden, and direct forbidden electronic transition, respectively.

The plot $(\alpha E)^2$ versus photon energy E proposes a direct allowed transition. It was chosen to be the most probable transition type in the as grown and annealed ZnSe and Al doped ZnSe films. $(\alpha E)^2$ plots were selected because they involves the widest range of linear data. Then, the values of the optical energy gap were determined by extrapolating the linear portions of the $(\alpha E)^2$ plots of the as grown and annealed ZnSe and Al doped ZnSe films.

The influence of the thermal annealing and Al doping on the optical energy gap can be analyzed in the light of the obtained energy gaps. The intercepts shown in Fig. 4.12 (a) and (b) illustrate the values of the ZnSe band gap such that the optical gaps are 2.67 eV and 2.45 eV for the as grown and annealed ZnSe films, respectively. As well as, 3.19 eV and 2.50 eV for the as grown and annealed Al doped ZnSe films, respectively. The decrease in the ZnSe energy gap (red shifted) was ascribed to the improvement in crystalline nature and to the increase in the grain size. It is also may be referred to the related increase in the surface free energy via annealing [55]. In addition, the decrease in the ZnSe lattice defects when annealed results in an internal stress formation at grain boundaries of the nano-structured ZnSe thin film this may reduce the gap [56, 57]. Moreover, annealing supplies the ZnSe lattice with thermal energy, which disturbs the valence band delocalized electrons and motivates a shift in the band's relative site [58]. Al doping promotes energy gap enhancement from 2.67 eV for the ZnSe thin film to 3.19 eV for the Al doped ZnSe. This behavior was reported in Mg doped ZnO films prepared by sputtering, where the energy gap is confirmed to increase upon doping [59]. In similar works, the increase in the energy gap with doping was explained by the degraded crystallinity [60].
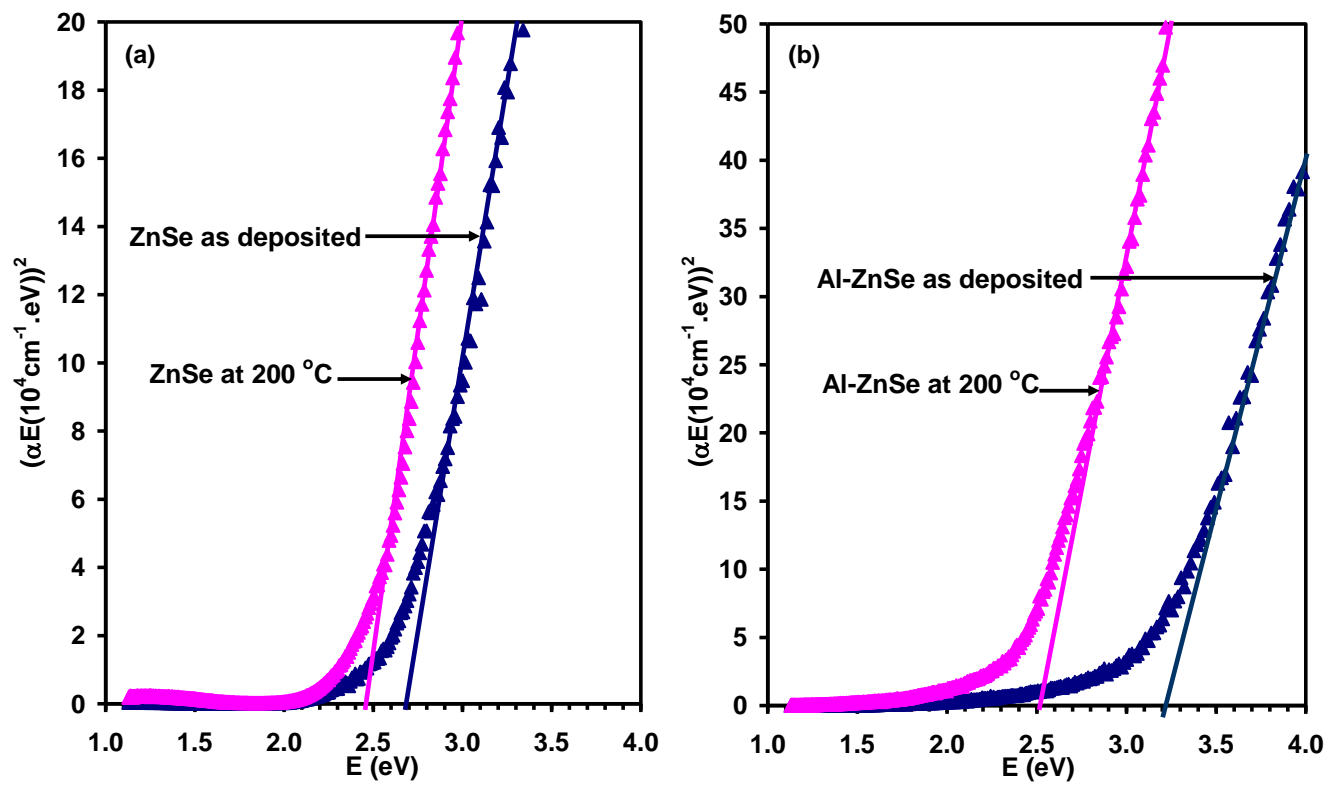
Fig. 4.12. $(\alpha E)^2$ versus photon energy (E) for the as deposited and annealed (a) ZnSe and, (b) Al doped ZnSe thin films.

4.2.2 Optical Analysis of Al Sandwiched ZnSe Thin Films

The transmittance and reflectance for Al nanosandwiched ZnSe thin films, presented in Fig. 4.13 and Fig. 4.14, were measured in a wide spectral range that extends from 300 nm to 1100 nm.

An evident Al impact on the films transmittance can be observed. A general overview into Fig. 4.13, transmittance spectrum of the Al sandwiched films reveals a transmittance attenuation. A clear change in the transmittance of the pure ZnSe films relative to the sandwiched films is observed. Particularly, when a 10 nm Al layer is inserted a consequent decrease in transmittance is recorded. The explanation may be facilitated by the fact that increasing the thickness of the metallic layer raises the film reflectance and absorbance.

The peaks that observed in the transmittance spectra, suggest a provoked light interference fringes in the thin film layers [61], which may propose higher absorption coefficients due to the large films thicknesses as well as the high refractive index. The intensity of the interference peak diminishes at the same time as the Al content sets up. Beyond, the presence of interference peaks in the graphed transmittance spectrum of the pure and Al sandwiched ZnSe films corroborate that the synthesized films are of harmonized thickness. Four fringes were reported in the as grown and pulsed laser treated ZnSe thin films transmittance spectra, which proves the good quality of the fabricated films [62].

The sandwiched films of the current work illustrate an ordered blue transmittance shift towards higher frequencies; this shift confirms the transmittance-Al thickness dependence. The blue shift can be attributed to crystallinity improvement and to the increase in the grain size [63] with Al sandwiching as was observed in the current work XRD analysis.
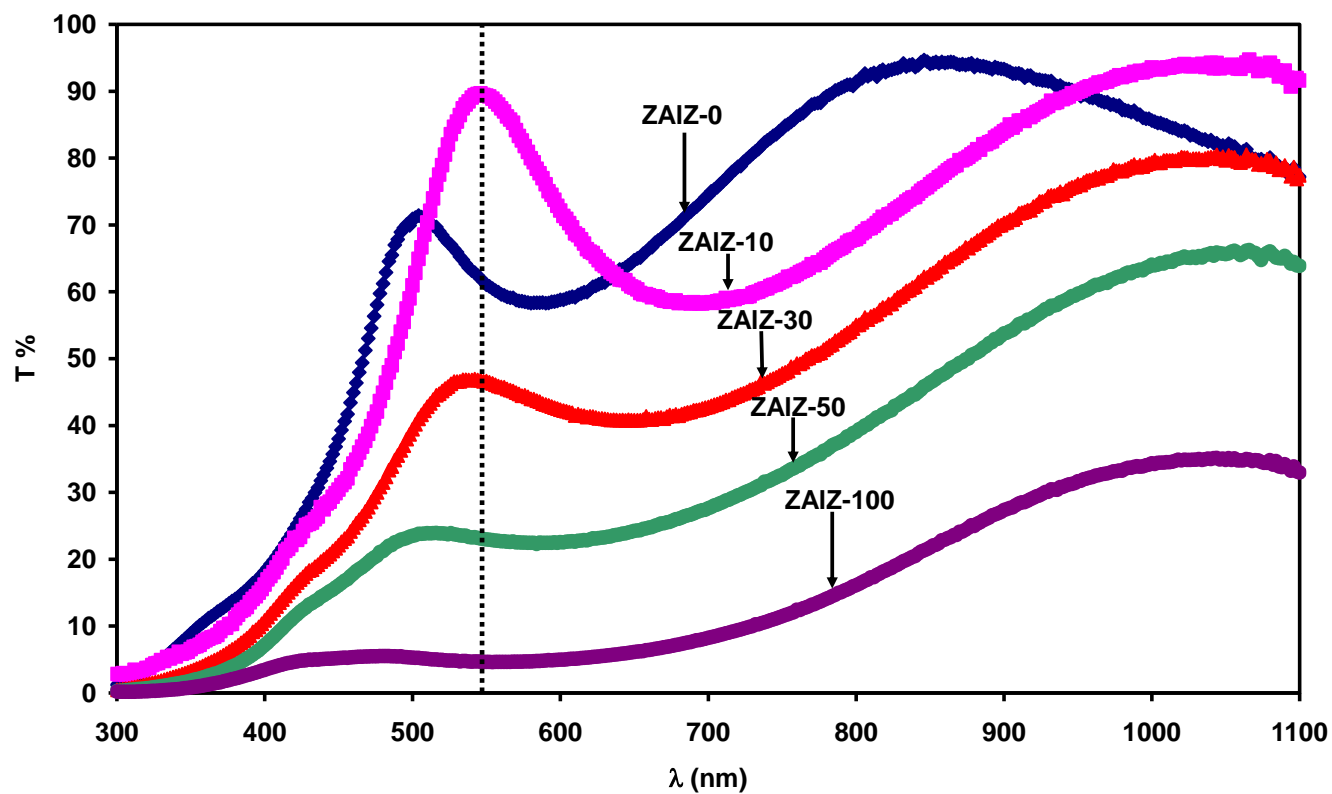
Fig. 4.13. The optical transmission (T %) versus the incident light wavelength (λ) for the Al sandwiched ZnSe thin films.

Comparatively, it was reported that a Lanthanum doped ZnSe nano-particles transmission spectral peaks exhibit blue shift compared to pure ZnSe nano-particles [64]. Moreover, a hast passivated ZnSe nanorods demonstrate a blue shift relative to the bulk ZnSe, which was assigned to electrons and holes quantum confinement in a small size [65].

On the other hand, the reflectance spectrum of the sandwiched films shown in Fig. 4.14 owns multiple maxima and minima, which come about as a result of light interference too.

A difference in the reflectance values of the sandwiched films, as observed in Fig. 4.14, may be referred to the difference in the Al layer thickness involved in each sandwiched film.

In Details, the 100 nm Al sandwiched ZnSe thin film has a good reflectance that reaches 50% at a wavelength of 548 nm, the high reflectance of the 100 nm Al sandwiched film may be referred to the large Al atom concentrations.

Whereas, the 50 nm Al sandwiched ZnSe thin film has a reflectance maxima of 27.45% at a wavelength of 628 nm. Also, the 30 nm Al sandwiched ZnSe thin film posses a reflectance maxima of 25.05% at a wavelength of 704 nm.

The more thick the Al layer in the sandwiched films the more atoms that can oscillate against the incident electromagnetic waves, which can radiate a new electromagnetic waves that have the same energy but different amplitude. The higher the amplitude of the reflected waves the larger the value of the reflection coefficient.
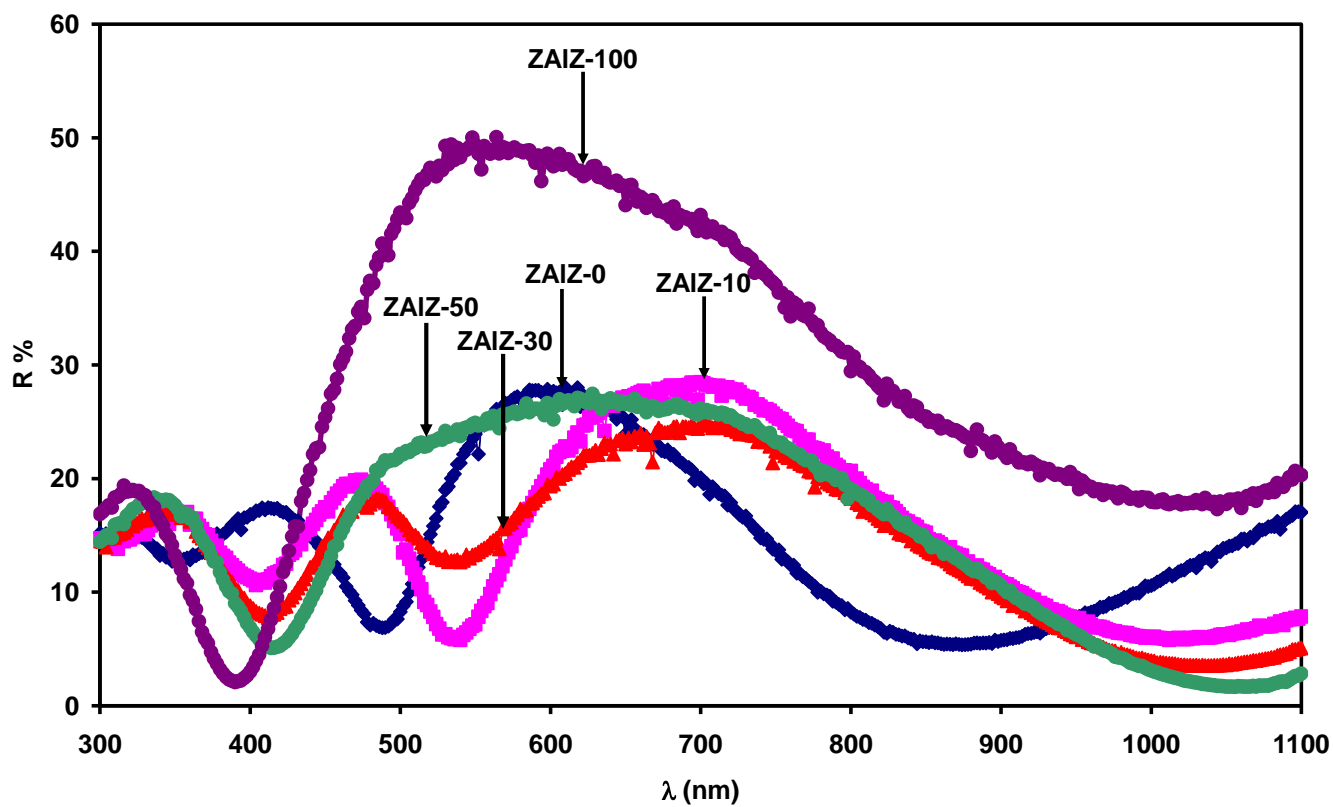
Fig. 4.14. The optical reflection (R %) versus the incident light wavelength (λ) for the Al sandwiched ZnSe thin films.

The influence of the Al sandwiching on the optical performance of the ZnSe thin films can be understood by analyzing the absorption coefficient spectrum. Fig. 4.15 shows a dramatic increase in the absorbance values of the sandwiched films while upgrading Al thickness.

The increased Al atom concentrations give rise to an enlargement in the number of unbound free electrons, this conduce a higher band to band absorption values, and permits more and more electronic transitions.

A sharp increase in the absorption coefficient of the pure ZnSe film is activated at photon energy larger than 3.5 eV. However, the absorption coefficient of the 10, 30, 50, and 100 nm Al layers deposited between the two 500 nm ZnSe layers has a sharp increase at photon energies larger than 2.98, 2.93, 2.90, and 2.89 eV, respectively.

Two regions of high and low absorbencies can be characterized; the high absorbance zone is established in the range from 2.5 to 4.13 eV, which referred to band-to-band UV electronic transitions, and the low absorbance zone extends from 1.13 to 2.5 eV, this zone is associated with electronic transition between band tails.

Al impurities and structural defects were reported to induce band tails formation. The band tails assist absorption at low frequencies, which would be the most probable reason for electronic transition regardless the photon energy value [66].

The absorption coefficient spectrum denotes how Al thickness can control the band-to-band absorption and direct the electronic transition correlated to band tails.
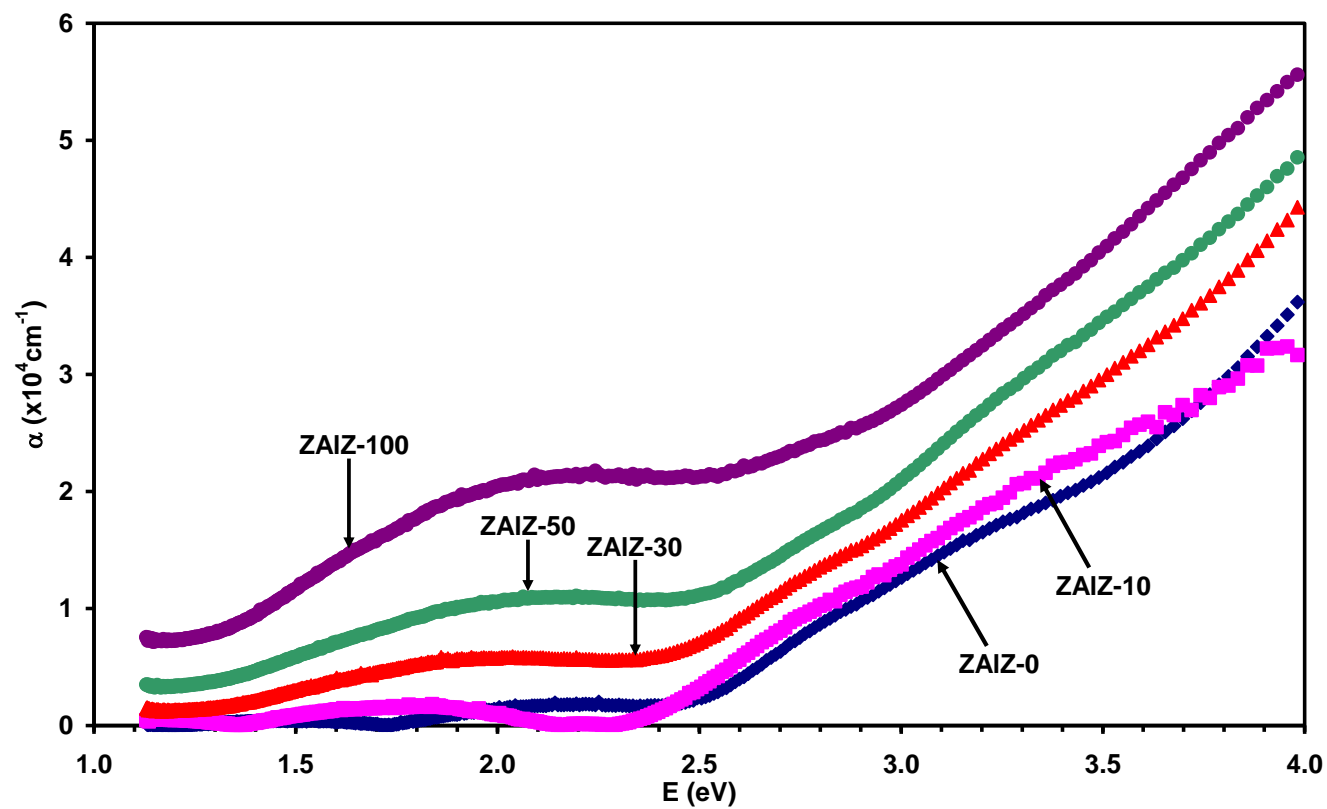
Fig. 4.15. The absorption coefficient (α) versus photon energy (E) for the Al sandwiched ZnSe thin films.

As we have previously done, the E_g determination requires $(\alpha E)^{1/p}$ plotting against the photon energy E in the high absorption region for the pure and Al sandwiched ZnSe thin films, according to Tauc equation.

$(\alpha E)^{1/2}$, $(\alpha E)^2$, $(\alpha E)^{1/3}$, and $(\alpha E)^{2/3}$ were plotted in Fig. 4.16 and Fig. 4.17. The plot $(\alpha E)^{2/3}$ versus photon energy (E) for 30, 50, 100 nm Al sandwiched ZnSe films was selected since it has the widest range of linear data. The plot $(\alpha E)^{2/3}$ versus photon energy (E) signify a direct forbidden transition. The direct forbidden transition was perceived in several semiconductor compounds like GaSe [63]. However, The plot $(\alpha E)^2$ versus photon energy (E) for pure and 10 nm Al sandwiched samples was selected, which indicates a direct allowed transitions.

The optical characteristics of the as grown ZnSe thin film were reported in literature, $ln(\alpha E)$ was plotted as a function of $ln(E\text{-}E_g)$, the slope of the linear plot was determined to be 0.45, and this value is very close to 0.5 that designates the direct electronic transition [67]. This authorizes our $(\alpha E)^2$ sketching versus photon energy for pure and 10 nm Al sandwiched ZnSe samples.

The direct allowed and direct forbidden transitions were investigated earlier in the theoretical part of this thesis. The direct forbidden transition was reported to need lower transition energy compared to the direct allowed; this explains the direct forbidden transition in many solids when exposed to light. The forbidden transition and the related interband conductivity were previously studied. The obtained results reveals that the direct forbidden transition conductivity is approximately hundred times lower than the conductivity of the direct allowed. This was explained by the tunneling of the charge carriers [68]. So, one may assign the transformation from the direct allowed transition to direct forbidden for the 30, 50, and 100 nm Al sandwiched ZnSe thin films to the initiated donor levels near the conduction band.
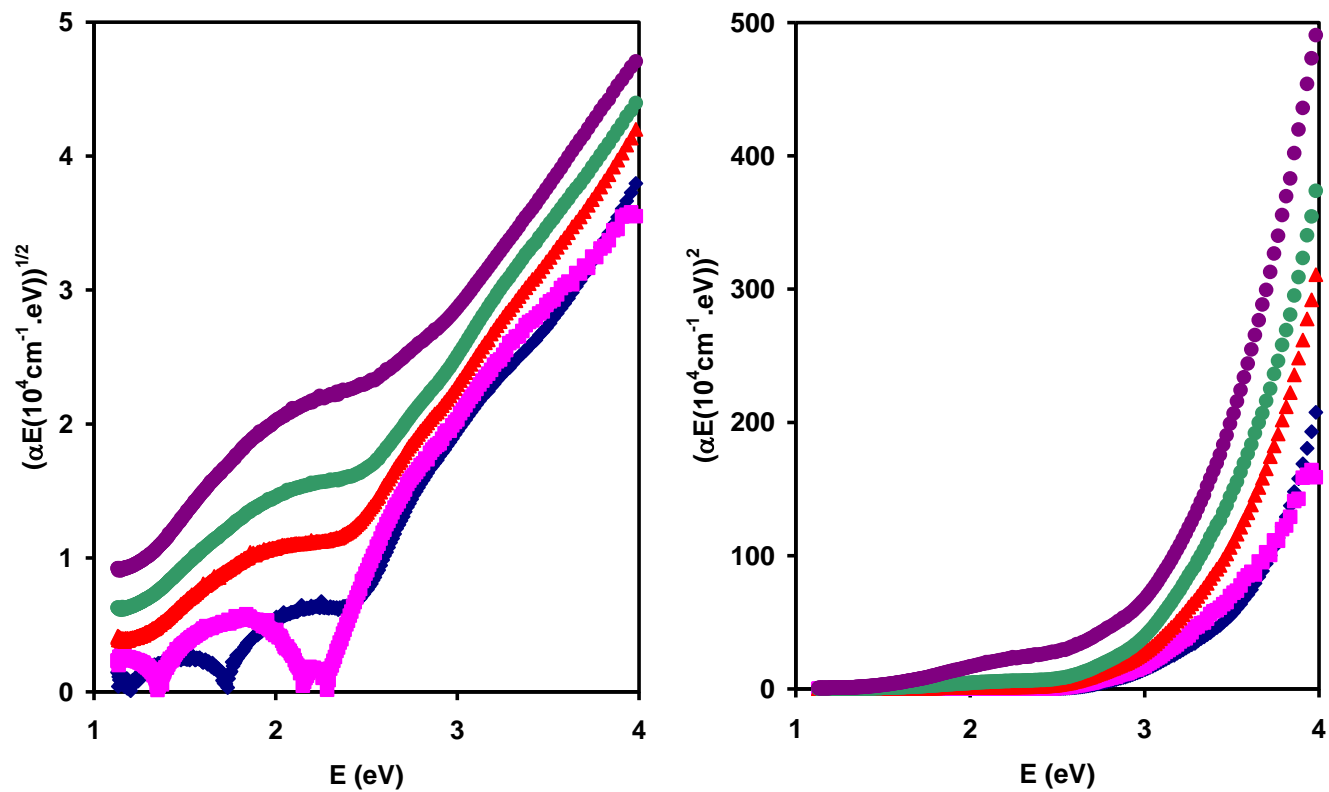
Fig. 4.16. $(\alpha E)^{1/p}$ versus photon energy (E) for (a) indirect allowed, and (b) direct allowed electronic transition in the Al sandwiched ZnSe thin films.
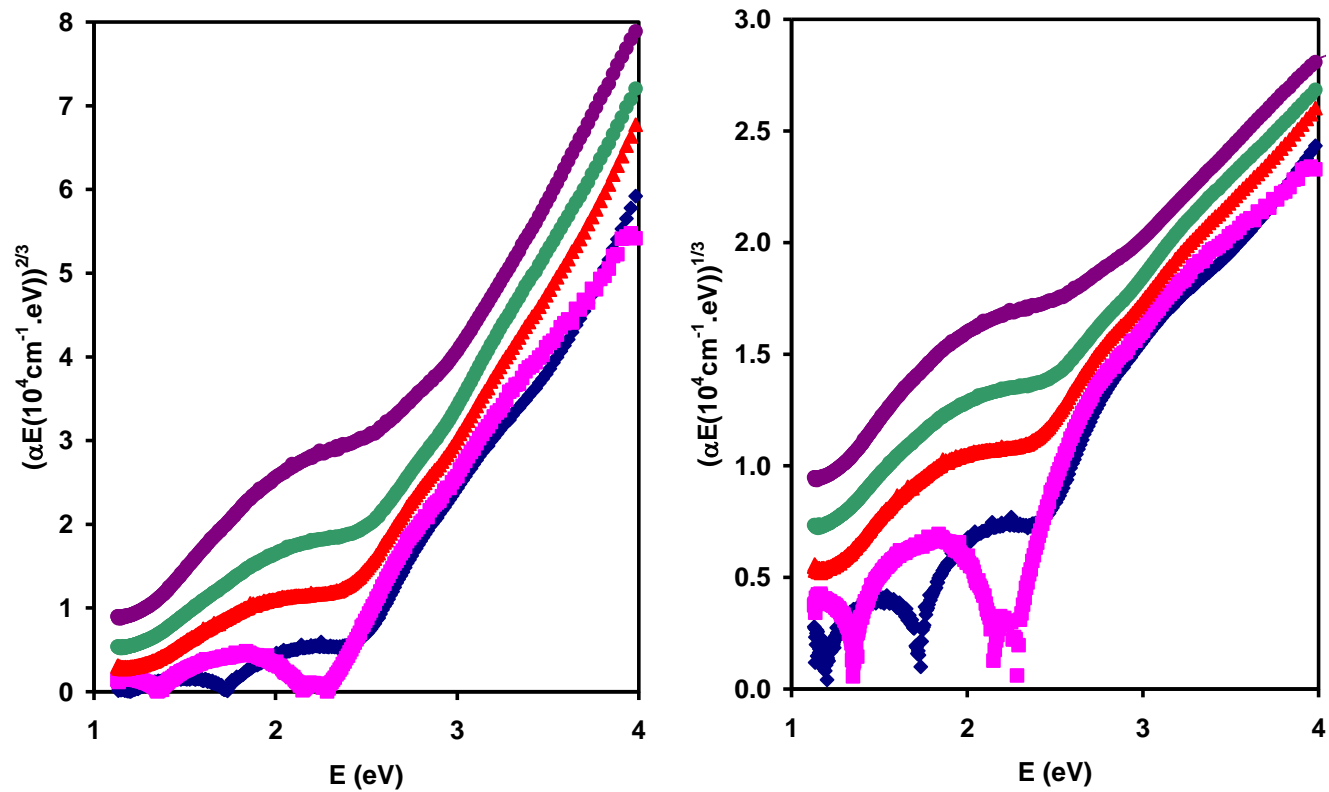
Fig. 4.17. $(\alpha E)^{1/p}$ versus photon energy (E) for (a) direct forbidden, and (b) indirect forbidden electronic transition in the Al sandwiched ZnSe thin films.

The lines indicated in Fig. 4.18 were extrapolated with the photon energy axis, and the obtained intercepts stand for E_g, the attained energy gap values are listed in Table 4.4. One can notice the decrease in the band gap values from 2.67, 2.58, 2.23, 2.10 to 2.05 eV upon 10, 30, 50, and 100 nm Al insertion, respectively.

A similar performance was reported and identified in the as grown Au sandwiched InSe thin films. The values of the energy gap were found to drop from 2.27 eV to 2.11 eV and 1.64 eV due to 20 and 100 nm thick Au insertions, respectively. The decrease in the band gap was credited to back-to-back Shotcky diodes formation with opposite electric fields on the two sides of the Au layer, that forces a band bending. Increasing the Au thickness brings on more free carriers in the two metal surfaces, which correlate stronger electric fields and rough band bending due to Coulomb's attraction. Another issue was taken into account for having a hand on the gap shrinkage is the image charge potential lowering. In optoelectronic, it is known that the potential lowering is proportional to the square root of the electric field and effective dielectric constant. Also, the diffusion of Au atoms in the upper and lower InSe layers may take place, causes a type of impurity and host material interaction termed as a deformation potential. The raised doping, enlarge the number of the Au interstitial atoms which perturb the band edge by inducing tails with a considerable density. Band tails conduct a reduction in the band gap [69]. These justifications seem logical to figure out the decrease in the band gaps of the sandwiched ZnSe films when Al concentration increases.

The pure ZnSe thin film energy gap is (2.67 eV), which is compatible with the reported energy gap of the thermally evaporated ZnSe thin films (2.60-2.64 eV) [70] as well as with the reported bulk ZnSe energy gap (2.70 eV) [71].
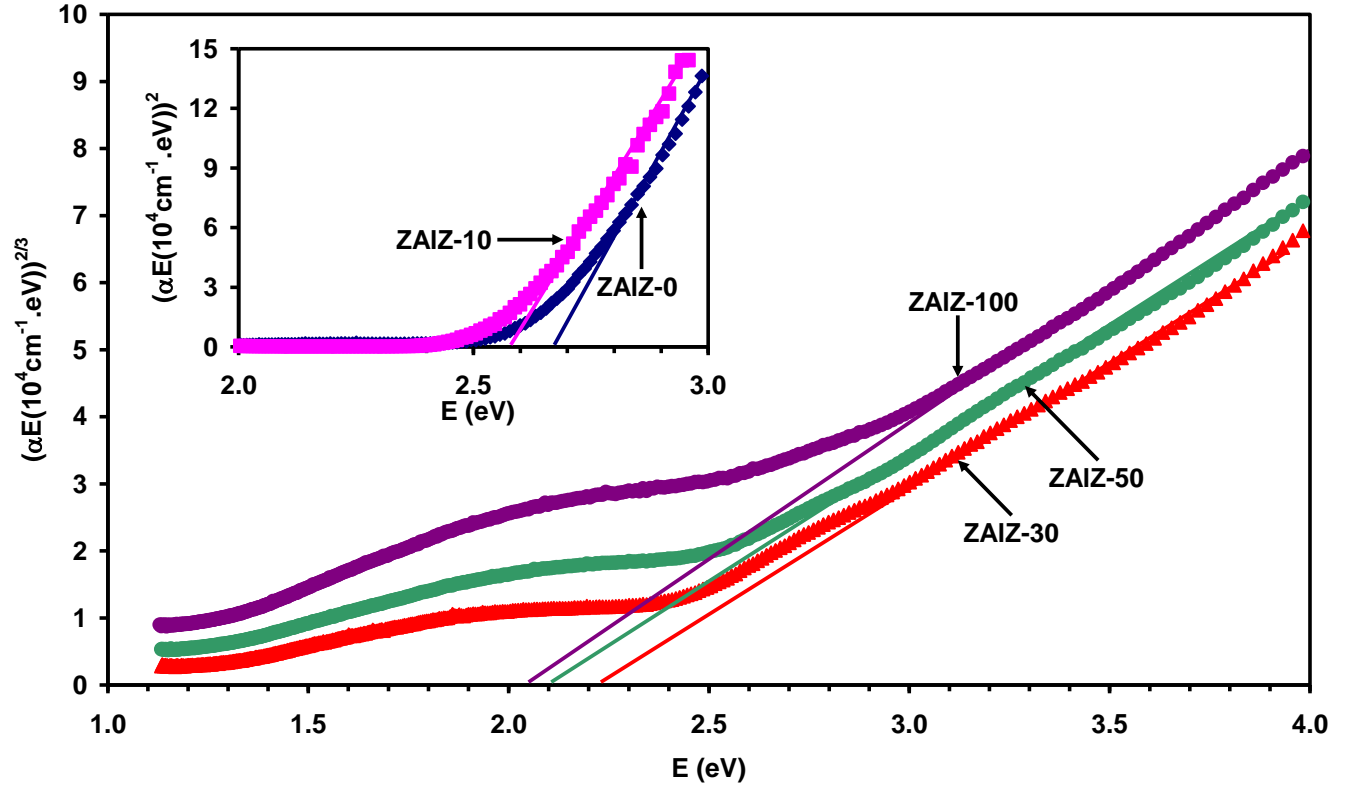
Fig. 4.18. $(\alpha E)^{2/3}$ and $(\alpha E)^2$ versus photon energy (E) for the 30,50,100 nm and 0,10 nm Al sandwiched ZnSe thin films, respectively.

As we did before, the band tails width (E_e) can be determined from the slopes of the straight lines appear in Fig. 4.19. The band tails width (E_e) was computed to have the values 0.136, 0.499, and 0.561 eV for the 30, 50, and 100 nm Al sandwiched ZnSe thin films, respectively (see table 4.4). The energy gap tuning can be referred to the increase in the width of the band tail [72]. It is evident that Al sandwiching can control the transition width of the band tails; this is believed to be due to the perturbation of the band edge, which stems from the overlapping of the close energy levels. Overlapping of the close states narrows the energy gap, increases the absorption ability, and increases the band tails width [73].

4.2.3 Comparison between Optical Properties of Al Sandwiched and Al Doped ZnSe Thin Films

An optical comparative study can be performed between Al nanosandwiching and Al doping. The transmittance, reflectance, and absorption coefficient spectra of the 100 nm Al sandwiched and Al doped ZnSe thin films are indicated in Fig. 4.20. The Al doped film shows generally a higher transmittance, lower reflectance, and lower absorbance values. These results can be assigned to the deposited Al plate, which prevent light from propagation. However, the randomly distributed Al molecules in the Al doped ZnSe film explains the reason for the lower light reflectivity.
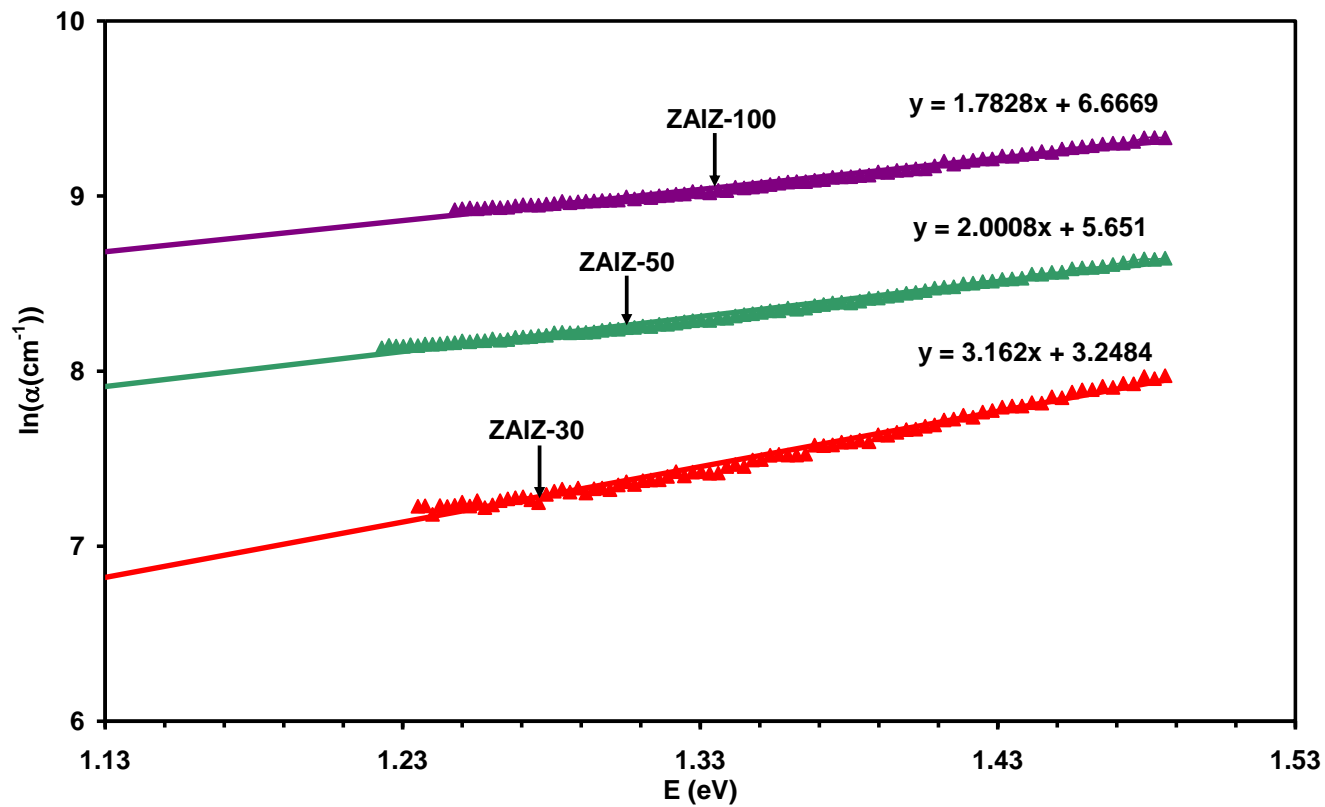
Fig. 4.19. (*ln*(α)) versus photon energy (*E*) for the 30, 50, and 100 nm Al sandwiched ZnSe thin films.

Table 4.4

Energy band gaps and band tails width of Al sandwiched ZnSe thin films.

Sample	E_g (eV)	E_e (eV)
ZnSe / Al(0 nm)/ ZnSe	2.67	~
ZnSe/ Al(10 nm)/ZnSe	2.58	~
ZnSe/ Al(30 nm)/ZnSe	2.23	0.136
ZnSe/ Al(50 nm)/ZnSe	2.10	0.499
ZnSe/Al(100nm)/ZnSe	2.05	0.561
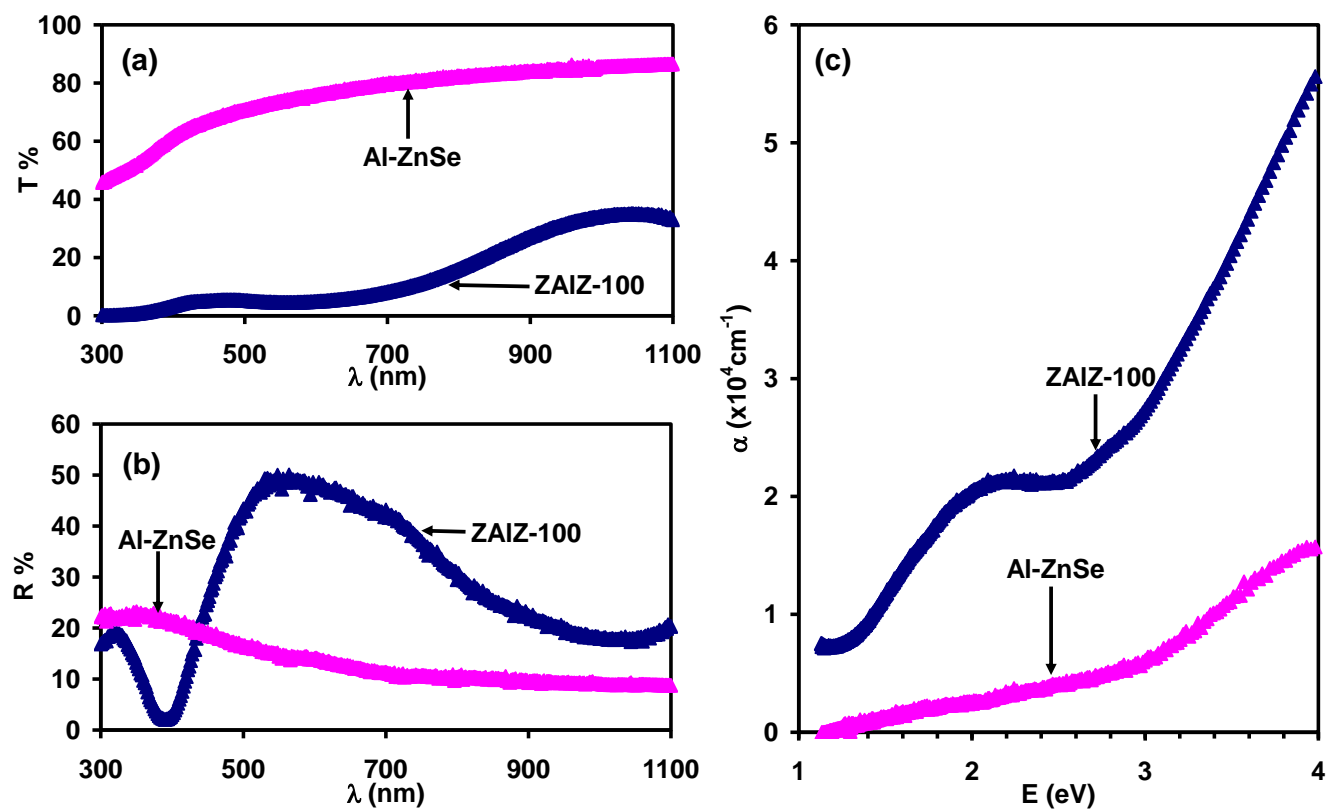
Fig. 4.20. (a) Transmission, (b) reflection, and (c) absorption coefficient spectra for 100 nm Al sandwiched and Al doped ZnSe thin films.

4.3 Dielectric Analysis

4.3.1 Real Dielectric Spectra of as Deposited and Annealed ZnSe and Al Doped ZnSe Thin Films

The introduced optical reflectance spectral data is used to deduce the effective dielectric constant (ε_{eff}). The reflectance (R) and the effective dielectric constant (ε_{eff}) are directly related through equation (2.78) stated in the theoretical part.

$$R = \frac{(\sqrt{\varepsilon_{eff}} - 1)^2 + (\frac{\alpha\lambda}{4\pi})^2}{(\sqrt{\varepsilon_{eff}} + 1)^2 + (\frac{\alpha\lambda}{4\pi})^2} \tag{4.3}$$

The real part of the effective dielectric constant (ε_{eff}) is identified as a real dielectric constant (ε_r), which illustrates electric dipoles generation and the sequential change in the material polarization by the presence of electromagnetic waves. However, the imaginary part of the effective dielectric constant, symbolized by (ε_{im}), regards to wave attenuation inside the deposited films. The real and imaginary dielectric constants were evaluated using equations (2.63) and (2.64).

$$\varepsilon_r = \varepsilon_{eff} - (\frac{\alpha\lambda}{4\pi})^2 \tag{4.4}$$

$$\varepsilon_{im} = \sqrt{\varepsilon_{eff}}(\frac{\alpha\lambda}{2\pi}) \tag{4.5}$$

The effect of annealing on the dielectric constant spectra can be figured out by surveying Fig. 4.21 (a). This figure deals with the dielectric spectra of the thermally treated ZnSe at 200 °C and that of the as grown ZnSe thin films. Principally, the 200 °C annealing considerably lowers the values of the ZnSe dielectric constant values whilst it doesn't affect the dielectric spectra format of the as grown ZnSe sample.

The maximum dielectric constant for the as grown ZnSe film is 4.72 at a frequency of 568 THz (2.35 eV) whereas the annealed film owns a dielectric maximum of 3.87 at 620 THz (2.57 eV). An evident shift in the visible light frequency in ZnSe samples dielectric spectra is achieved by heat treatment; this indicates that annealing can derive more light responsivity in the visible light region.

Dielectric peaks entity at 2.35 eV and 2.57 eV for the as grown and annealed ZnSe films can be ascribed to the reported direct energy gap in the ZnSe thin films. The promotion in the heat treated ZnSe sample grain size could be probably the reason for the dielectric spectrum attenuation. Venkatachalam et al have previously declared a decrease in the dielectric values for the annealed ZnSe thin films [74].

Furthermore, Al doped ZnSe thin film was annealed at 200 ^{o}C. The dielectric spectra of the annealed film shows a systematic decrease relative to the dielectric spectra values of the as grown Al doped ZnSe film, especially when the light frequency exceeds 600 THz as clarified in Fig. 4.21 (b).

In details, the dielectric constant peaks of the Al doped ZnSe film decrease from 8.17 to 3.45 and shift from 857 THz to 833 THz upon 200 ^{o}C annealing, with no explicit variation in the general dielectric spectra performance. So, the dielectric maxima appear as 3.55 eV and 3.45 eV for the as grown and 200 ^{o}C annealed Al doped ZnSe films, respectively. These energy values can be referred to the film's light absorption and carrier's direct transitions. A spectroscopic ellipsometry investigation of the grown $Zn_{1-x}Cu_xSe$ thin films presents an analogous dielectric constant lowering by annealing [75].

The effect of Al doping on the real dielectric constant spectra can be visualized with the help of Fig. 4.21 (c). Ordinarily, Al doping causes first a noticeable increase in the dielectric spectra compared to the pure ZnSe film. In addition, Al doping causes a dielectric spectra reshaping.

For the ZnSe film, the maximum dielectric constant value is 4.72 at a light frequency of 568 THz (2.35 eV). On the other hand, the Al doped ZnSe film has a dielectric peak of 8.17 sets at a frequency of 857 THz (3.52 eV). The increase in the spectral dielectric constant via Al doping could be referred to the formerly characterized transformation from the ZnSe cubic structure to the amorphous Al doped ZnSe. Also, Al doping brings on more free carriers as a result of the delocalized impurity levels presence near valence band; this motivates the increase in the dielectric maxima from 4.72 to 8.17.

Fig. 4.21 (d) presents the dielectric spectra behavior of the 200 ºC annealed ZnSe and Al doped ZnSe thin films. For the as grown films it appears that Al doping stimulates an increase in the values of the real dielectric constant. But when annealing comes into action, thermal treatment overcomes the effect of metal doping. Such that, the maximum dielectric constant value is assigned to the annealed ZnSe film with a value of 3.87 at 620 THz while the annealed Al doped ZnSe has a maximum of 3.45 at 833 THz.
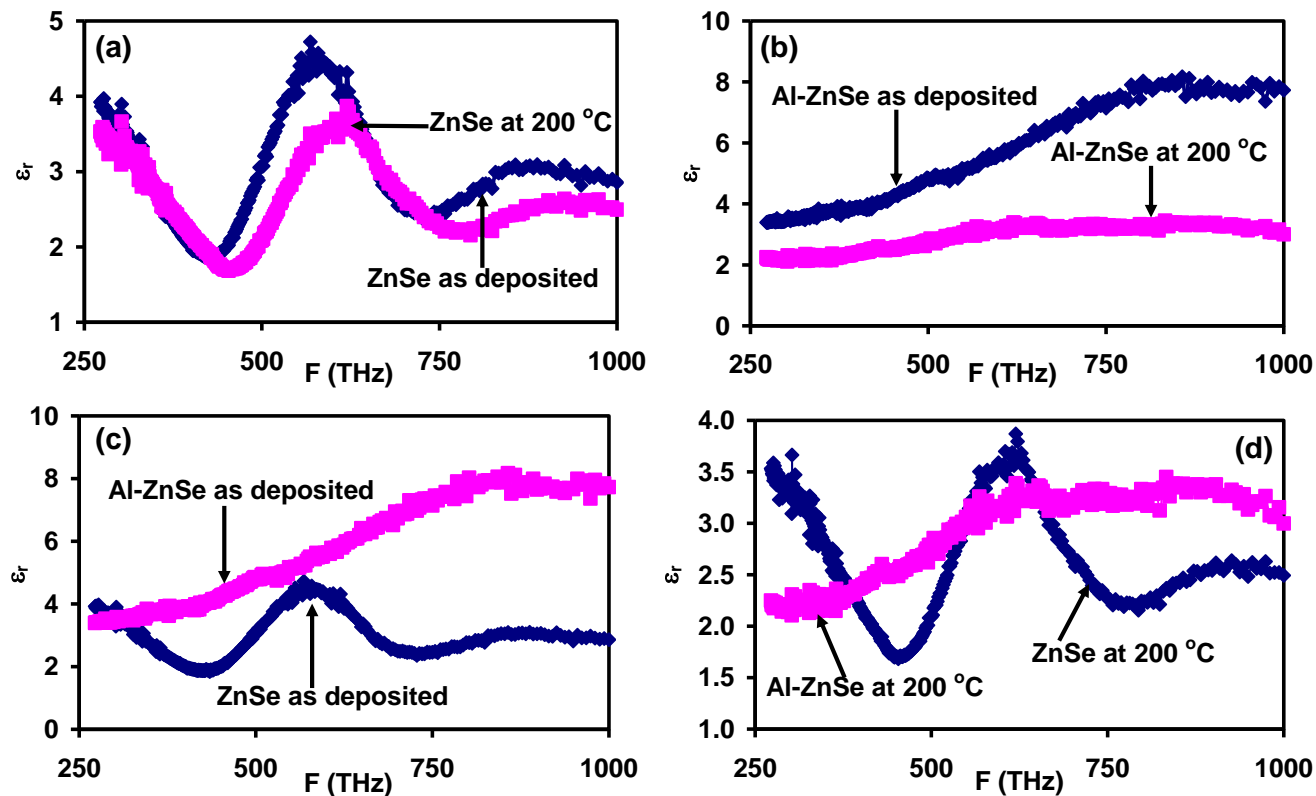
Fig. 4.21. The real dielectric spectra for the (a) as grown & annealed ZnSe films, (b) as grown & annealed Al doped ZnSe films, (c) as grown ZnSe & Al doped ZnSe films, and (d) annealed ZnSe & Al doped ZnSe films.

4.3.2 Real Dielectric Spectra of the Al Sandwiched ZnSe Thin Films

The real dielectric constant spectra for the (0, 10, 30, 50, and 100) nm Al sandwiched ZnSe samples are displayed in Fig. 4.22. This figure reveals an apparent growing in the real dielectric constant values with the incident light frequency till come to a maximum then the dielectric constant values starts to decrease. The ZnSe/Al(0 nm)/ZnSe reveals a maximum real dielectric constant of 10.56 at a light frequency of 492 THz (2.04 eV). In addition, the ZnSe/Al(10 nm)/ZnSe shows a maximum real dielectric constant of 10.82 at a light frequency of 429 THz (1.78 eV). The ZnSe/Al(30 nm)/ZnSe shows a maximum real dielectric constant of 9.02 at a light frequency of 426 THz (1.77 eV). While, the ZnSe/Al(50 nm)/ZnSe has a maximum value of 10.24 at a light frequency of 478 THz (1.98 eV), and the ZnSe/Al(100 nm)/ZnSe exhibits a jump in the maximum real dielectric constant value when a 100 nm Al layer is inserted to be 34.05 at 532 THz (2.20 eV).

The enhancement in the real dielectric constant values when the thickness of the Al layer is raised above 30 nm is favored since it suggests the Al layer thickness effect on the spectrum of the real dielectric constant. The maxima introduced in Fig. 4.22 inform a shift in the real dielectric spectra of the ZnSe/Al(30 nm)/ZnSe, ZnSe/Al(50 nm)/ZnSe, and ZnSe/Al(100 nm)/ZnSe toward higher frequencies relative to ZnSe/Al(10 nm)/ZnSe dielectric spectra, which articulate the increase in the ZnSe/Al/ZnSe film's visible light sensitivity with metal sandwiching.

It is worth to be concerned about the increase in the energy values of the maximum dielectric spectra from 1.77 eV, 1.98 eV to 2.20 eV as illustrated in Fig. 4.22 for the ZnSe/Al(30 nm)/ZnSe, ZnSe/Al(50 nm)/ZnSe, and ZnSe/Al(100 nm)/ZnSe, respectively. This increase may be ascribed by the selected direct absorption transitions in the Al sandwiched ZnSe films between the direct conduction and valence valleys through directly associated states.
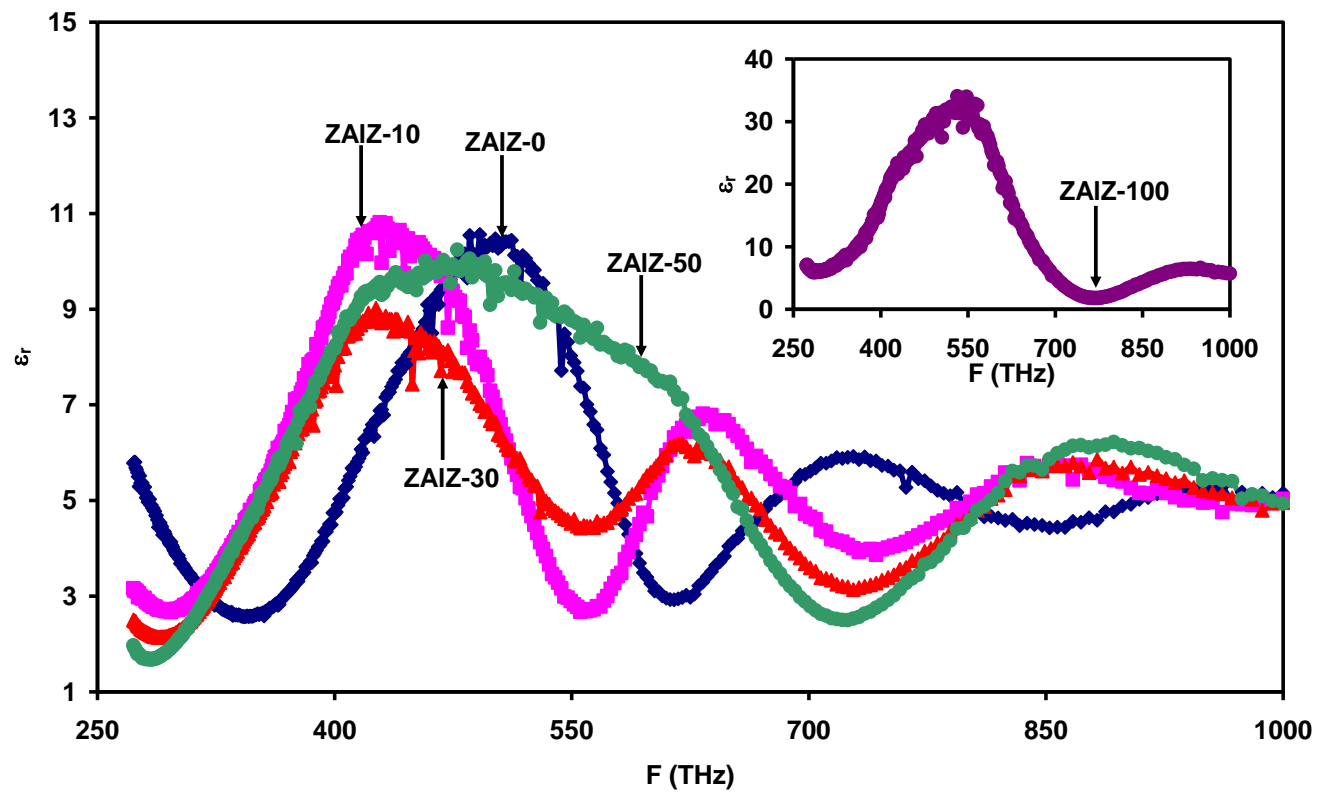
Fig. 4.22. The real dielectric spectra for the (0, 10, 30, 50, and 100) nm Al sandwiched ZnSe thin films.

4.3.3 Plasmon-Electron Interaction in the as Deposited and Annealed ZnSe and Al Doped ZnSe Thin Films

The imaginary dielectric constant ε_{im} of the grown films can be plotted as a function of optical frequency. The optical conductance of the prepared samples is directly related to the imaginary dielectric constant ε_{im} through the equation ($\sigma(\omega)=\omega\ \varepsilon_{im}$). To inspect some variables which can be transferred from the effect of the incident electromagnetic waves on plasmon-electron interaction, the imaginary part of the dielectric constant ε_{im} is modeled according to Drude-Lorentz, which was explained in the theoretical part of this thesis. One can come by the dielectric parameters of the grown films by employing the following relation [69],

$$\varepsilon_{im} = \sum_{i=1}^{k} \frac{\omega_{pei}^2 \omega}{\tau_i((\omega_{ei}^2 - \omega^2)^2 + \omega^2 \tau_i^{-2})} \tag{4.6}$$

Herein, $\omega_{pe} = (4\pi ne\ /m^*)^{1/2}$ is the free charge carrier bounded plasma frequency, where n is the free charge carrier density and m^* is the effective mass of the free carriers in the grown samples, ω is the frequency of the incident electromagnetic waves, τ is the free charge carrier scattering time, and ω_e is the reduced resonant frequency.

The importance of imaginary dielectric spectra modeling stems from drift mobility evaluation where ($\mu=e\tau/m^*$). The free electron oscillations relative to the positively charged ions can be exemplified by the imaginary dielectric spectra oscillations. The free electron symmetric oscillations are motivated by the electromagnetic waves. Free carrier oscillations are damped by a restoring force originates from the bounding positive ions, and the restoring force is inversely proportional to the free carriers scattering time such that ($F\alpha\tau^{-1}$).

Returning back to the previous equation, the imaginary dielectric spectra will have a maximum when the first part of the denominator goes to zero, this means that the frequency of the incident electromagnetic wave is equal to the free charge carriers frequency.

By setting off the previously reported Al and ZnSe effective masses (m^*_{Al}=0.97m_o [76], m^*_{ZnSe}=0.134m_o [77]), the reduced mass of the as grown and annealed ZnSe thin films is 0.134m_o. As well as, the reduced mass of the as grown and annealed Al doped ZnSe films can be assumed to be 0.134m_o since the Al percent in the doped films is small. These reduced masses are required to set the charge carrier bounded plasma frequency ω_{pe}.

Fig. 4.23 illustrates the experimentally achieved and the modeled imaginary dielectric spectra of the ZnSe samples, which shows a considerable coincidence between the experimental graph (colored line) and modeled spectra (black line). On the other hand, the experimental and the modeled imaginary dielectric spectra of the Al doped ZnSe films are presented in Fig. 4.24 by the colored and black lines, respectively.

Drude-Lorentz model enables us to find out the dielectric parameters by computation. The obtained parameters were listed in Tables 4.5 & 4.6 for the as grown and annealed ZnSe and Al doped ZnSe samples, respectively.

The fitting parameters related to the free carrier's coupled oscillations denote the optoelectronic features of the as grown and annealed films. Presently, the samples obtained parameters reveal a refinement in the films optical conduction when thermally treated. Particularly, the free carrier's density n is increased from $130{\times}10^{17}$cm^{-3} to $280{\times}10^{17}$cm^{-3}. However, the drift mobility μ of the carriers is decreased from 30.2 cm^2/Vs to 19.7 cm^2/Vs. Also, an increase in the plasmon frequency

from 5.9 GHz to 8.6 GHz is observed for the as grown and annealed ZnSe samples, respectively. It was concluded that 200 °C annealing promotes the optoelectronic properties of the ZnSe thin film by enhancing the free carrier density n. However, 200 °C annealing reduces the mobility because of the increased interaction between the electrons and the vibrating lattice atoms and between the electrons themselves. Lattice vibration is expected to increase as the temperature increases; this implies that the probability of the scattering event also increases, thus the mobility decreases. The increased scattering events are evident from the decrease in the scattering time (from 2.3 fs to 1.5 fs). This happened despite the fact that annealing enhances grain size, which leads to increase carrier mobility. But it seems scattering is more dominant in reducing the mobility.

The free carrier density of the as deposited ZnSe (130×10^{17}cm^{-3}) reveals that this film has n-type conductivity. Refer to EDAX results, there was observed Se vacancies in the as grown ZnSe thin film. These vacancies are responsible for the n-type conductivity.

The tabulated parameters of the as deposited and annealed Al doped ZnSe samples shows an increase in the free carrier scattering time from 1 fs to 10 fs. The free carrier density n has such behavior, which is raised from 160 x10^{17}cm^{-3} to 440 x10^{17}cm^{-3}. A conducted increase in the carrier mobility from 13.1 cm^2/Vs to 131.1 cm^2/Vs is also observed in the as deposited and annealed Al doped ZnSe films, respectively. The increase in the scattering time is related to the mobility enhancement. The increase in the drift mobility of the Al doped ZnSe thin film upon annealing implies a decrease in the carriers damping coefficient. This mobility increase may be due to the increase in the grain size of the amorphous structure upon annealing, which leads to an increase in the scattering time (decrease in scattering events). The alteration in the mobility of the doped sample upon 200 °C annealing may be also assigned to an ionized impurity scattering. If annealing is preformed on the Al doped ZnSe film,

the carrier's thermal velocity increases, thus the time the free carrier spent in the vicinity of the ionized impurity is decreased. The less time spent the smaller the scattering event and the greater the mobility.

Finally, one can conclude that annealing performed on Al doped ZnSe films excites a progression in the fitting parameters and sample properties. Comparing the as grown ZnSe and Al doped ZnSe films plasmon-electron parameters obtained by modeling, Al doping prompts a great increase in the free carrier's density from 130×10^{17} cm^{-3} to 160×10^{17} cm^{-3} for as deposited ZnSe and Al doped ZnSe thin films, respectively. The same increase was also observed in the annealed films, such that the free carrier density increases from 280×10^{17} cm^{-3} to 440×10^{17} cm^{-3} for the annealed ZnSe and Al doped ZnSe thin films, respectively.
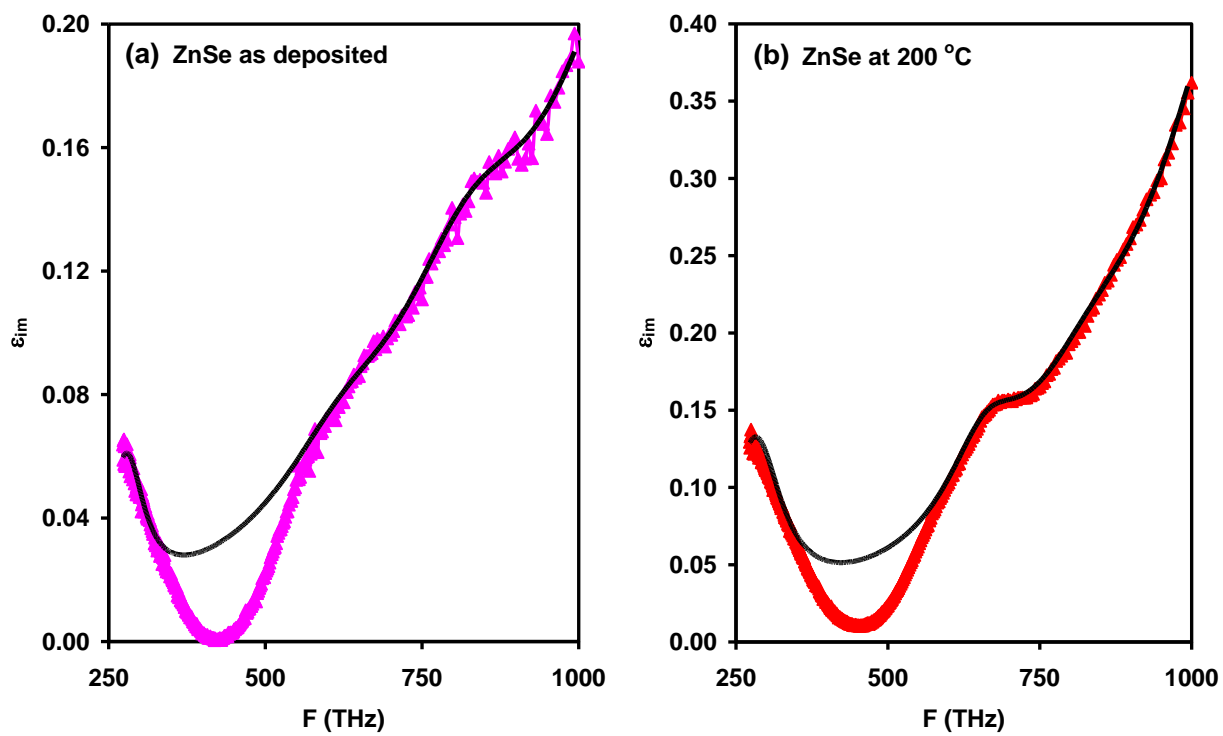
Fig. 4.23. The imaginary dielectric spectra for the (a) as grown, and (b) annealed ZnSe thin films.
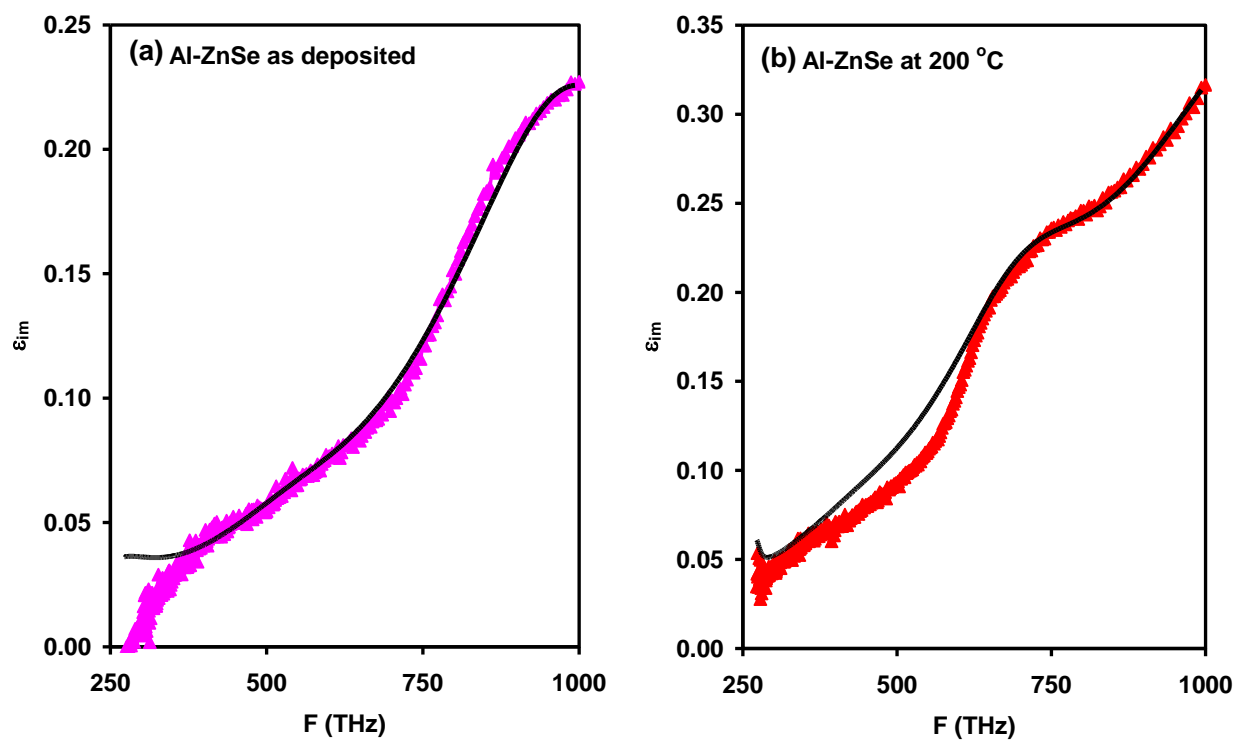
Fig. 4.24. The imaginary dielectric spectra for the (a) as grown, and (b) annealed Al doped ZnSe thin films.

Table 4.5

Plasmon-electron interactions in the as grown and annealed ZnSe films.

Parameter	ZnSe as grown				ZnSe annealed at 200 ºC			
τ_i (*fs*)	2.3	0.6	0.5	0.4	1.5	1.0	0.6	0.4
w_{ei} (x10^{15}Hz)	1.7	4.0	5.3	7.16	1.8	4.2	5.3	7.2
n (x10^{17} cm^{-3})	1.2	5.9	25.0	130.0	4.5	8.0	17.0	280.0
μ (cm^2/V s)	30.2	7.9	6.6	5.2	19.7	13.1	7.9	5.3
w_{pei} (GHz)	0.6	1.3	2.6	5.9	1.1	1.5	2.1	8.6

Table 4.6

Plasmon-electron interactions in the as grown and annealed Al doped ZnSe films.

Parameter	Al-ZnSe as grown				Al ZnSe annealed at 200 ºC			
τ_i (*fs*)	1.0	0.5	0.4	0.3	10.0	0.7	0.5	0.2
w_{ei} (x10^{15}Hz)	1.7	3.5	5.0	6.5	1.7	2.8	4.5	7.7
n (x10^{17} cm^{-3})	0.9	3.0	1.0	160.0	0.1	1.0	24.0	440.0
μ (cm^2/V s)	13.1	6.5	5.3	3.9	131.2	9.2	6.6	2.6
w_{pei} (GHz)	0.5	0.9	0.5	6.5	0.2	0.5	2.5	10.8

4.3.4 Plasmon-Electron Interaction in the Al sandwiched ZnSe Thin Films

Drude-Lorentz models the free carrier oscillations of the sandwiched films by fitting the imaginary dielectric spectra. The free electrons resonance at the interface between the two ZnSe layers is stimulated by the incidence of the electromagnetic waves. The effective mass of the three layers samples was computed as $(m^*_e=((m^*_{Al})^{-1} + 2(m^*_{ZnSe})^{-1})^{-1}=0.0627m_o$, which in turn is substituted into the constructed template to generate the relevant fitting parameters.

The optical parameters of the ZnSe/Al/ZnSe films are presented in Table 4.7 & 4.8, which designate the effect of Al nanosandwiching on the samples optical conduction. Fig. 4.25, 4.26, and 4.27 introduce the experimentally created (colored line) and the modeled (black line) ZnSe/Al/ZnSe imaginary dielectric spectra.

In general, an increase in the electron scattering time values were identified. This increase points out less damping upon Al sandwiching. An analogous promotion in the drift mobility of the sandwiched films was noticed when the Al content is increased. The free electron mobility increases from 140.2 cm^2/Vs to 280.4 cm^2/Vs for the ZnSe/Al(10 nm)/ZnSe and ZnSe/Al(100 nm)/ZnSe, respectively. The free electron density was found to be 92.5×10^{17} cm^{-3} when a 100 nm Al layer is deposited between the ZnSe layers. In addition, the tables data show that nanosandwiching shifts the charge carrier bounded plasma frequency toward higher values compared to the pure film. However, the electron reduced frequency values don't show a distinct alteration.

Our previous consideration to mobility proves the metal sandwiching role in optical conduction improvement. Furthermore, by increasing the number of oscillators, the free electron density, reduced and plasmon frequencies are generally increased. But, the free electron scattering time and the drift

mobility were damped with oscillators. This can be assigned to electron-hole recombination in the ZnSe/Al/ZnSe films.

Compare the recently investigated ZnSe/Al(100 nm)/ZnSe with the Al doped ZnSe film, the 100 nm Al nanosandwiching reveals a preferable optical conduction parameters. Ordinarily, the free electrons scattering time raised from 1 *fs* to 10 *fs*, the scattering time associated mobility was shifted from 13.1 cm^2/Vs to 280.4 cm^2/Vs. Also, 100 nm Al nanosandwiching increases the charge carrier bounded plasma frequency and decreases the electrons reduced frequency. The increase in the ZnSe/Al(100 nm)/ZnSe sample dielectric parameters over the doped sample might be due to the isolated Al plate inserted between the two semiconductor layers, which facilitate the large mobility.
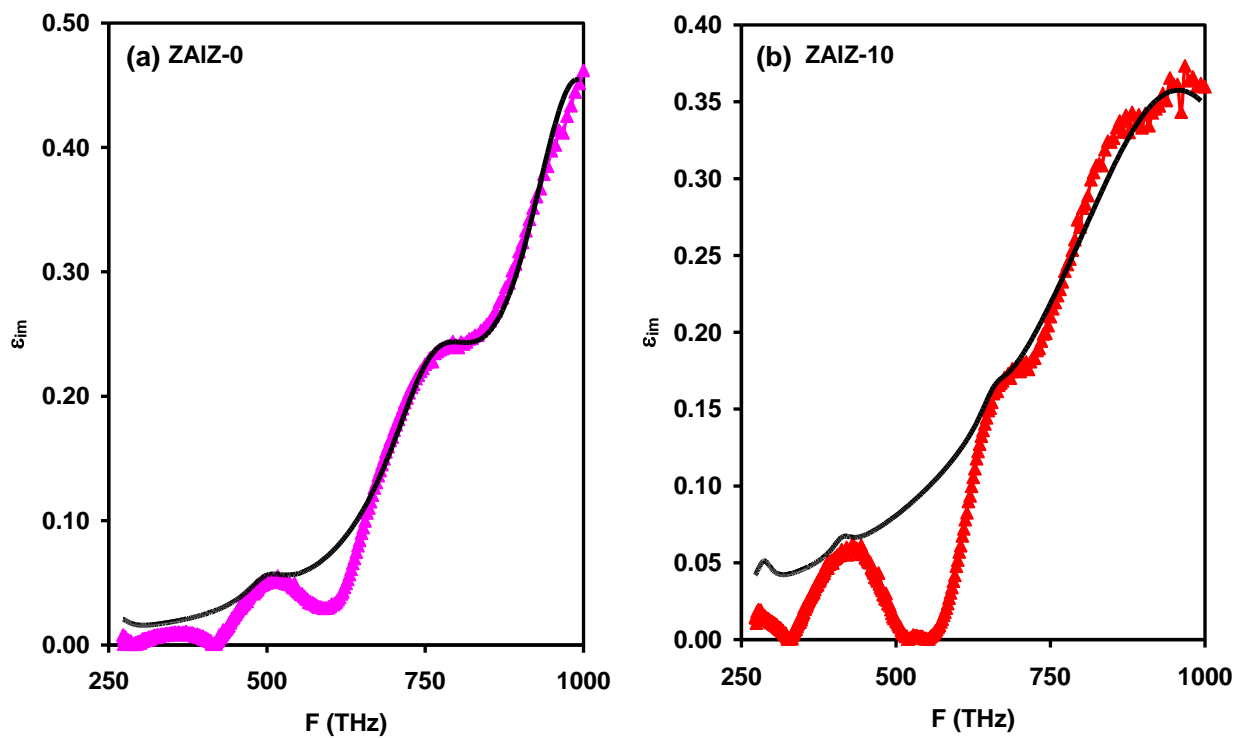
Fig. 4.25. The imaginary dielectric spectra for the (a) ZnSe/Al(0 nm)/ZnSe, and (b) ZnSe/Al(10 nm)/ZnSe thin films.
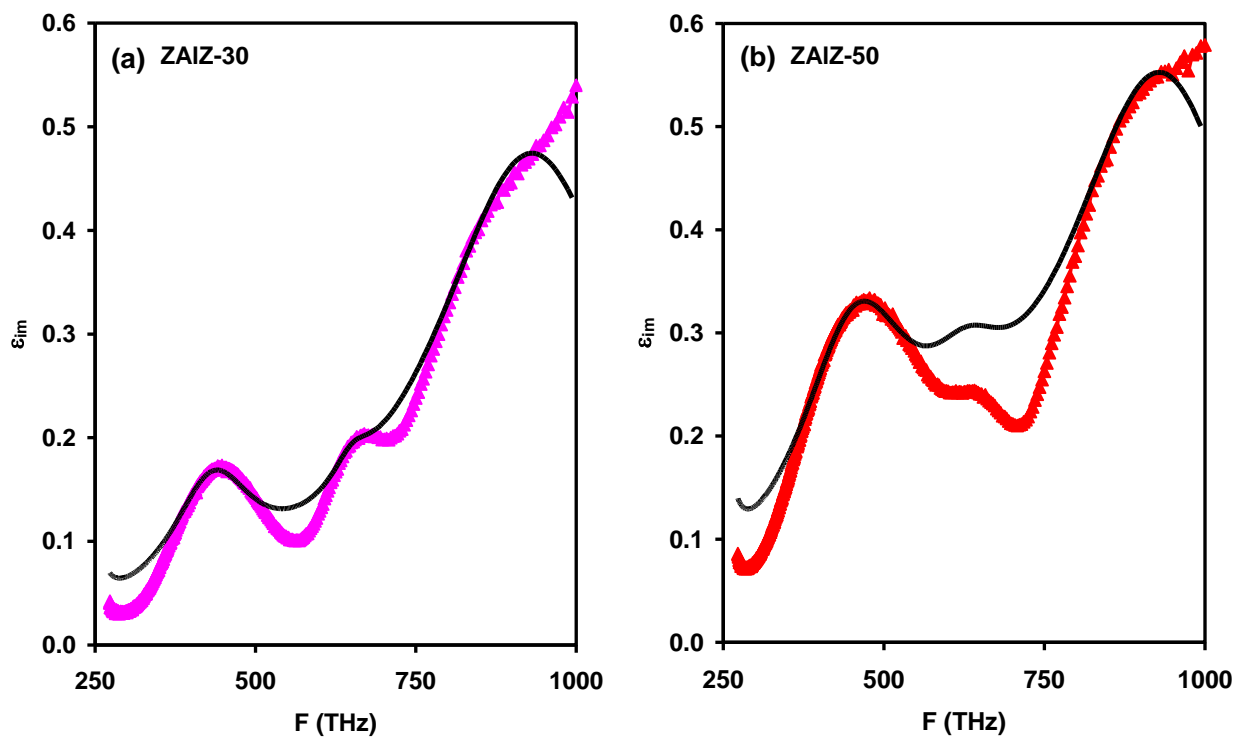
Fig. 4.26. The imaginary dielectric spectra for the (a) ZnSe/Al(30 nm)/ZnSe, and (b) ZnSe/Al(50 nm)/ZnSe thin films.
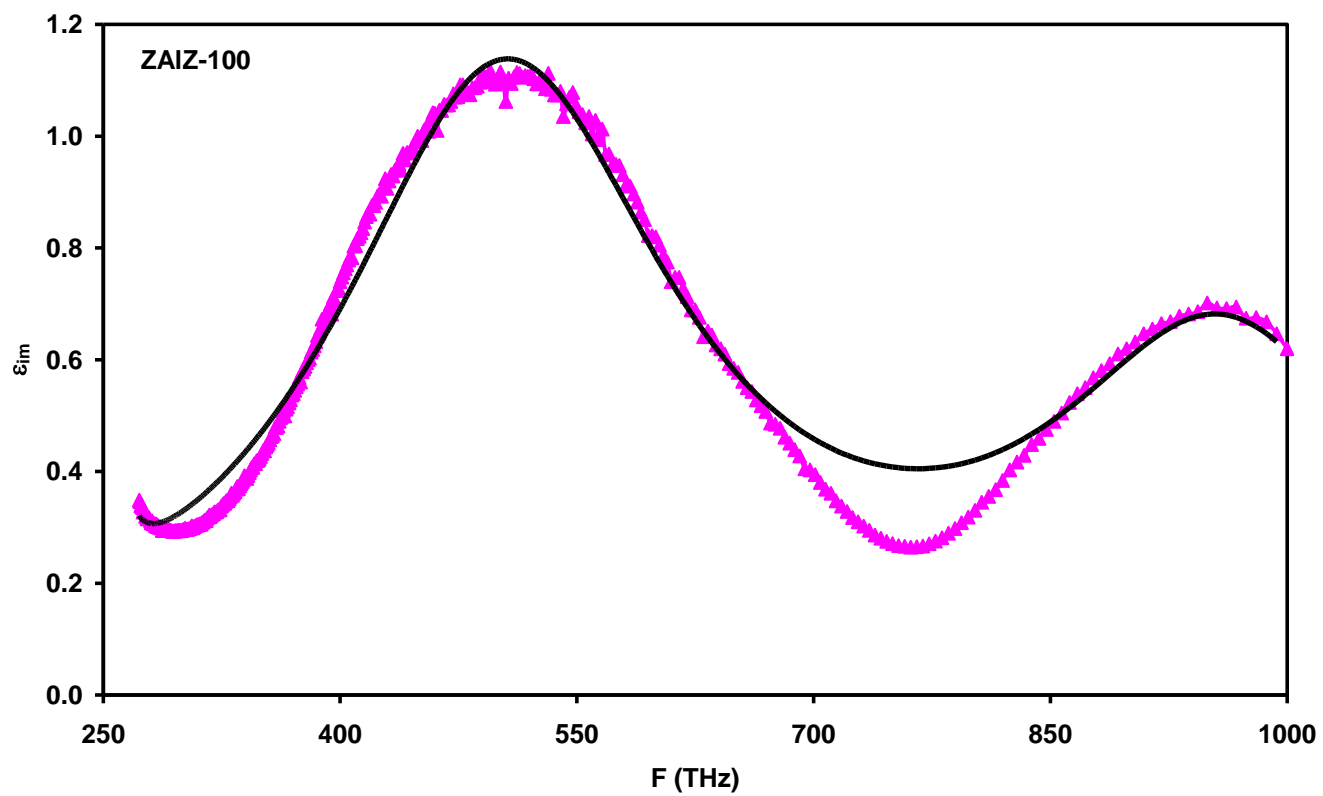
Fig. 4.27. The imaginary dielectric spectra for the ZnSe/Al(100 nm)/ZnSe thin film.

Table 4.7

Plasmon-electron interactions in the ZnSe/Al(0 nm)/ZnSe and ZnSe/Al(10 nm)/ZnSe films.

Parameter	ZnSe/Al(0nm)/ZnSe				ZnSe/Al(10nm)/ZnSe			
τ_i (*fs*)	5.0	2.0	0.8	0.7	5.0	4.0	3.0	0.3
w_{ei} ($\times 10^{15}$Hz)	1.7	3.1	4.9	6.3	1.8	2.6	4.1	6.3
n ($\times 10^{17}$ cm^{-3})	0.1	1.0	31.0	130.0	0.1	0.1	0.3	115
μ (cm^2/V s)	65.6	26.2	10.5	9.2	140.2	112.2	84.1	8.4
w_{pei} (GHz)	0.2	0.5	2.9	5.8	0.2	0.2	0.4	8.1

Table 4.8

Plasmon-electron interactions in the as grown ZnSe/Al (30 nm) /ZnSe, ZnSe/Al (50 nm) /ZnSe, and ZnSe/Al(100 nm)/ZnSe thin films.

Parameter	ZnSe/Al(30nm)/ZnSe				ZnSe/Al(50nm)/ZnSe				ZnSe/Al(100nm)/ZnSe			
τ_i (*fs*)	10.0	1.0	2.0	0.4	10.0	0.7	1.0	0.4	10.0	0.6	0.5	0.6
w_{ei} ($\times 10^{15}$Hz)	1.5	2.8	4.1	6.0	1.5	3.0	4.0	6.0	1.6	3.3	4.0	6.1
n ($\times 10^{17}$ cm^{-3})	1.0	4.8	1.0	110.0	2.0	16.0	5.0	125.0	1.0	92.5	0.31	96.0
μ (cm^2/V s)	280	28.0	56.1	11.2	280.4	19.6	28.0	11.2	280.4	16.8	14.0	16.8
w_{pei} (GHz)	0.8	1.6	0.8	7.9	1.1	3.0	1.7	8.4	0.8	7.2	0.4	7.4

Chapter Five

Conclusions

Al effect on the ZnSe structural properties was investigated minutely. The comparison between Al doping and nanosandwiching indicates sandwiching superiority over Al incorporation for its role in maintaining the ZnSe Zinc blende structure, improving grain size and lowering the ZnSe film strain, stacking fault, and dislocation density.

ZnSe is known for its high sensitivity to electromagnetic waves, and to the related applicability in optoelectronic devices. However, this promising material suffers from the high light transparency (low absorption) as well as the high electrical resistivity. Hence, Al doping and nanosandwiching were performed to improve the grown ZnSe samples absorbance and to attenuate the samples resitivities by increasing the free electron density via Al introduction. Al presence ensures higher absorbencies by exploiting the metals high reflectivity.

The effect of 200 ºC annealing on the grown samples optical properties was examined as well. Moreover, Al doping and Al sandwiching effect on the optical parameters such as transmittance, reflectance, absorbance, energy band gaps was carried out. Energy gap controlling via Al doping, guarantee the doped ZnSe usage in photodetectors and transistors manufacturing.

In addition, ZnSe dielectric properties were investigated upon Al doping, Al sandwiching and 200 ºC annealing. The conducted results show the alternations in the real and imaginary dielectric spectra, free carrier density, drift mobility, carrier scattering time, and plasmon frequency.

REFERANCES

[1] Wu, D., Shi, Z., Xu, T., Tian, Y., & Li, X. (2016). Gate-controllable photoresponse of nitrogen-doped p-type ZnSe nanoribbons top-gate FETs. *Materials Letters*, *164*, 84-88.

[2] Song, Y., Li, Y., Liu, Y., Su, X., & Ma, Q. (2015). Highly sensitive and selective detection of phosphate using novel highly photoluminescent water-soluble Mn-doped ZnTe/ZnSe quantum dots. *Talanta*, *144*, 680-685.

[3] Song, Y., Li, Y., Wang, X., Su, X., & Ma, Q. (2015). Novel aqueous synthesis methods for ZnTe/ZnSe and Mn 2+-doped ZnTe/ZnSe Type-II core/shell quantum dots. *RSC Advances*, *5*(9), 6271-6278.

[4] Su, Q., Zhang, Y., Li, S., Du, L., Zhao, H., Liu, X., & Li, X. (2015). Synthesis of p-type phosphorus doped ZnSe nanowires and their applications in nanodevices. *Materials Letters*, *139*, 487-490.

[5] Cooper, J. K., Gul, S., Lindley, S. A., Yano, J., & Zhang, J. Z. (2015). Tunable Photoluminescent Core/Shell Cu+-Doped ZnSe/ZnS Quantum Dots Codoped with Al3+, Ga3+, or In3+. *ACS applied materials & interfaces*, *7*(18), 10055-10066.

[6] Al Garni, S. E., & Qasrawi, A. F. (2016). Absorption and optical conduction in InSe/ZnSe/InSe thin film transistors. *Functional Materials Letters*, *9*(02), 1650019.

[7] Niina, T., Minato, T., & Yoneda, K. (1982). Ga-doped ZnSe grown by molecular beam epitaxy for blue light emitting diodes. *Japanese Journal of Applied Physics*, *21*(6A), L387.

[8] Xi, Y., El Bouanani, L., Xu, Z., Quevedo-Lopez, M. A., & Minary-Jolandan, M. (2015). Solution-based Ag-doped ZnSe thin films with tunable electrical and optical properties. *Journal of Materials Chemistry C*, *3*(38), 9781-9788.

[9] Yadav, K., & Jaggi, N. (2015). Effect of Ag doping on structural and optical properties of ZnSe nanophosphors. *Materials Science in Semiconductor Processing*, *30*, 376-380.

[10] Ashcroft, N. W., Mermin, N. D., & Rodriguez, S. (1998). Solid state physics.

[11] Kittel, C., McEuen, P., & McEuen, P. (1996). *Introduction to solid state physics* (Vol. 8, pp. 323-324). New York: Wiley.

[12] Dorset, D. L. (1998). X-ray diffraction: a practical approach. *Microscopy and Microanalysis*, *4*(5), 513-515.

[13] West, A. R. (2014). *Solid state chemistry and its applications*. John Wiley & Sons.

[14] Brown, G., & Brindley, G. W. (Eds.). (1980). *Crystal structures of clay minerals and their X-ray identification* (Vol. 5, pp. 305-360). London: Mineralogical Society.

[15] Koch, C., Ovid'ko, I., Seal, S., & Veprek, S. (2007). *Structural nanocrystalline materials: fundamentals and applications*. Cambridge University Press.

[16] Matějka, L., & Merhari, L. (2009). Hybrid Nanocomposites for Nanotechnology: Electronic, Optical, Magnetic and Biomedical Applications.

[17] Monshi, A., Foroughi, M. R., & Monshi, M. R. (2012). Modified Scherrer equation to estimate more accurately nano-crystallite size using XRD. *World Journal of Nano Science and Engineering*, *2*(3), 154-160.

[18] Bindu, P., & Thomas, S. (2014). Estimation of lattice strain in ZnO nanoparticles: X-ray peak profile analysis. *Journal of Theoretical and Applied Physics*, *8*(4), 123-134.

[19] Omar, A., Qasrawi, A. F., & Gasanly, N. M. (2017). Temperature effects on the structural and optical properties of the TlInSe2xS2 (1− x) mixed crystals (x= 0.3). *Journal of Alloys and Compounds*, *724*, 98-102.

[20] Anderson, P. M., Hirth, J. P., & Lothe, J. (2017). *Theory of Dislocations*. Cambridge University Press.

[21] Khusayfan, N. M., Al Garni, S. E., & Qasrawi, A. F. (2017). Design and performance of Yb/ZnS/C Schottky barriers. *Current Applied Physics*, *17*(1), 115-119.

[22] Papaconstantopoulos, D. A. (2016). *Handbook of the Band Structure of Elemental Solids: From Z*. Springer.

[23] Sze, S. M., & Ng, K. K. (2006). *Physics of semiconductor devices*. John wiley & sons.

[24] Fox, M. (2002). *Optical properties of solids*.

[25] Riedl, M. J. (2001). *Optical design fundamentals for infrared systems* (Vol. 48). SPIE press.

[26] Chen, S. H., & Kotlarchyk, M. (2007). *Interactions of photons and neutrons with matter*. World Scientific Publishing Company.

[27] Pankove, J. I. (2012). *Optical processes in semiconductors*. Courier Corporation.

[28] López, R., & Gómez, R. (2012). Band-gap energy estimation from diffuse reflectance measurements on sol–gel and commercial TiO2: a comparative study. *Journal of sol-gel science and technology*, *61*(1), 1-7.

[29] Chatterjee, U., Das, A., Ghosh, T., Duttagupta, S. P., Gandhi, M. N., & Singh, S. G. (2014). Effect of post deposition annealing on thermal evaporated ZnSe: Te towards a scintillator application. *Microelectronic Engineering*, *126*, 84-87.

[30] Khan, T. M., Mehmood, M. F., Mahmood, A., Shah, A., Raza, Q., Iqbal, A., & Aziz, U. (2011). Synthesis of thermally evaporated ZnSe thin film at room temperature. *Thin Solid Films*, *519*(18), 5971-5977.

[31] A. Solimeman, M. M. Hafiz, A. A. Abu-sehly, A. A. Alfeqeer, J. Taibah, Univ. Sci. 01 (2014) 002.

[32] Ivashchenko, M. M., Buryk, I. P., Opanasyuk, A. S., Nam, D., Cheong, H., Vaziev, J. G., & Bibyk, V. V. (2015). Influence of deposition conditions on morphological, structural, optical and electro-physical properties of ZnSe films obtained by close-spaced vacuum sublimation. *Materials Science in Semiconductor Processing*, *36*, 13-19.

[33] Agawane, G. L., Shin, S. W., Suryawanshi, M. P., Gurav, K. V., Moholkar, A. V., Lee, J. Y., ... & Kim, J. H. (2014). Novel reduced toxic route synthesis and characterization of chemical bath deposited ZnSe thin films. *Ceramics International*, *40*(1), 367-374.

[34] Yousif, A., Som, S., Kumar, V., & Swart, H. C. (2015). Comparison and analysis of Eu3+ luminescence in Y3Al5O12 and Y3Ga5O12 hosts material for red lighting phosphor. *Materials Chemistry and Physics*, *166*, 167-175.

[35] Agawane, G. L., Vanalakar, S. A., Kamble, A. S., Moholkar, A. V., & Kim, J. H. (2018). Fabrication of Cu 2 (Zn x Mg 1-x) SnS 4 thin films by pulsed laser deposition technique for solar cell applications. *Materials Science in Semiconductor Processing*, *76*, 50-54.

[36] Rao, G. K. (2014). Doping ZnS and ZnSe thin films with bismuth: A comparison between sandwiching technique and nano-particle incorporation. *Materials Science in Semiconductor Processing*, *26*, 137-143.

[37] Kafashan, H., Ebrahimi - Kahrizsangi, R., Jamali - Sheini, F., & Yousefi, R. (2016). Effect of Al doping on the structural and optical properties of electrodeposited SnS thin films. *physica status solidi (a)*, *213*(5), 1302-1308.

[38] Xu, C., Wu, Q., Hua, Y., & Li, J. (2014). The electrodeposition of Zn-Ti alloys from ZnCl2-urea deep eutectic solvent. *Journal of Solid State Electrochemistry*, *18*(8), 2149-2155.

[39] Nagaraja, K. K., Pramodini, S., Poornesh, P., & Nagaraja, H. S. (2013). Effect of annealing on the structural and nonlinear optical properties of ZnO thin films under cw regime. *Journal of Physics D: Applied Physics*, *46*(5), 055106.

[40] Fang, D., Lin, K., Xue, T., Cui, C., Chen, X., Yao, P., & Li, H. (2014). Influence of Al doping on structural and optical properties of Mg–Al co-doped ZnO thin films prepared by sol–gel method. *Journal of Alloys and Compounds*, *589*, 346-352.

[41] Thompson, C. V. (1998). Grain growth in polycrystalline thin films of semiconductors. *Interface Science*, *6*(1), 85-93.

[42] Atwood, J. L., & Seale, S. K. (1976). The interaction of aromatic hydrocarbons with organometallic compounds of the main group elements.: IV. The preparation and structure of the novel selenide K [CH3Se {Al (CH3) 3} 3]· 2C6H6. *Journal of Organometallic Chemistry*, *114*(2), 107-118.

[43] Sun, Y., Sun, Z., Gao, S., Cheng, H., Liu, Q., Piao, J., ... & Xie, Y. (2012). Fabrication of flexible and freestanding zinc chalcogenide single layers. *Nature communications*, *3*, 1057.

[44] Suresh, R., Ponnuswamy, V., & Mariappan, R. (2013). Effect of annealing temperature on the microstructural, optical and electrical properties of CeO 2 nanoparticles by chemical precipitation method. *Applied Surface Science*, *273*, 457-464.

[45] Lohar, G. M., Jadhav, S. T., Takale, M. V., Patil, R. A., Ma, Y. R., Rath, M. C., & Fulari, V. J. (2015). Photoelectrochemical cell studies of Fe 2+ doped ZnSe nanorods using the potentiostatic mode of electrodeposition. *Journal of colloid and interface science*, *458*, 136-146.

[46] Rajesh, C., Phadnis, C. V., Sonawane, K. G., & Mahamuni, S. (2014). Synthesis and optical properties of copper-doped ZnSe quantum dots. *Physica Scripta*, *90*(1), 015803.

[47] Nikesh, V. V., Lad, A. D., Kimura, S., Nozaki, S., & Mahamuni, S. (2006). Electron energy levels in ZnSe quantum dots. *Journal of applied physics*, *100*(11), 113520.

[48] Yildirim, E., Gubur, H. M., Alpdogan, S., Ari, M., Harputlu, E., & Ocakoglu, K. (2016). The effect of annealing of ZnSe nanocrystal thin films in air atmosphere. *Indian Journal of Physics*, *90*(7), 793-803.

[49] Howari, H. (2013). Influence of pulsed laser annealing on the optical properties of thermally evaporated ZnSe thin films. *Journal of Natural Sciences and Mathematics*, *5*(2).

[50] Ezema, F. I., Ekwealor, A. B. C., & Osuji, R. U. (2006). Effect of thermal annealing on the band GAP and optical properties of chemical bath deposited ZnSe thin films. *Turkish journal of physics*, *30*(3), 157-163.

[51] Sato, Y., Ashida, T., Oka, N., & Shigesato, Y. (2010). Carrier density dependence of optical band gap and work function in Sn-doped In2O3 films. *Applied Physics Express*, *3*(6), 061101.

[52] Ziabari, A. A., & Ghodsi, F. E. (2012). Growth, characterization and studying of sol–gel derived CdS nanoscrystalline thin films incorporated in polyethyleneglycol: effects of post-heat treatment. *Solar Energy Materials and Solar Cells*, *105*, 249-262.

[53] Ashraf, M., Akhtar, S. M. J., Khan, A. F., Ali, Z., & Qayyum, A. (2011). Effect of annealing on structural and optoelectronic properties of nanostructured ZnSe thin films. *Journal of Alloys and compounds*, *509*(5), 2414-2419.

[54] Wang, Y., Miska, P., Pilloud, D., Horwat, D., Mücklich, F., & Pierson, J. F. (2014). Transmittance enhancement and optical band gap widening of Cu2O thin films after air annealing. *Journal of Applied Physics*, *115*(7), 073505.

[55] Park, J. J., Kim, D. Y., Lee, J. G., Cha, Y. H., Swihart, M. T., & Yoon, S. S. (2014). Supersonic aerosol-deposited TiO 2 photoelectrodes for photoelectrochemical solar water splitting. *RSC Advances*, *4*(17), 8661-8670.

[56] M. Dongol, A. El-Denglawey, M.S. AbdElSadek, I.S. Yahia, Optik 126 (2015)1325.

[57] Akgul, F. A., Akgul, G., Yildirim, N., Unalan, H. E., & Turan, R. (2014). Influence of thermal annealing on microstructural, morphological, optical properties and surface electronic structure of copper oxide thin films. *Materials Chemistry and Physics*, *147*(3), 987-995.

[58] Abuelwafa, A. A., El-Denglawey, A., Dongol, M., El-Nahass, M. M., & Soga, T. (2015). Influence of annealing temperature on structural and optical properties of nanocrystalline Platinum octaethylporphyrin (PtOEP) thin films. *Optical Materials*, *49*, 271-278.

[59] Karthick, K., & Vijayalakshmi, K. (2014). Influence of Mg doping on the properties of ZnO films prepared on c-cut sapphire by sputtering. *Superlattices and Microstructures*, *67*, 172-180.

[60] Narayanan, N., & Kannoth, D. N. (2017). Exploring p type conductivity in ZnO thin films by In–N codoping for homo-junction devices. *Journal of Materials Science: Materials in Electronics*, *28*(8), 5962-5970.

[61] Shaaban, E. R., Yahia, I. S., & Sharaf, E. R. (2017). Structure Analysis and Optical Parameters of Nano-scale ZnSe/Flexible Substrate Thin Film. *Journal of Electronic Materials*, *46*(1), 527-534.

[62] Hassanien, A. S., Aly, K. A., & Akl, A. A. (2016). Study of optical properties of thermally evaporated ZnSe thin films annealed at different pulsed laser powers. *Journal of Alloys and Compounds*, *685*, 733-742.

[63] Al Garni, S. E., & Qasrawi, A. F. (2015). Post annealing effects on the structural, compositional, optical and dielectric properties of Cd doped GaSe thin films. *Journal of Alloys and Compounds*, *633*, 499-504.

[64] Kumar, P., Singh, J., Pandey, M. K., Jeyanthi, C. E., Siddheswaran, R., Paulraj, M., ... & Hui, K. S. (2014). Synthesis, structural, optical and Raman studies of pure and lanthanum doped ZnSe nanoparticles. *Materials Research Bulletin*, *49*, 144-150.

[65] Florence, S. S., Umadevi, M., John, R., Kumari, B. S., & Arockiasamy, D. L. (2013). Structural, morphological and optical properties of chelating ligand passivated ZnSe nanorods. *Materials Letters*, *108*, 5-8.

[66] Prakash, D., Shaaban, E. R., Shapaan, M., Mohamed, S. H., Othman, A. A., & Verma, K. D. (2016). Thickness-dependent dispersion parameters, energy gap and nonlinear refractive index of ZnSe thin films. *Materials Research Bulletin*, *80*, 120-126.

[67] Sharma, J., Shikha, D., & Tripathi, S. K. (2014). Optical and electrical properties of ZnSe thin films: Effect of vacuum annealing. *Romanian reports in Physics*, *66*(4), 1002-1011.

[68] Hadasa, K., Yellaiah, G., & Nagabhushanam, M. (2014). Effect of copper doping on structural, optical and electrical properties of Cd0· 8Zn0· 2S films prepared by chemical bath deposition. *Bulletin of Materials Science*, *37*(1), 53-60.

[69] Omareya, O. A., Qasrawi, A. F., & Al Garni, S. E. (2017). Effect of Au nanosandwiching on the structural, optical and dielectric properties of the as grown and annealed InSe thin films. *Physica B: Condensed Matter*.

[70] Bacaksiz, E., Aksu, S., Polat, I., Yılmaz, S., & Altunbaş, M. (2009). The influence of substrate temperature on the morphology, optical and electrical properties of thermal-evaporated ZnSe thin films. *Journal of Alloys and Compounds*, *487*(1), 280-285.

[71] S. Kasap, P.Capper, Springer Handbook of Electronic and Photonic Materials, Springer Science þ Business MediaInc, NewYork, NY, USA, 2006,1406.

[72] Tsay, C. Y., & Lee, W. C. (2013). Effect of dopants on the structural, optical and electrical properties of sol–gel derived ZnO semiconductor thin films. *Current Applied Physics*, *13*(1), 60-65.

[73] Phung, H. N. T., Truong, N. D., Nguyen, L. T., Thi, K. L. P., Duong, P. A., & Le, V. T. H. (2015). Enhancement of the visible light photocatalytic activity of vanadium and nitrogen co-doped TiO2 thin film. *Journal of Nonlinear Optical Physics & Materials*, *24*(04), 1550052.

[74] Venkatachalam, S., Soundararajan, D., Peranantham, P., Mangalaraj, D., Narayandass, S. K., Velumani, S., & Schabes-Retchkiman, P. (2007). Spectroscopic ellipsometry (SE) studies on vacuum-evaporated ZnSe thin films. *Materials characterization*, *58*(8), 715-720.

[75] Arslan, M., Habib, A., Zakria, M., Mehmood, A., & Husnain, G. (2017). Elemental, structural and optical properties of nanocrystalline Zn 1− x Cu x Se films deposited by close spaced sublimation technique. *Journal of Science: Advanced Materials and Devices*, *2*(1), 79-85.

[76] Shetty, M.N. (2016). *Materials science and engineering : problems with solutions*.

[77] Peter, Y. U., & Cardona, M. (2010). *Fundamentals of semiconductors: physics and materials properties*. Springer Science & Business Media.

الخصائص البنائية والضوئية لرقائق الزنك سيلينيد المطعمة والمحشوة بالألمنيوم

اعداد

أنسام السبع

إشراف

أ. د. عاطف قصراوي

الملخص

في هذه الرسالة تمت مناقشة أثار زراعة الألمنيوم بطريقة التطعيم وطريقة زراعة الشرائح على الخصائص البنائية والضوئية لمادة الزنك سالنيد، وقد تبين أن تطعيم الألمنيوم لمادة الزنك سالنيد بنسبة 13% يحول مادة الزنك سالنيد من مادة بلورية التركيب إلى مادة عشوائية التركيب. بينما تقوم الشرائح النانومترية من الألمنيوم بتحسين الخصائص البنائية بحيث تزداد كل من طول المحاور الشبكية الأفقية والعمودية ويزداد حجم الحبيبات النامية بازدياد سمك طبقة الألمنيوم ويصاحب ذلك تقلص في كمية الخلل وانخفاض في كمية الالتواء وتقل كمية الأخطاء في التراص بين الطبقات الذرية.

وتبين أيضا أن زيادة سمك الألمنيوم من 0 الى 100 نانومتر تسمح بهندسة فراغات الطاقة بداخل المادة بحيث يتقلص فراغ الطاقة من 2.67 إإلى 2.05 الكترون فولت . ولقد وجد أنه يمكن التحكم بثابت العازلية من خلال طبقات الألمنيوم النانومترية ويمكن الحصول على ثلاث اضعاف القيمة الحقيقية لثابت العازلية عند زراعة طبقة من الألمنيوم بسمك 100 نانومتر. بالاضافة إلى ذلك تبين من التحليل النظري باستخدام نظرية درود لورنتز المتطابقة مع القيمة المقاسة لثابت العازلية التخيلي بأن الألمنيوم يؤدي إلى زيادة سرعة الإلكترون لكل وحدة مجال كهربائي وزيادة كثافة الشحنات الحرة بسبب ازدياد عدد حاملات الشحنة بازدياد سمك الألمنيوم.